NORTHWESTERN UNIVERSITY

Technical Advances in Spectroscopic Single-Molecule Localization Microscopy
for Improving Spatial Resolution and Spectral Precision

A DISSERTATION

SUBMITTED TO THE GRADUATE SCHOOL
IN PARTIAL FULFILLMENT OF THE REQUIREMENTS

for the degree

DOCTOR OF PHILOSOPHY

Field of Biomedical Engineering

By

Ki-Hee Song

EVANSTON, ILLINOIS

September 2020

Abstract

Technical Advances in Spectroscopic Single-Molecule Localization Microscopy for Improving Spatial Resolution and Spectral Precision

Ki-Hee Song

Fluorescence microscopy has become a widely used tool in many research areas. However, its spatial resolution, limited to 250 nm by the diffraction limit of light, has restricted direct observation of details of ultrastructural biology. In recent years, spectroscopic single-molecule localization microscopy (sSMLM), one of super-resolution imaging techniques, has been recognized as a very powerful tool to offer molecular insights into cellular behavior. It enables the visualization of nanoscopic features of cells far beyond the diffraction limit of the conventional fluorescence microscopy by capturing spatial information of fluorescent molecules, achieving spatial resolution on the order of 40-80 nm. Furthermore, this technique has been attracting significant interest by additionally capturing the linked spectroscopic signatures. However, the sSMLM system has an intrinsic constraint imposed by the limited photon budget of individual molecules as the emitted photons need to be separated into two imaging domains to capture spatial and spectral images simultaneously. This fundamental constraint restricts the highest level of spatial resolution and spectral precision in sSMLM and thus hampers the potential for various

structural/functional imaging applications. This dissertation has provided technical advances in sSMLM to address this issue.

The work in this dissertation covers a range of topics under this overall goal: (1) theoretical studies to evaluate the performance of sSMLM using numerical simulation and analytical solution; (2) development of new optical configurations and post-data processing techniques to improve spatial and spectral precisions. Specifically, four technical advances are presented: (i) tunable spectral dispersion sSMLM, (ii) three-dimensional (3D) biplane sSMLM, (iii) symmetrically dispersed sSMLM (SDsSMLM), and (iv) photon-accumulation enhanced reconstruction (PACER); (3) their experimental validations for multimodal imaging using biology samples and nanoparticles; and (4) Manufacture of a compact optical device integrating all demonstrated 3D sSMLM functionalities. These studies offer a comprehensive technical guidance for better designing and optimizing the sSMLM system, which can facilitate more precise spectroscopic single-molecule study in broader cell biology and material science applications.

Acknowledgements

First and foremost, I would like to thank my advisor Dr. Hao F. Zhang for offering me this great opportunity at Northwestern and guiding me with endless patience throughout my studies. He is a great mentor. What he said has been a great help to me – *"Everyone has different problems.",* which looks simple but unforgettably comforted me in many moments. I appreciate his support when dealing with the challenging moments in research as well as life.

I would like to thank my committee, Dr. Sridhar Krishnaswamy and Dr. Vadim Backman, for their time, patience, and helpful advice over the years. Also, I would especially like to thank Dr. Cheng Sun for his invaluable contribution to broaden my scientific perspective over the past four years.

In addition, I would like to thank my current lab mates, Yang Zhang, Janel Davis, Lisa Beckmann, Ian Rubinoff, David Miller, Zheyuan Zhang, Benjamin Brenner, Roman Kuranov, and Zhen Cai, as well as my previous lab members, Ben Urban, Biqin Dong, Siyu Chen, Wenzhong Liu, Xiao Shu, and Brian Soetikno, for having dynamic discussions.

Lastly, I would like to thank my family, sister Jihey, mother Heesook, and father Jintae. Also, special thanks to my wife Jungyoung. Being there was a great help.

List of Abbreviations

1D	One dimensional
2D	Two dimensional
3D	Three dimensional
4D	Four dimensional
ADU	Analog to digital unit
AF647	Alexa Fluor 647
AR	Anti-reflection
ATPB	Adenosine triphosphate synthase beta subunit
βME	beta-mercaptoethanol
BN	Background shot noise
BP	Background photon
BPF	Band pass filter
BS	Beam splitter
BSA	Bovine serum albumin
C	Camera
CBC	Coordinate-based colocalization
CF660C	Cyanine-based fluorescent dye 660C
COS	African green monkey kidney cells; CV-1 in Origin, carrying SV40
CRLB	Cramer-Rao lower bound
CW	Continuous wave
D	Distance from the grating position to the intermediate image plane
DNA	Deoxyribonucleic acid
DM	Dichroic mirror
DMEM	Dulbecco's modified eagle's medium
DWP	Dual wedge prism
EDC	1-ethyl-3-(3-dimethylaminopropyl)

EM	Electron multiplication
EMCCD	Electron multiplying charge-coupled device
F	Focal length
FOV	Field-of-view
FRC	Fourier ring correlation
FWHM	Full width at half maximum
G	Grating
HILO	Highly inclined and laminated optical sheet
IIP	Intermediate image plane
IP	Image plane
L	Lens
LPF	Long pass filter
M	Mirror
MES	2-(N-morpholino) ethanesulfonic acid
MINFLUX	Minimal photon fluxes
MLE	Maximum likelihood estimation
MSD	Mean squared displacement
NA	Numerical aperture
NB	The number of blinking events
NaCl	Sodium chloride
NHS	N-Hydroxysuccinimide
OBL	Objective lens
PACER	Photon-accumulation enhanced reconstruction
PALM	Photo-activated localization microscopy
PAINT	Point accumulation for imaging in nanoscale topography
PBS	Phosphate-buffered saline
PLL	Poly-l-lysine
PSF	Point spread function

S	Slit
SC	Spectral centroid
sCMOS	Scientific complementary metal–oxide–semiconductor
SD	Spectral dispersion
SDsSMLM	Symmetrically dispersed spectroscopic single-molecule localization microscopy
SH	Spectral heterogeneity
SM	3D sSMLM module
SMLM	Single-molecule localization microscopy
SPT	Single particle tracking
SR-STORM	Spectrally resolved stochastic optical reconstruction microscopy
SSD	Spectral shift distance
sSMLM	Spectroscopic single-molecule localization microscopy
STED	Stimulated emission depletion
STORM	Stochastic optical reconstruction microscopy
SN	Signal shot noise
TL	Tube lens
TIRF	Total internal reflection fluorescence
TOM20	Mitochondrial Outer Membrane translocase complex
QD	Quantum dot
QE	Quantum efficiency
RMS	Root-mean-square
RN	Readout noise
RP	Right angle prism
SNR	Signal to noise ratio
WP	Wedge prism

Table of Contents

List of Figures

List of Tables

Chapter 1

Introduction

1.1 BACKGROUND AND MOTIVATION

1.1.1 Fluorescence microscopy and the optical diffraction limit

We have observed remarkable growth in the use of optical microscopy as a key tool to offer insights into cellular behavior. Its inherently non-invasive nature allows for direct observation of structures and dynamics in living cells. In particular, fluorescence microscopy, among a variety of optical imaging techniques, has been established as a fundamental tool for cell biology due to its molecular specificity and high sensitivity. Also, as many fluorescent probes are available with a range of excitation and emission spectra, it enables simultaneous visualization of multiple targets by multicolor imaging.

Despite being widely useful, the spatial resolution of the conventional fluorescence microscopy, in far-field optics, has restricted a direct observation of details of ultrastructural biology [1, 2]. Due to the diffraction of light, the fluorescence emitted from a point source appears as a blurred spot with finite size in an image plane when passing through a lens-based imaging system. This blurred image is the Airy pattern, which contains a bright central region, Airy disk, together with a series of rings around, and also referred to as a point spread function (PSF) of the imaging system. Ernst Abbe found in 1873 that the imaging system (or light) has a minimum resolvable distance, which refers to the resolution limit, to distinguish two closest Airy patterns (or two-point sources). This resolution limit is defined by the following formula:

$$\Delta x, y \approx \frac{\lambda}{2NA} \tag{1.1}$$

$$\Delta z \approx \frac{2\lambda}{NA^2} \tag{1.2}$$

where λ is the wavelength of emitted light; NA is the numerical aperture of the objective lens, $NA = n\sin\theta$; n is the refractive index of the medium; and θ is the maximal half-collection angle of the objective lens. The resolution limit is later sophisticated by Lord Rayleigh in 1896 and defined as the distance where the central maximum of the Airy disk from one of the point sources meets with the first minimum dark ring of the Airy disk from the other point sources. This is an arbitrary standard but commonly accepted for most imaging applications. It is expressed by the following formula:

$$\Delta x, y \approx \frac{0.61\lambda}{NA} \tag{1.3}$$

Accordingly, the resolution limit of far-field fluorescence microscopy is 200-300 nm in the lateral dimensions and 500-600 in the axial dimension for visible light and thus, unfortunately, leaves many biology questions inside cells, which occurs at scales far below the diffraction limit, to be unknown.

1.1.2 Spectroscopic single-molecule localization microscopy

Spectroscopic single-molecule localization microscopy (sSMLM), one of a family of super-resolution imaging techniques awarded the Nobel Prize in Chemistry 2014, has been recognized as a very powerful tool to offer molecular insights into cellular behavior with nanoscale precision. It enables the visualization of nanoscopic features of cells far beyond that of the conventional fluorescence microscopy by capturing spatial information of fluorescent molecules, achieving

spatial resolution on the order of 40-80 nm [3-6]. The increased spatial resolution provides rich information on individual molecules to extend our fundamental understanding of cell biology.

Furthermore, this technique has been attracting significant interest by additionally capturing the linked spectroscopic signatures, together with the nanoscopic location, of individual molecules. Its advantage to acquire the full emission spectrum of each molecule enables specific identification of different types of single molecules and further unprecedented extension of the number of available fluorophores in multi-color super-resolution imaging [3, 7]. In addition, it allows studies that reveal comprehensive physiological and chemical information, including local pH, and chemical polarity, by resolving minute spectroscopic variations associated with the interaction of single molecules to their local environment [8-14]. Besides, sSMLM can effectively suppress background, such as autofluorescence of impurities or Raman scattering from water, by separating them from target molecules based on their different emission spectra [15]. Thus, its great potential has led to many studies for a better understanding of a broad range of biomedical research.
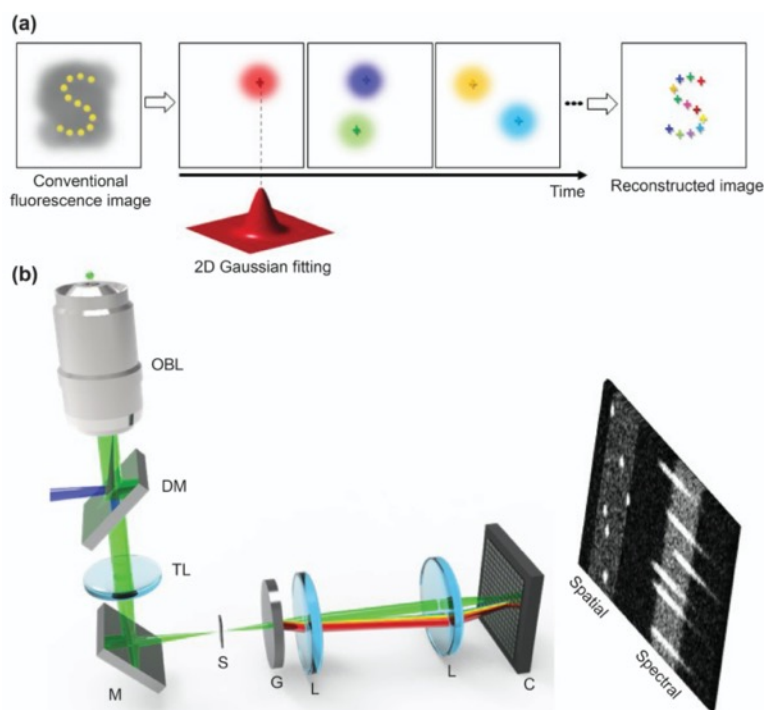
Figure 1.1 (a) Working principle and (b) schematic of sSMLM. The conventional fluorescence microscopy is modularized with a grating-based spectrometer. It allows us to simultaneously capture spatial and spectral information of individual molecules in a single camera. OBL: objective lens; DM: dichroic mirror; TL: tube lens; M: mirror; S: Slit; G: Grating; L: lens; C: Camera.

Figures 1.1(a) and 1.1(b) show a working principle of sSMLM for image reconstruction and its schematic, respectively. If a fluorescence-labeled structure (the yellow circles in Fig. 1.1(a)) is imaged by the conventional fluorescence microscopy, the image appears blurred by the diffraction limit of light (the gray blur in Fig. 1.1(a)). However, in sSMLM, each fluorophore on the structure of interest stochastically emits fluorescence, referred to as "blinking", and these isolated emission events are captured with the shape of the diffraction-limited PSF in spatial images at different frames. The coordinates of each imaged fluorophore are estimated, typically by 2D Gaussian fitting [16], and the super-resolved image (the plus markers in Fig. 1.1(a)) is reconstructed with their distinctive emission spectra.

To implement sSMLM, the conventional fluorescence microscopy is modularized with a grating-based spectrometer, as illustrated in Fig. 1.1(b) [7]. Basically, the sSMLM system can be implemented by inserting a dispersive element, such as a grating [5] or a prism [3], before image detection. Thus, in the emission beam path, the light is separated into two beams: (1) a non-dispersed spatial beam and (2) a spectrally dispersed spectral beam, which allows for simultaneous acquisition of the spatial and spectral images of single molecules.

1.1.3 Challenges for sSMLM

Despite its revolutionary capabilities, the sSMLM system has several constraints fundamentally imposed by the limited photon budget of each emission event and the system complexity, as the total emitted photons need to be separated into two imaging domains to simultaneously record the spatial and spectral images. These fundamental constraints restrict the highest level of spatial resolution and spectral precision in sSMLM despite the excellent brightness of the fluorophore dyes used in sSMLM, such as Alexa Fluor 647 (AF647) that emits ~ 5000 photons [17].
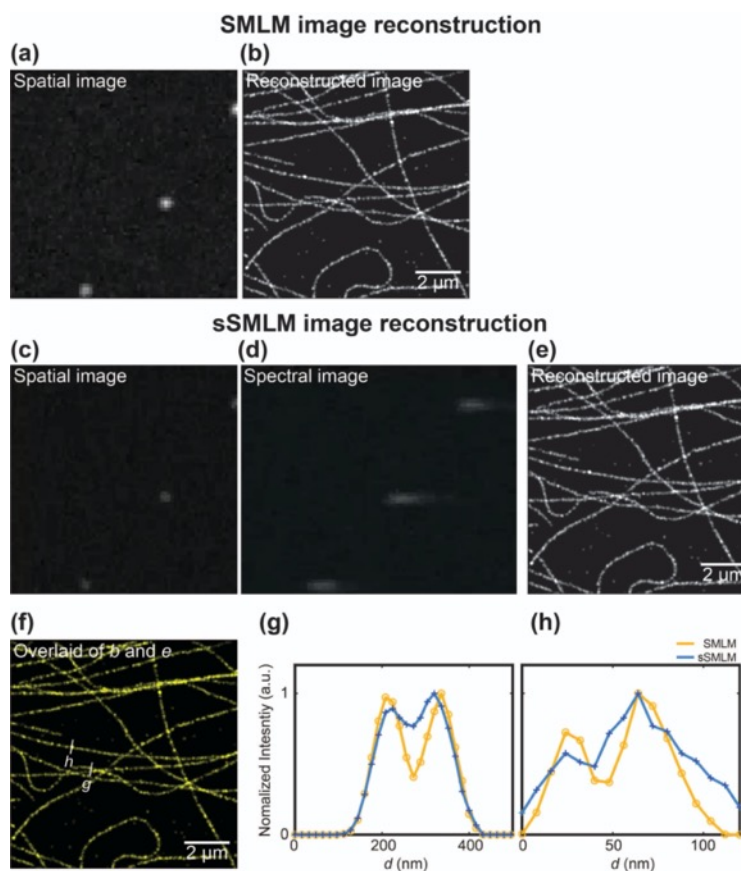
Figure 1.2 Comparison of spatial resolution between SMLM and sSMLM images (a) First frame of spatial image in SMLM (b) Reconstructed SMLM image. The first frames of (c) spatial and (d) spectral images in sSMLM (e) Reconstructed sSMLM image. (f) Overlaid image of panels b and e. (g) and (h) The cross-sections highlighted by the white lines in the panel f. The sSMLM spatial and spectral images are simulated based on the experimentally acquired SMLM image in the panel a with a 1:3 splitting ratio, a spectral dispersion of 5 nm/pixel, and the emission spectrum of AF647.

Figure 1.2 shows a comparison of spatial resolution between the conventional SMLM image and the sSMLM image. In SMLM, from several frames that contain many PSFs over the field-of-view (FOV) (Fig. 1.2(a)), a super-resolution image is reconstructed (Fig. 1.2(b)). Here, the photon budget of the PSFs is intrinsically determined by the stochastically emitting fluorescence ("blinking") of each molecule, which governs localization precision and predominantly determines

the imaging resolution, typically 10-30 nm [2]. Here, the localization precision can be described by the following formula [18]:

$$\sigma = \sqrt{\frac{s^2 + a^2/12}{N}\left(1 + 4\tau + \sqrt{\frac{2\tau}{1+4\tau}}\right)} \qquad (1.4)$$

where $\tau = 2\pi b(s^2 + a^2/12)/Na^2$; s is the standard deviation of the Gaussian function (nm); a is the back-projected pixel size (nm); N is the number of detected photons; b is the number of background photons per pixel. On the other hand, in sSMLM, as a portion of photons are separated to produce the spectral image, it unfavorably reduces the number of photons for the spatial image and, consequently, reduces the localization precision and the imaging resolution. As a result, we detect dimmer PSFs in the spatial image (Fig. 1.2.(c)) for sSMLM compared with SMLM (Fig. 1.2(a)), together with their dimmer emission spectra (Fig. 1.2.(d)). Although the reconstructed sSMLM image (Fig. 1.2.(e)) are nicely overlaid with the reconstructed SMLM image (Fig. 1.2.(b)) over the entire FOV (Fig. 1.2.(f)), sSMLM failed to resolve the fine features of two tubulin structures as shown in cross-sections (Figs. 1.2(g) and 1.2(h)). In contrast, SMLM successfully resolved both tubulins, with clear separations (of around 100 nm and 35 nm in Figs. 1.2(g) and 1.2(h), respectively), satisfying the Rayleigh resolution criterion.

Moreover, in sSMLM, the required photon budget for each channel can be different depending upon both applications and the experimental condition. Thus, a ratio of the photon budget between two channels would ideally be able to be tuned. However, there is still no sSMLM that gives the flexibility to control a ratio of photons between two channels or maximize the utilization of a given photons in each channel. Furthermore, 3D imaging with sSMLM is not straightforward due to the

limited photon budget. It also hampers the potential for various structural/functional super-resolution imaging applications in 3D.

1.2   SCOPE OF THE DISSERTATION

The objective of this dissertation is, ultimately, to provide technical advances in sSMLM to improve spatial and spectral precisions. Under this general goal, the work in this dissertation covers a range of topics: (1) theoretical studies using numerical simulation and analytical solution; (2) development of new optical configurations and post-data processing techniques to improve spatial and spectral precisions. (3) their experimental validations for multimodal imaging using biology samples and nanoparticles; and (4) Manufacture of a compact optical device integrating all demonstrated 3D sSMLM functionalities.

1.3   DISSERTATION OUTLINE

Chapter 2 presents a theoretical foundation to determine the fundamental limit of the sSMLM system. Specifically, Chapter 2 introduces a theoretical model with numerical simulation and analytical solution to understand the newly introduced spectral precision. This spectral precision is investigated with considering the contribution of key parameters: 1) noise factors, such as shot noise of emission spectra, background, and readout noise, 2) spectral dispersion (SD), and 3) spectral calibration error. This study reveals the delicate balance among key imaging parameters for achieving the optimal spectral precision.

Chapter 3 presents the development of a tunable SD sSMLM system based on a grating-based spectrometer and investigates the influence of SD on image quality in multi-color imaging, as an experimental extension of the previous chapter. The carefully tuning of SD enables simultaneous

three-color super-resolution imaging in fixed cells using multiple far-red emitting dyes with minimized crosstalk. This study suggests that an optimal SD needs to be identified to minimize the crosstalk, and thus mischaracterization in multi-color sSMLM imaging.

Chapter 4 introduces a new 3D imaging technique in sSMLM, 3D biplane sSMLM. Implementing the biplane method based on the already-existing spatial and spectral imaging channels in sSMLM allows for more efficient use of the limited photon budget. Its multi-color 3D imaging capability is demonstrated by visualizing the colocalization of different organelles in fixed cells using multiple far-red emitting dyes.

Chapter 5 presents the development of symmetrically dispersed sSMLM (SDsSMLM), which fully utilizes all photons of individual molecules in both spatial and spectral channels. Improvements in spatial and spectral precisions are investigated and quantified under different experimental conditions, compared with existing sSMLM. And, its functionalities are demonstrated in multi-color imaging using fixed cells and 3D single-particle tracking using quantum dots (QD).

Chapter 6 presents the development of a post-data processing technique for sSMLM, photon-accumulation enhanced reconstruction (PACER), to break the physical photon limit by accumulating photons over repeated stochastic emission events from the same dye species through spectral identification. Improvement in spatial precision up to sub-2-nm is demonstrated using QDs. And, it is further validated using two types of DNA origami nanostructures with known feature size as small as 6 nm.

Chapter 7 proposes a compact 3D sSMLM module design using a dual-wedge prism-based lensless spectrometer. Through numerical simulations, theoretically achievable spatial and spectral precisions are estimated. And, its 3D spectroscopic single-molecule imaging capability is demonstrated using a realistic simulated data set.

Chapter 8 summarizes this dissertation and presents future works.

Chapter 2

Theoretical foundation to evaluate the performance of sSMLM based on numerical simulation and analytical solution

sSMLM captures and analyzes the full emission spectrum of every stochastic single-molecule emission while maintaining nanoscale precision in spatial localization. This spectroscopic imaging capability of sSMLM necessitates the establishment of a theoretical foundation of the newly introduced spectral precision to guide the system design and optimization. Here, we introduce a theoretical model with numerical simulation and analytical solution to evaluate the performance of sSMLM. For this, we analyze spectral precision with considering spectral calibration procedure and the contribution of key parameters, including photon numbers per single emission spectra, background, image noises, and system's spectral dispersion (SD). Our theoretical model enables quantitative evaluation of all experimental conditions. This study suggests that the best spectral precision can only be achieved at a particular system SD. More importantly, it reveals the delicate balance among key imaging parameters for achieving the optimal spectral precision, which provides a comprehensive guide for optimizing sSMLM. This chapter is adapted from a previously published article in *Review of Scientific Instruments* [19].

2.1 INTRODUCTION

Spectroscopic single-molecule localization microscopy (sSMLM) enables specific identification of different types of individual molecules and, therefore, the number of different molecules that can be imaged simultaneously is no longer constrained by the discrete color

channels in existing multi-color super-resolution microscopy methods [3]. In addition, resolving minute spectroscopic variations in fluorescence emission associated with molecular compositional and conformational heterogeneities at the single-molecule level enables studying inter-molecular and intra-molecular interactions [12]. Furthermore, its potential can be extended for chemical recognition by probing chemical reactions at the single-molecule level [20-22]. Ultimately, sSMLM may allow a better understanding of the properties of single molecules rather than average properties of a large molecule population in current spectroscopy, which will benefit cell and molecular biology studies. Motivated by its great promise, sSMLM has been implemented by multiple groups with diverse optical designs and imaging parameters, which signifies the need for a unified theoretical framework to correlate key system parameters and their contributions to the performance of sSMLM, especially the newly introduced spectral precision.

sSMLM simultaneously records the diffraction-limited spatial images of stochastically emitting fluorescent molecules and the spectrally dispersed spectral images resulting from the convolution of diffraction-limited PSF and the linearly-spread spectral signature distinct to individual molecules. While researchers have developed theoretical models for localizing molecules from the spatial images with the highest spatial precision [18, 23-25], spectral precision in extracting molecules' spectroscopic signatures from the spectral image is yet to be fully understood. Since sSMLM's goal is to obtain the optimal precisions from both the diffraction-limited spatial and spectral images, we introduced a theoretical model with numerical simulation and analytical solution to analyze spectral precision with contributions from all key system parameters. We further quantitatively evaluated the contributions from image noises and the

spectral calibration procedure with respect to the system's SD to provide a guideline in optimizing the sSMLM system.

2.2 METHODS

2.2.1 Working principle of sSMLM

Building upon SMLM, sSMLM can be realized by inserting a dispersive optical element, such as a prism or a diffraction grating. Using the dispersive element, we can divide the emitted photons from every stochastic single-molecule emission event into two groups, which respectively form one spatial image and one spectral image. Thus, every recorded sSMLM image frame consists of simultaneously acquired spatial and spectral images of all the stochastic emission events happened during the exposure time of the image frame. We used the spatial image to localize the positions of individual emission events and further to establish the reference point for analyzing the spectroscopic signatures in the spectral image.
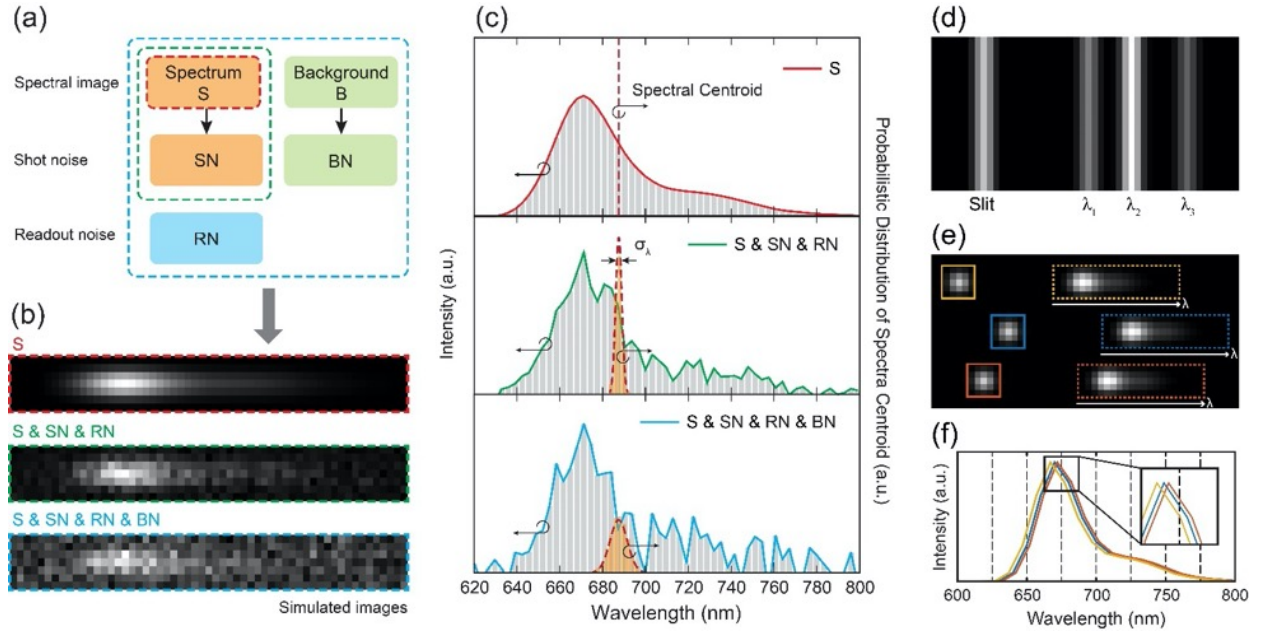
Figure 2.1 (a) Summary of the different image noises. (b) Simulated spectral images illustrate the contributions of different image noises. The ideal spectral image (**S**) shown in the red box. Image noises, including **SN** and **RN**, were added to the ideal spectral image (in the green box). When background (**B**) is presented (20000 photons in total), **BN** further increases the fluctuation of the spectral image (in the blue box). (c) Spectra (left vertical axis) of the three simulated spectral images shown in (b) and their spectral precisions. To emphasize the influence of different image noises, we first subtracted the background and visualized the spectral image in (b) and the spectra in (c). (d) Simulated reference image for spectral calibration. (e) An ideal sSMLM image, which contains three emission events, recorded in a single camera frame. Every recorded sSMLM image frame consists of simultaneously acquired spatial and spectral images. (f) The pixelated emission spectra from (e). Inset shows the magnified view of the black box in (f) to illustrate the spectral-shift error. a.u.: arbitrary units.

2.2.2 Spectral precision

As illustrated in Fig. 2.1(a), the recorded spectral images comprise an emission spectrum and the background, which are governed by the intrinsic characteristics of the samples. Image noises, including shot noise from both the emission spectrum and background, and the readout noise collectively contribute to the fluctuations in the spectral images [Figs. 2.1(a) and 2.1(b)]. Among several estimators that have been tested in SMLM, including least-square fitting and maximum-likelihood fitting [16], we use the commonly-accepted weighted centroid method, to represent the

emission spectrum [5]. The spectral centroid wavelength can be obtained via the weighted centroid method (as the weighted mean) defined by

$$\lambda_c = \frac{\sum_i \lambda_i S_i}{\sum_i S_i} \tag{2.1}$$

where λ_i is the wavelength determined by the calibration process at pixel i and S_i is the signal intensity at each pixel i after the background subtraction. Spectral precision is described by the standard deviation of the centroid wavelength distribution, which is typically a Gaussian distribution since it reflects the distribution of statistical errors in experimental measurements.

2.2.3   Image noise model

To investigate the influence of various noise sources on the spectral precision, we established the camera noise model using the electron multiplying charge-coupled device (EMCCD) camera (iXon897, Andor). Given the electron multiplication (EM) gain process, the noise model can be expressed as [26],

$$Y_{i,j} = \left(S_{i,j} + B_{px,i,j} \right) + F_{EM} \left(SN_{i,j} + BN_{i,j} \right) + RN_{i,j} \tag{2.2}$$

where $S_{i,j}$ is the emission signal of single-molecule fluorescence emitters at the pixel (i,j); $Y_{i,j}$ is the EMCCD output signal of $S_{i,j}$; $B_{px,i,j}$ is the background per pixel; $F_{EM}(=\sqrt{2})$ is the excess noise factor generated by the EM process [16]; $SN_{i,j}$ is the shot noise; $BN_{i,j}$ is the background noise; and $RN_{i,j}$ is the readout noise. Note that $(S_{i,j} + SN_{i,j})$ and $(B_{px,i,j} + BN_{i,j})$ follow Poisson distributions with mean values of $S_{i,j}$ and $B_{px,i,j}$, respectively, and $RN_{i,j}$ follows Gaussian distribution with a zero mean and a standard deviation equaling to the rms readout noise. The dark noise is negligible for deeply-cooled EMCCD camera with a fast acquisition time ($\sim$10 ms) [26].

2.2.4 Numerical simulation

We implemented numerical simulation by generating the noise-added spectral images of a single-molecule fluorescent emitter. To simulate its emission spectrum, a spatial image was first produced. The PSF was modeled as a two-dimensional (2D) Gaussian function and the full-width-at-half-maximum (FWHM) of PSF was set to be 2.57 pixels, which represents the PSF acquired by an EMCCD with a pixel size of 16 µm using a 100x Nikon TIRF objective lens (NA=1.49) and a 1.5x tube lens (f = 300 mm) at the emission wavelength of 670 nm. Using the generated PSF, an ideal spectral image was calculated at a certain SD as a result of the convolution of the PSF and the emission spectra of a single fluorescent molecule (Alexa Fluor 647). The SD of the simulated spectral images was defined as the wavelength range per individual pixel. Assuming the SD is linear in a given sSMLM system, it can be expressed $\Delta\lambda = W_{\mathrm{p}} \times R_{\mathrm{d}}$ (nm/pixel), where W_{p} is the width of the camera pixel (µm); R_{d} is the reciprocal linear dispersion and shows the separation of wavelength (nm) per an interval distance (µm). The representative images of the simulated spectral image of a single fluorescence molecule at the SD of 3.2 nm/pixel with and without image noises are illustrated in Fig. 2.1(b). All key characteristic parameters of the EMCCD camera used in simulations are listed in Table 2.1.

Table 2.1 List of camera parameters used in simulations.

Camera	Pixel size	QE[a] @ 670 nm	EM gain[b]	RN[c]	F_{EM}[d]	ADU Gain[e]
iXon 897	16 µm	92.5 %	100	2 e-	$\sqrt{2}$	14.2 e-/count

[a]QE is the quantum efficiency; [b]EM gain is the electron multiplication gain; [c]RN is the readout noise; [d]F_{EM} is the excess noise factor; [e]ADU Gain is the analog-to-digital unit.

Considering that the total amount of background presented in the entire spectral image is a constant, the number of photons from the background allocated to each camera pixel is inversely proportional to the SD. Therefore, the photon number of the background recorded by each pixel can be defined as

$$B_{px} = \frac{B}{N_\lambda N_y} = \frac{B}{(W_\lambda / \Delta\lambda)N_y} \tag{2.3}$$

where B_{px} is the background per pixel; B is the total background; N_y and N_λ are the number of pixels along y-axis and spectral-axis, respectively; W_λ is the wavelength range used in spectral analysis; and $\Delta\lambda$ is the SD (nm/pixel). For instance, when y-axis contains 7 pixels and the wavelength range is 160 nm, the total background of 5600 photons assigns 20 photons per pixel at the SD of 4 nm/pixel.

Finally, we generated 10000 noise-added spectral images at different B according to the noise model defined in Eq. (2.3). We then obtained the emission spectra by binning the 7 pixels along the y-axis. In this study, we used a wavelength range of 160 nm (620 nm – 780 nm) for spectral analysis using the weighted centroid method.

2.2.5 Spectral calibration procedure

In order to convert the recorded spectral images in the spatial domain to the emission spectrum in the wavelength domain, a spectral calibration procedure is required to establish the spatial-wavelength mapping, which is specific to individual sSMLM systems. Unique to sSMLM, the spectral calibration procedure refers to not only the acquisition of the reference image for the conventional spectral calibration (Step 1), but also the conversion of the recorded spectral images into emission spectrum in the wavelength domain (Step 2).

In Step 1, we first recorded a reference image using a narrow slit illuminated by a spectrometer wavelength calibration light source, as illustrated by Fig. 2.1(d). A single line corresponds to the slit position in the spatial image whereas the multiple spectral lines in the spectral image correspond to the emissions centered at $\lambda_1, \lambda_2,$ and λ_3 of the calibration source. Then, the pixel positions and wavelengths of these spectra lines were fitted by a linear polynomial function using a customized MATLAB code. We used the fitted function to determine the conventional spectral calibration between the spatial image and spectral image.

In Step 2, we converted the recorded spectral images of individual stochastic radiation events from pixel position to wavelength, as illustrated in Figs. 2.1(e) and 2.1(f). Here, spatial images of the radiation events were used as the reference location for the spectral analysis. Accordingly, spectral windows with the same wavelength range can be determined by the spectral calibration obtained in Step 1, shown as the colored boxes in Fig. 2.1(e). Therefore, by integrating the spectral images along the y-axis, we can obtain the emission spectra as depicted in Fig. 2.1(f).

2.2.6 Spectral-shift error

Unique to sSMLM, the spectral calibration procedure (Step.2) introduces a systematic error in converting the recorded spectral images in the spatial domain into the emission spectrum in the wavelength domain. This leads to a sub-pixel level spectral shift in calculating the spectral centroid, which is defined as the spectral-shift error. The spectral-shift error becomes more significant for the system featuring lower SD. As an example, an ideal sSMLM image of three emission events at system SD of 10 nm/pixel is illustrated in Fig. 2.1(e). After the spectral analysis, the pixelated emission spectra of all events are plotted in Fig. 2.1(f). The inset shows the magnified view of the black-boxed region, illustrating the spectral-shift error. Notably, the spectral analysis

contains two types of uncertainties: the localization uncertainty and the spectral-shift error, which are induced by the localization analysis and the spectral calibration procedure, respectively. Since the localization precision is typically at deep-sub-pixel level, we assume that its influence on the spectra-shift error is negligible.

2.2.7 Analytical solution

To better understand the underlying principle, we further established the analytical solution of the spectral precision. To simplify the analytical model, here we assume the spectral image consists of the emission spectrum described as a 2D Gaussian function [16, 24, 27],

$$S(\lambda, y) = N \frac{1}{\sqrt{2\pi s_\lambda^2}} e^{-\frac{(\lambda-\lambda_c)^2}{2s_\lambda^2}} \frac{1}{\sqrt{2\pi s_y^2}} e^{-\frac{(y-y_c)^2}{2s_y^2}} \tag{2.4}$$

where N is the total number of photons of the emission signal acquired in the spectral image, s_y and s_λ are standard deviations of the Gaussian function along the y- and spectral- axes, and y_c and λ_c are weighted centroids of the Gaussian function along the y- and spectral- axes.

Since the spectral images are recorded using pixelated sensor array, the spectral centroid can be expressed in the discretized form as

$$\lambda_c = \frac{\sum_{i,j}\left[(S_{i,j} + R_{i,j})\lambda_{i,j}\right]}{\sum_{i,j}(S_{i,j} + R_{i,j})} \tag{2.5}$$

where i, j are the pixel coordinates in the spectral image and R is a noise contribution due to various sources, including shot noise ($n_{s,i,j}$) of the emission spectrum, the shot noise of the background (n_{bg}), and the readout noise (n_{ro}). In the analytical solution, we assume that $n_{s,i,j}$ and n_{bg} follow Poisson distributions with the mean values of $S_{i,j}$ and B_{px}, respectively, whereas n_{ro} follows

Gaussian distribution with a zero mean. Given the main noise sources, $r_{i,j}$ (the standard deviation of $R_{i,j}$) can be written as $r_{i,j}^2 = n_{s,i,j}^2 + n_{bg}^2 + n_{ro}^2$. Therefore, the spectral precision, σ_λ, can be described using propagation of error assuming the errors are uncorrelated [24, 28, 29]:

$$\sigma_\lambda^2 = \frac{\sum_{i,j}\left(\lambda_{i,j} - \lambda_c\right)^2 n_{s,i,j}^2}{N^2} + \frac{n_{bg}^2 \sum_{i,j}\left(\lambda_{i,j} - \lambda_c\right)^2}{N^2} + \frac{n_{ro}^2 \sum_{i,j}\left(\lambda_{i,j} - \lambda_c\right)^2}{N^2} \qquad (2.6)$$

In Eq. (2.6), the first term represents the contribution of shot noise from the emission spectrum (σ_s). In a similar way to calculate its contribution in localization precision [24, 30], σ_s along the spectral-axis can be written as $\sigma_s^2 = s_\lambda^2/N$. Noting that we ignored the pixelation noise to simplify the analytical solution as its influence is less than 5 % under our experimental condition (when SD < 10 nm/pixel) [30].

The second term in Eq. (2.6) represents the contribution of the shot noise from the background σ_{bg} and here we have

$$\sigma_{bg}^2 = \frac{n_{bg}^2}{N^2}\sum_{i,j}\left(\lambda_{i,j} - \lambda_c\right)^2 = \frac{n_{bg}^2}{\Delta\lambda\Delta y N^2}\iint_{-\infty}^{+\infty}\left(\lambda_{i,j} - \lambda_c\right)^2 d\lambda dy \qquad (2.7)$$

where $\Delta\lambda$ is the SD (nm/pixel) and Δy is the image pixel size along the y-axis (nm). The size of the kernel used in our analytical model was set to be $[-4s_y, 4s_y]$ along the y-axis and $[-4s_\lambda, 4s_\lambda]$ along the spectral-axis, respectively, around the weighted centroid (λ_c, y_c) in order to cover the area corresponding to 99.9% of the signal in the spectral image. Thus

$$\sigma_{bg}^2 = \frac{n_{bg}^2}{\Delta\lambda N^2}\int_{-4s_\lambda}^{+4s_\lambda}(\lambda_i - \lambda_c)^2 d\lambda \frac{1}{\Delta y}\int_{-4s_y}^{+4s_y} dy = \frac{1024 n_{bg}^2 s_\lambda^3 s_y}{3\Delta\lambda\Delta\lambda N^2} \qquad (2.8)$$

where $n_{bg}^2 = B_{px} = \frac{B}{(8s_\lambda/\Delta\lambda)(8s_y/\Delta y)} = \frac{B\Delta\lambda\Delta y}{64s_\lambda s_y}$ since the background noise is determined by the background per pixel. Therefore, we have

$$\sigma_{bg}^2 = \left(\frac{B\Delta\lambda\Delta y}{64s_\lambda s_y}\right)\frac{1024s_\lambda^3 s_y}{3\Delta\lambda\Delta y N^2} = \frac{16Bs_\lambda^2}{3N^2} \tag{2.9}$$

The third term in Eq. (2.6) represents the contribution of readout noise (σ_{ro}). Since readout noise is constant for each pixel, we have

$$\sigma_{ro}^2 = \frac{n_{ro}^2}{N^2}\sum_{i,j}\left(\lambda_{i,j} - \lambda_c\right)^2 = \frac{n_{ro}^2}{\Delta\lambda\Delta y N^2}\int\int_{-\infty}^{+\infty}\left(\lambda_{i,j} - \lambda_c\right)^2 d\lambda dy = \frac{1024n_{ro}^2 s_\lambda^3 s_y}{3\Delta\lambda\Delta y N^2} \tag{2.10}$$

Additionally, the uncertainty of the spectral-shift error, σ_{sse}, is linearly proportional to $\Delta\lambda$. As the spectral-shift error follows a top-hat distribution, σ_{sse} can be quantitatively expressed as [30]

$$\sigma_{sse}^2 = \frac{\Delta\lambda^2}{12} \tag{2.11}$$

In conclusion, by adding a factor of EM process to the shot noise in case of the EMCCD camera [24], the overall spectral precision is expressed as

$$\sigma_\lambda^2 = F_{EM}^2\left(\sigma_s^2 + \sigma_{bg}^2\right) + \sigma_{ro}^2 + \sigma_{sse}^2 = F_{EM}^2\left(\frac{s_\lambda^2}{N} + \frac{16Bs_\lambda^2}{3N^2}\right) + \frac{1024n_{ro}^2 s_\lambda^3 s_y}{3\Delta\lambda\Delta y N^2} + \frac{\Delta\lambda^2}{12} \tag{2.12}$$

where F_{EM} is approximately $\sqrt{2}$ due to the EM gain when the EMCCD camera is used for image acquisition [16].

Table 2.2 List of parameters used in analytical solution.

N (photons)	B (photons)	Δy (nm)[a]	n_{ro} (e-)	s_y (nm)	s_λ (nm)

3000	5000	106.67	2	116.47	20

$^a\Delta y$ is the image pixel size along the y-axis on the objective plane, which is determined by EMCCD camera pixel size (16 μm, shown in Table 2.1) divided by the magnification of the imaging system, which includes 100x from the objective lens and 1.5x from the matching tube lens being used.

2.3 RESULTS

If only considering the contributions from the three aforementioned primary forms of image noises, the overall characteristic scaling behavior of spectral precision with respect to SD was calculated as the green curve in Fig. 2.2(a). In contrast, the spectral-shift error is linearly proportional to the pixel size and, thus, can be significant in a system with a lower SD (the red curve in Fig. 2.2(a)). Considering the competing contributions from image noises and spectral-shift error, our numerical models predicted the optimal SD in order to achieve the best spectral precision (the black curve in Fig. 2.2(a)). For example, the best spectral precision of 1.31 nm can be achieved by designing the optical system with an SD of 1.6 nm/pixel for a blinking event with 3000 photons.
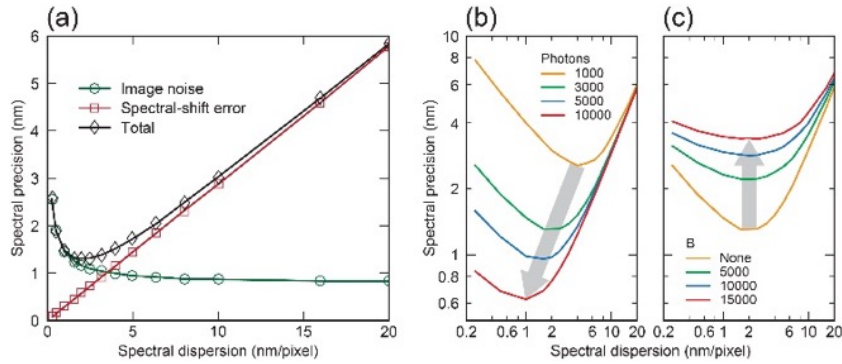
Figure 2.2 (a) Spectral precision as a function of SD when considering image noises (the green circle), spectral-shift error (the red square), and their overall contributions (the black diamond). (b) Dependence of spectral precision on SD under different photon numbers without background. (c) Dependence of spectral precision on SD with different background levels when the spectral signal contains 3000 photons. Note that the iteration number of numerical simulations is 10000.

Our model further enables quantitative evaluation of all experimental conditions. Using photon number as an example, while one would anticipate that increasing photon number will favorably improve the spectral precision, our study suggests that the best spectral precision can only be achieved with a matching SD at a given photon number as shown in Fig. 2.2(b). Taking 20-nm/pixel SD as an example of a non-optimal condition, increasing photon number from 1000 to 10000 will marginally improve the spectral precision from 6.02 nm to 5.79 nm. In contrast, respectively matching optimal SD of 4 and 1 nm/pixel with 1000 and 10000 photons, the spectral precision improves from 2.56 nm to 0.62 nm. We showed that while higher background noise reduces the overall spectral precision, background noise negligibly impacts the optimal SD required to achieve the best spectral precision (Fig. 2.2(c)).
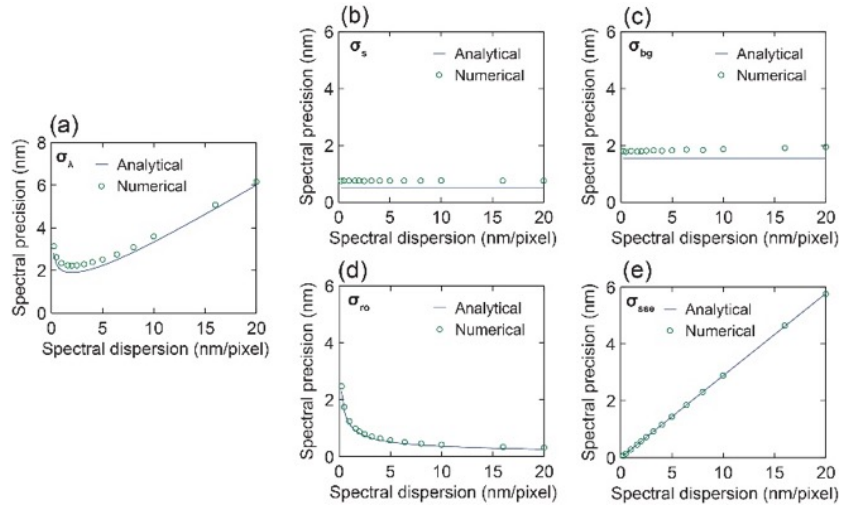
Figure 2.3 Comparison of spectral precisions obtained by numerical simulation and analytical solution. The spectral signal contains 3000 photons and the total background has 5000 photons. (a) Overall spectral precision and spectral precision when only considering the contribution of (b) the shot noise from the emission spectrum, (c) the shot noise from the background, (d) the readout noise, and (e) the spectral-shift error with respect to SD.

As illustrated in Fig. 2.3(a), we confirmed an excellent agreement between the numerical simulation and analytical solution of the overall spectral precision with respect to SD when

considering the contribution from all system parameters, as listed in Table 2.2. We also confirmed that σ_s and σ_{bg} are constant and independent of the SD whereas σ_{ro} is inversely proportional to the square root of the SD as illustrated in Figs. 2.3(b)-(d). Additionally, σ_{sse} is linearly proportional to $\Delta\lambda$ as the spectral-shift error follows a top-hat distribution as visualized in Fig. 2.3(e). Note that the emission spectrum of the fluorescent dye molecule used in the numerical simulation does not perfectly follow a Gaussian distribution. Nevertheless, our results suggested the analytical solution assuming that the Gaussian distribution of the emission spectrum can be used as a relatively accurate guideline to estimate the spectral precision.

We further calculated the optimal SD and the corresponding spectral precision with respect to the photon numbers of the recorded emission spectrum and the background. In the simulation, the photon number of the emission spectrum was increased from 100 to 10000 and the background was increased from 100 to 100000, approximating the practical conditions used in experiments. First, the spectral precision under each condition was calculated as a function of the SD from 0.1 to 20 nm/pixel. The optimal SD and the corresponding spectral precision were found and shown as the 2D contour plot in Fig. 2.4. Interestingly, the SD of the sSMLM system used to achieve the best spectral precision solely depends on the photon number of the spectra image, as indicated by Fig. 2.4(a). By contrast, spectral precision further depends on the total background. When the total background increases, spectral precision decreases, as indicated by Fig. 2.4(b).
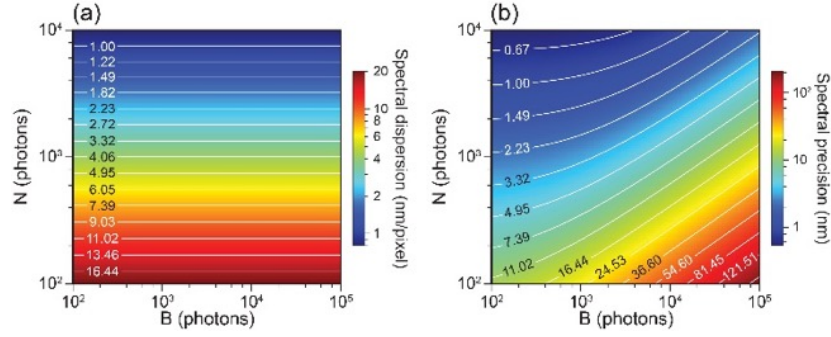
Figure 2.4 (a) 2D contour plot of optimal SD of sSMLM to achieve the best spectral precision. (b) 2D contour plot of the corresponding spectral precision with respect to the photon number of the emission spectrum and the background.

2.4 CONCLUSION AND DISCUSSION

When the localization uncertainty is relatively less significant than the spectral-shift error in actual experiments, we could reduce the spectral-shift error by taking the localized position of individual molecules in the spatial images as a reference for the spectral analysis. This localized position at sub-pixel level allows us to approximately estimate the sub-pixel level spectral shift between the emission spectra of individual molecules. Thus, we could potentially minimize the influence of the spectral-shift error by compensating for the estimated sub-pixel level spectral shift.

In conclusion, we introduced a theoretical model with numerical simulation and analytical solution to analyze spectral precision influenced by the spectral calibration procedure and contributions from all key system parameters. Our study suggests that the best spectral precision can only be achieved with a particular system SD. These findings reveal the delicate balance among key imaging parameters for achieving the optimal spectral precision, which provides unified guidance for developing and optimizing sSMLM technologies.

Chapter 3

Multi-color super-resolution imaging using a tunable spectral dispersion sSMLM system

One of key benefits of label-based optical imaging is multi-color imaging, which allows the simultaneous vitalization of several subcellular nanostructures and the study of their molecular interactions, together with super-resolution optical imaging techniques. Especially for sSMLM, the number of distinguishable fluorescent labels is, in principle, unlimited as sSMLM analyzes the full spectral of different species of labels even if they are highly overlapped.

In this chapter, we develop a tunable spectral dispersion (SD) sSMLM system based on a transmission grating spectrometer. Using the developed system, we characterize the spectral heterogeneities of multiple far-red emitting dyes in a high-throughput manner. In addition, as an experimental extension of the previous chapter, we investigate the influence of SD on the quality of multi-molecular imaging, *i.e.* single-molecule identification performance of fluorophores, when their emission spectra are highly overlapped. The carefully tuning of SD in grating-based sSMLM permits simultaneous three-color super-resolution imaging in fixed cells with a single objective lens at a relatively low photon budget. The results show that an optimal SD needs to be identified to minimize the crosstalk, and therefore mischaracterization, among different fluorescence labels. This chapter is adapted from a previously published article in *Applied Optics* [7].

3.1   INTRODUCTION

Super-resolution microscopy offers an opportunity to study biological processes at nanometer-level spatial resolution [31-38]. Single-molecule localization microscopy (SMLM) requires moderate illumination power and exploits the stochastic fluorescence "blinking" nature of luminescent probes to capture sparsely distributed single-molecule blinking subsets [39]. SMLM techniques can provide a spatial resolution of up to 10 nm; however, the multi-color imaging capability is restricted to only limited numbers of discrete color channels [36, 40]. Indeed, conventional SMLM typically requires two dyes to have emission maxima with at least 100 nm separation to minimize spectral crosstalk [36, 40]. Exchanging ligand strategies enable multiplexing super-resolution imaging by sequentially labeling and subsequent dissociating the target-specific fluorescent DNA probes; however, they require additional sample preparation and prolonged acquisition process [41-43]. Recently developed sSMLM techniques simultaneously record the spatial locations and corresponding emission spectra of single-molecule blinking events, offering new imaging capabilities to resolve, in principle, an unlimited number of fluorescent labels at single-molecule level [3, 5].

In sSMLM, a dispersive element chromatically disperses the photons collected from each single-molecule stochastic blinking event to obtain the single-molecule emission spectrum. Meanwhile, the corresponding spatial information of the blinking event is simultaneously collected in a separate optical path. As a result, sSMLM can capture single-molecule spectra with ultra-high throughput and resolve multiple molecular labels that possess low single-molecule spectral variations where their emission maxima separation can be less than 10 nm [3]. The original Spectrally Resolved Stochastic Optical Reconstruction Microscopy (SR-STORM) collects the

spatial and spectral information of the blinking events via a dual-objective-lens system in two separate paths and disperses the photons in the spectral channel using a prism. Only bright single-molecule blinking events (> 10,000 detected photons) are utilized to reduce the noise uncertainty and its influence on the determination of the spectral signatures. A few examples have been demonstrated since then to collect the emission light only through a single objective lens and then split them into spatial and spectral channels using prisms as the dispersive elements [6, 44]. These techniques permit sSMLM imaging in live cells and probing microenvironment changes in vitro. However, the implementation of these configurations requires a specially modified optical system, typically with a beam splitter, a prism and multiple mirrors, and lenses. The complicated system setup may cause single-molecule signal attenuations and is challenging to integrate the system as a compact add-on module to be used with conventional localization microscopes.

On the other hand, the grating element combines the function of the beam splitter and a dispersive element in grating-based sSMLM systems. They use the minimal number of required optical elements and improve compactness. In fact, it has been demonstrated that placing only a piece of transmission type of diffraction grating between the detector and the conventional localization microscope port enables sSMLM imaging [4]. However, only half of photons are collected through the single objective lens comparing with the dual-objective-lens system, which complicates the multi-color sSMLM imaging acquisition using grating-based sSMLM setups, especially in high fluorescence background biological samples. Indeed, the high dispersions in the spectral channel (referred to as spectral dispersion, SD) used in these systems make it hard to precisely determine the spectral centroid (SC) of dimer blinking events because of splitting photons between zeroth and first-order images. The SD has not been precisely adjusted to achieve

the requisite spectral precision for multi-color imaging in grating-based sSMLM systems (we define spectral precision as the measured standard deviation of single-molecule SC under the collective influence of noise uncertainty and intrinsic single-molecule spectral variations, or spectral heterogeneity).

We developed sSMLM systems that utilize a diffraction grating to obtain the spatial and spectral information of the single-molecule blinking events simultaneously. Using sSMLM, we reported that Rhodamine dyes tagged microtubules assembled in vitro showed significant spectral heterogeneity. Taking advantage of such large spectral heterogeneity, we achieved sub-10 nm spatial resolution via photon regression algorithm [5]. In this article, we report the high-throughput characterization of single-molecule spectral heterogeneity, the SD influence on the identification performance of largely spectral overlapping dyes, and the multi-color super-resolution imaging using transmission diffraction grating-based sSMLM under optimized SD.

3.2 METHODS

3.2.1 sSMLM setup

The schematic of our sSMLM system is shown in Fig. 3.1. A 642-nm CW laser was focused at the back focal plane of a Nikon Ti-U microscope body equipped with a perfect focus module. The light was illuminated onto the sample by a 100 X TIRF objective lens (CFI Apochromat 100X, NA=1.49, Nikon) with an illumination angle slightly smaller than the TIRF module requirement. The emitted photons were collected by the same objective lens. After passing through a tube lens (TL), the collected photons were routed by a mirror (M) to an entrance slit (S), which confines the field-of-view (FOV) of the spatial image, and then split into the zeroth-order and first-order images with a ratio of ~1:3 by a transmission grating (G, 100 grooves/mm, STAR100, Paton Hawskely

Education Ltd.). The grating position relative to the imaging lens (L1, the focal length $f = 50$ mm) was adjusted to tune the SD from 6 to 9 nm/pixel. At the same time, the zeroth-order images remained unmodified, adapting the setup in Fig. 3.1. The SD of 3 nm/pixel was achieved by placing the grating in the collimating beam path between L1 and L2. Photons in the zeroth and first orders were respectively focused onto two different regions of an electron-multiplying charge-coupled device (EMCCD) camera (ProEM 532, Princeton Instrument) by an imaging lens (L2, $f = 50$ mm).
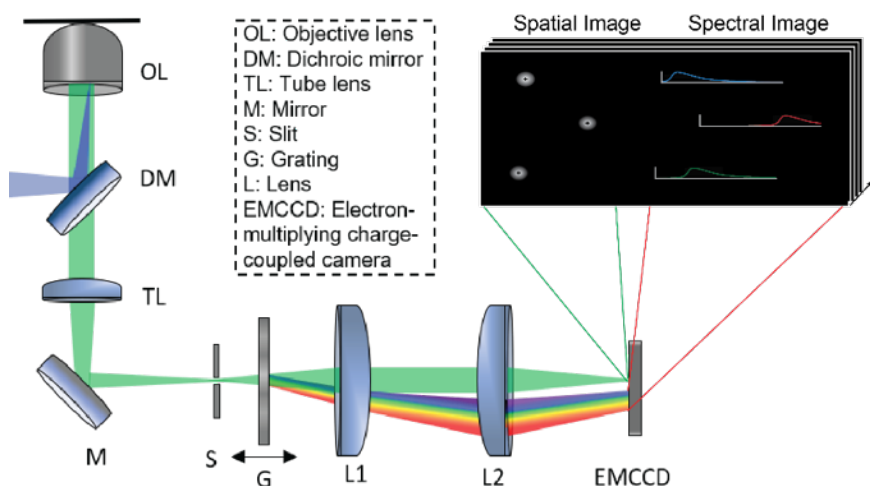
Figure 3.1 Schematic of the sSMLM experimental system. The fluorophores are excited, and then the emitted light is collected by an objective lens and passing through a dichroic mirror, tube lens, mirror and an entrance slit sequentially. Then the light passes through a transmission grating to be split into zeroth-order and first-order light, which provide the spatial and spectral information, respectively, and then two imaging lenses. The inset illustrates the zeroth-order (spatial) and first-order (spectral) images captured by the EMCCD.

3.2.2 Sample preparation

NHS-ester functionalized Alexa Fluor 647 (AF647, Thermofisher), CF660C and CF680 (Biotinum), Dyomics 634 (Dy634, Dyomics Inc.), Cy®5.5 (Sigma) were stored at -20 °C. Primary antibodies mouse anti-TOM20 (Santa Cruz), sheep anti-tubulin (Cytoskeleton), and chicken anti-ATPB (Abcam) were aliquoted and stored at -80 °C. Secondary antibodies Donkey anti-mouse,

anti-sheep IgG, and anti-chicken IgY (Jackson ImmunoResearch) were aliquoted and stored at 4 °C. Fluorescent dye-antibody conjugations were performed by NHS-coupling reaction of the NHS-ester functionalized dyes with the secondary antibodies following a literature protocol [6]. Briefly, Dye (0.4 μL, 5 mM in DMSO), IgG/IgY proteins (100 μL, 1 mg/mL in PBS) and Sodium Bicarbonate (10 μL, 1 M in water) were mixed overnight at 25 °C. The mixture was purified by Nap-5 size exclusion column, concentrated with Amicon Ultra-0.5 Centrifugal Filter units, characterized by a NanoDrop Spectrophotometer to give 1-2 dyes per antibody and stored at 4 °C.

To measure spectral heterogeneity of far-red emitting fluorescent probes, the NHS-ester of Dy634, AF647, CF660C, CF680 and Cy5.5 were conjugated with anti-mouse IgG, adsorbed on the surface of No.1 cover glass at a concentration of 2 μg mL^{-1} for 5 min and rinsed thoroughly with PBS. Before the experiment, a freshly prepared imaging buffer was added to support single-molecule detection.

For multi-color sSMLM imaging, COS-7 cells (ATCC) were grown in DMEM (Gibco/Life Technologies) supplemented with 2 mM L-glutamine (Gibco/Life Technologies), 10% fetal bovine serum (Gibco/Life Technologies), and 1% penicillin / streptomycin (10,000 U mL^{-1}, Gibco/LifeTechnologies) at 37 °C with 5% CO2. The cells were plated on No.1 borosilicate bottom 8-well Lab-TekTM Chambered Coverglass with low confluency. After 48 hours, the cells were fixed in pre-warmed 3% Paraformaldehyde and 0.1% Glutaraldehyde in PBS for 10 min, washed with PBS twice, quenched with freshly prepared 0.1% Sodium Borohydride in PBS for 7 min and rinsed with PBS for three times at 25 °C. The fixed samples were permeabilized with a blocking buffer (3% BSA, 0.5% Triton X-100 in PBS) for 20 min and then incubated with the primary antibodies (Sheep anti-tubulin, 10 μg mL^{-1} for three-color samples and 2.5 μg mL^{-1} for

other samples), (Chicken anti-ATPB, 2 µg mL^{-1}) , (Mouse anti-TOM20, 5 µg mL^{-1}) in blocking buffer for 1h at room temperature and rinsed with a washing buffer (0.2% BSA, 0.1% Triton X-100 in PBS) for three times. The fixed samples were further incubated with the corresponding Donkey secondary antibodies-dye conjugates (Anti-Sheep AF647 and Anti-Mouse CF660C for two-color imaging experiment; Anti-Chicken AF647, Anti-Sheep CF660C and Anti-Mouse CF680 for three-color imaging experiment, 2.5 µg mL^{-1} in blocking buffer) for 40 min, washed thoroughly with PBS for three times at 25 °C and stored at 4 °C.

3.2.3 Image acquisition and data processing

We measured the system's SD using a fluorescent calibration lamp with an entrance slit width of 10 µm. The emission peaks of 487.7, 546.5, 611.6 and 707.0 nm were used to calculate the SD with a first polynomial fit. For the spectral heterogeneity measurement, the entrance slit width was adjusted to 50 µm to reduce the background noise in the spectral channel. For multi-color imaging in cells, the slit width was adjusted to 5 mm to provide an adequate FOV while preventing overlapping between spatial and spectral image channels.

Prior to imaging, an imaging buffer containing 50 mM Tris (pH = 8.0), 10 mM NaCl, 0.5 mg mL^{-1} Glucose Oxidase (Sigma, G2133), 2000 U mL^{-1} Catalase (Sigma, C30), 10% (w/v) D-Glucose, and 100 mM Cysteamine was added to the sample chamber. The imaging experiments were typically finished in one hour or replenished with fresh prepared buffers every hour. The single-molecule blinking lasts for tenths of milliseconds with a few thousand of photons, the spatial locations and the spectral information of each single-molecule blinking were collected with an exposure time of 20 ms. We respectively recorded 5,000, 20,000 and 30,000 frames for spectral heterogeneity measurement, the two-color, and three-color sSMLM imaging reconstructions.

The single-molecule localization of each blinking event was processed using ThunderSTORM [25]. The corresponding single-molecule emission spectrum of every blinking event was obtained using its spectral image with the spatial image as the reference for the calibration process. The spectral detection channel (650 – 750 nm) was selected to collect at least 90% of the dye emission while minimizing the noise uncertainty contribution on the SC of each blinking event. This detection channel corresponds to 34 ×3, 17×3 and 12×3 pixel areas for the SD of 3, 6, and 9 nm/pixel on the camera, respectively. The SC of the emission spectrum was calculated as the weighted average of each spectrum [5]. The single-molecule SCs were used to identify and classify the single-molecule blinking from different dye molecules.

For two-color imaging, we respectively preset the spectral windows for AF647 and CF660C to 683-689 nm and 692-698 nm based on their SCs and spectral precisions. For misidentification characterizations, we imaged AF647-labeled cells and calculated the spectral precision and the number of misidentified single molecules classified into both spectral windows. We applied different photon threshold filters (500-2500) for the spectral channel to discard the blinking events dimmer than the filter thresholds. For spectral precision measurement and multi-color imaging experiments, we filtered out all the blinking events of less than 500 photons. Each single-molecule event was assigned a SC value, and we collected all the events with their SCs within the predefined spectral windows for each dye. In each experiment, 10,000 single molecules were analyzed, and a spectral precision value was provided based on the standard deviation of the spectral centroids of the 10,000 single molecules. In total, 10 samples were analyzed for each condition to provide standard errors.

For three-color sSMLM imaging, 6-nm/pixel SD and 500-photon threshold were applied. We used spatial information of all the single-molecule events after the above classification methods to render the pseudo-color-coded sSMLM images. Based on the spectral precision, the preset spectral windows of 683-689 nm, 692-698 nm, and 703-709 nm for the three dyes (AF647, CF660C and CF680) were used. We firstly acquired AF647, CF660C and CF680 individually labeled cell samples. Using these single-dye stained samples, we calculated the spectral precision of every dye under the same imaging condition and the number of single molecules classified into the other two spectral windows against the total population as the identification fraction. The possibilities of misidentification (channel shift) are 5% between AF647 and CF660C and between CF660C and CF680, and 0.5% between AF647 and CF680.

The morphology-based drift correction was performed according to reference [25] from the original spatial image reconstruction before spectral classification. Prior to sSMLM image rendering, the drift correction file obtained from the original spatial localization image was applied to each classified imaging channel.

3.3   RESULTS

3.3.1   Single-molecule fluorescence spectral signature characterization

We discovered that Rhodamine dyes possess large single-molecule fluorescence spectral heterogeneity when labeled with proteins. Their single-molecule SCs can fluctuate more than 50 nm. Taking this advantage, we employed a spectral regression algorithm to achieve sub-10 nm spatial resolution using sSMLM [5]. In contrast, certain dyes were reported to show reduced spectral heterogeneity at the single-molecule level, and the identification of more than three types

of dye molecules emitted at similar spectral regions based on their single-molecule SC were achieved with prism-based sSMLM system [3].

To validate our sSMLM system for simultaneous multi-color imaging, spectral heterogeneities of multiple far-red emitting fluorophores were firstly measured. We collected single-molecule blinking events with more than 500 photons and a narrow spectral detection window (650-750 nm) to characterize the spectral heterogeneity under minimal noise contribution. The width of the entrance slit was adjusted to 50 μm, which provides a background photon (BP) less than 5 per pixel for each blinking event in the corresponding spectral image. The measurement of SCs variation of red fluorescent nanosphere under the same experimental condition showed a spectral precision of 1.3 nm. This evidence suggested that the spectral variation of more than 1.3 nm should be predominantly contributed by the intrinsic single-molecule fluorescence spectral heterogeneity using this particular system setup. In other words, we can measure the spectral heterogeneity of dyes unambiguously down to 1.3 nm. The FOV in the spatial image was restricted within a 5×120 pixel area. We can collect 5,000-10,000 single-molecule blinking events within 5000 frames (~100 s).
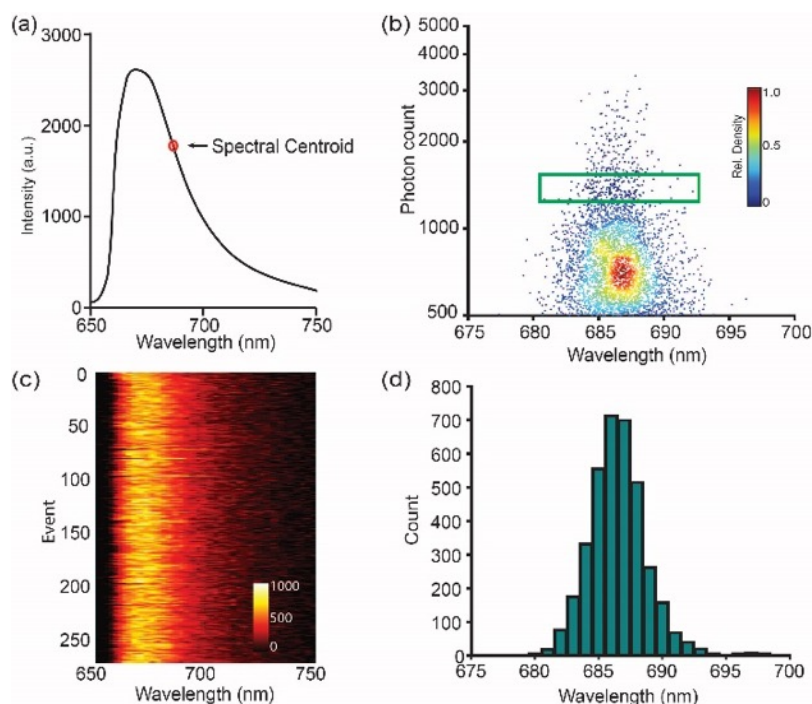
Figure 3.2 Spectral heterogeneity characterization of AF647. (a) The averaged emission spectrum of AF647 and its calculated spectral centroid (SC) position; (b) Scatterplot of photon count vs. single-molecule SC position of 6,132 AF647 single-molecule blinking events with the rectangular region highlights 260 single-molecule events with photon count from 1200-1500 and their emission spectra shown in (c); (d) Histogram of SC distribution of all the 6,132 single-molecule blinking events. Scale bar refers to the relative density of single-molecule distribution in (b) and relative intensity in (c).

Table 3.1 Single-molecule fluorescence emission signature of dye-protein conjugates.

Dye	λ_{Em} (nm) [a]	λ_{SC} (nm) [b]	σ_{SH} (nm) [c]
Dy634	664	682	1.9
AF647	670	686	2.1
CF660C	688	695	3.1
Cy5.5	697	701	3.5
CF680	704	706	2.2

[a]λ_{Em}: averaged emission maximum; [b]λ_{SC}: averaged emission spectral centroid; [c]σ_{SH}: standard deviation of single-molecule spectral heterogeneity.

The averaged emission maximum (670 nm) and emission SC (686 nm) of AF647-IgG conjugates adsorbed on glass slide measured by the sSMLM system (Fig. 3.2(a)) agreed well with

literature reports [17]. The scatterplot of the emitted photon number against single-molecule SC of 6,132 blinking events revealed a relatively small SC variation primarily from 680 nm to 692 nm (Fig. 3.2(b)). Figure 3.2(c) shows that the 260 single-molecule emission spectra with 1200-1500 detected photons (highlighted by the green box in Fig. 3.2(b)) have negligible spectral changes among each other. The histogram of SC distribution from all the 6,132 detected blinking events from AF647 depicted a relatively low spectral heterogeneity with a standard deviation (σ_{SH}) of 2.1 nm, as shown in Fig. 3.2(d). The measured spectral heterogeneities of Dy634, CF660C, CF680, and Cy5.5, which emit within similar far-red spectral regions, showed slightly different values of 1.9, 3.1, 3.5, and 2.2 nm, respectively. The measured spectral heterogeneities are stable for at least 1 hour after adding fresh imaging buffer with relatively stable pH. Their measured averaged emission spectral maxima are consistent with literature values, as shown in Table 3.1 [3, 17]. These spectral heterogeneities provide the possibility to distinguish dye labels, where their SCs are only 10 nm apart, relying on the single-molecule SCs, and the simultaneous multi-color super-resolution imaging using a single objective lens.

3.3.2 Simultaneous two-color sSMLM imaging in cells under different spectral dispersions

Both intrinsic single-molecule fluorescence spectral heterogeneity and background noise affect the spectral precision and determine the number of dyes or imaging channels that can be simultaneously resolved in sSMLM using SC classification method. The spectral heterogeneities of these far-red emitting dyes were remarkably low to permit the multi-color sSMLM imaging. As an example, the misidentification between AF647 and CF660C in the pre-defined spectral channels is only 2.0%. However, because of the limited photon budget and relatively high intracellular

background, the spectral precision might significantly decrease, especially when the SD is relatively high (SD < 4 nm). Instead, a lower SD of 5-7 nm/pixel could provide relatively stable spectral precision over high background conditions according to our theoretical predictions [19]. To further investigate the SD effect on multi-color sSMLM imaging experimentally, we performed two-color sSMLM imaging of COS-7 cells under different SDs where microtubule and mitochondria were labeled with AF647 and CF660C, respectively.
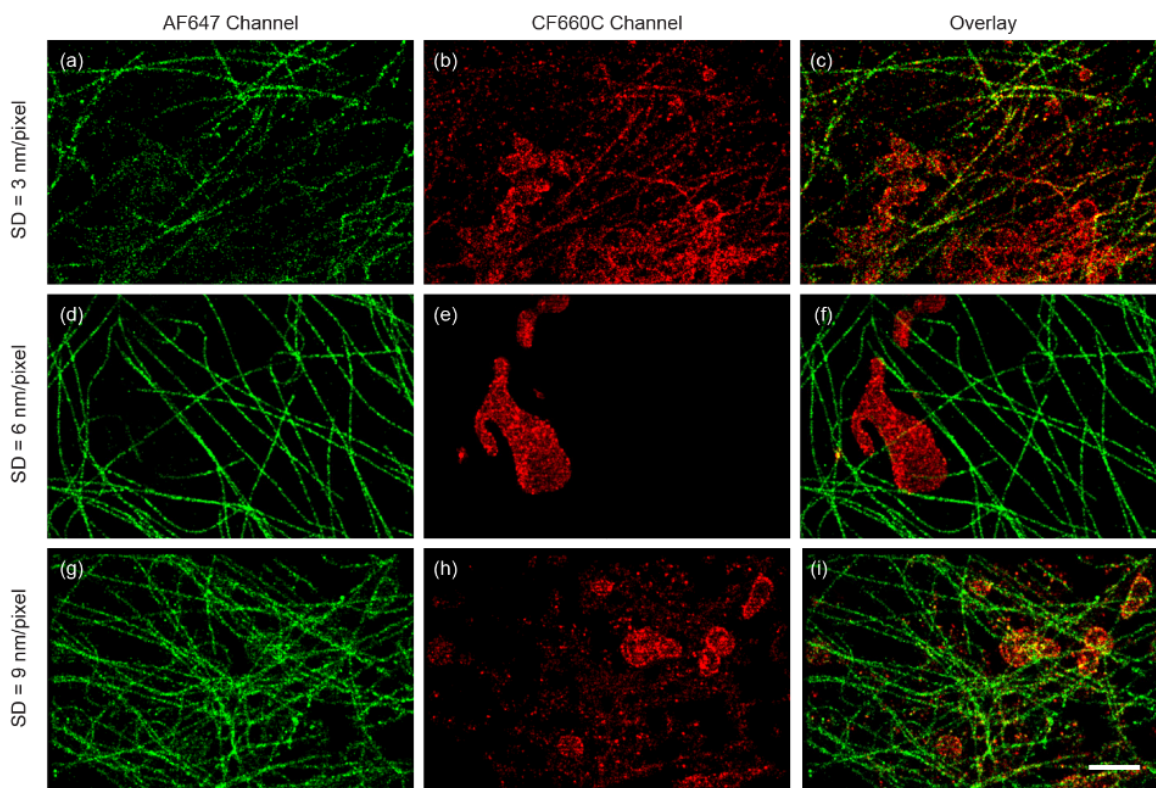
Figure 3.3 Two-color sSMLM images of AF647 labeled microtubule and CF660C labeled mitochondria in COS-7 cells at different SDs (a-c, 3 nm/pixel), (d-f, 6 nm/pixel) and (g-i, 9 nm/pixel) respectively. The AF647 (a, d and g) and CF660C (b, e, and h) channels and the overlay images (c, f, and i) were collected with single-molecule SC of 683-689 nm and 692-698 nm respectively. (Scale bar = 2 μm)

At the SD of 3 nm/pixel, the microtubule and mitochondria structures appeared in both AF647 and CF660C channels (Figs. 3.3(a)-(c)). The coordinate-based co-localization (CBC) analysis [45] indicated a CBC value of 0.19, suggesting significant overlapping between the two channels as a

result of high misidentification rate and low spectral precision. These experimental evidences indicated that the relatively high intracellular background (BP = ~50/pixel) restricts the system performance to unambiguously distinguish dyes that emission spectra are only 9 nm apart at the SD of 3 nm/pixel. Presumably, limited number of photons collected in the spectral channel were dispersed to a relatively large area on the camera, and the spectral precision was affected by noise uncertainty at such high BP.

Then we conducted two-color sSMLM imaging under 6-nm/pixel SD. Comparing to the 3-nm/pixel case, the microtubule and mitochondria structures respectively showed only in the AF647 and CF660C channels with a CBC value of 0.01, which suggested negligible overlapping between the two channels (Figs. 3.3(d)-(f)). Furthermore, the two-color imaging at the SD of 9 nm/pixel showed increased overlapping between the two channels with a CBC value of 0.08 (Figs. 3.3(g)-(i)). In the overlaid image (Fig. 3.3(i)), yellow-orangish color was observed on the mitochondria region, which indicated that misidentified single molecules from the tubulin channel. Therefore, the image quality degraded in SD of 9 nm/pixel comparing to 6 nm/pixel.

3.3.3 Two-color sSMLM imaging performance characterization

Our sSMLM simultaneously captures the spatial and spectral information of single-molecule blinking events. For achieving high spectral precision, 75% of the total photons were allocated to the first order image while the rest 25% of total photons were allocated into the zeroth order for spatial localization. We achieved localization uncertainty of 17-23 nm (Fig. 3.4(a)) which were comparable with literature values in the conventional SMLM under similar photon budget [17]. Notably, the spatial resolution was independent of SD since the blinking signals in the zeroth order remained unmodified. In addition, this sSMLM setup provides the opportunity to systematically

tune and optimize SD for multi-color imaging with simply adjusting the grating position relative to the imaging lens (L1).

Using the same sSMLM setup, we quantified the misidentification under different SDs by imaging AF647 labeled microtubules in COS-7 cells as examples at different background levels. In the aforementioned spectral heterogeneity measurement with SD of 3 nm/pixel, low BP < 5/pixel were detected. Within 6,132 detected AF647 single molecules, 122 single-molecule SCs locate in the spectral region of 692-698 nm, which was the spectral window we preset for CF660C. These values suggested a spectral precision of 2.1 nm and a misidentification rate of 2.0% between AF647 and CF660C that SCs are 9 nm apart (Figs. 3.4(b)-(c)). Then we adjusted the entrance slit to 5 mm to increase the FOV to 120×120 pixels (19.2×19.2 µm2) for imaging cell samples. The BP increased to ~ 50/pixel when we imaged the COS-7 cells labeled with AF647 with a concomitant decrease of spectral precision down to 6.4 nm (Fig. 3.4(c)). Under this condition, 29,862 from 100,546 detected single-molecule SCs located in the CF660C spectral window (Fig. 3.4(b)). In such high intracellular background conditions, the high misidentification rate of 29.7% restricts the imaging capability of our multi-color sSMLM system (Fig. 3.4(b)). Although applying higher photon threshold filter (2500) can decrease the misidentification rates to 5.4 % when BP was ~ 50/pixel (Fig. 3.4(b)), the number of collected localization events was not enough to render a good-quality super-resolution image with continuous microtubules until dyes photobleaching.
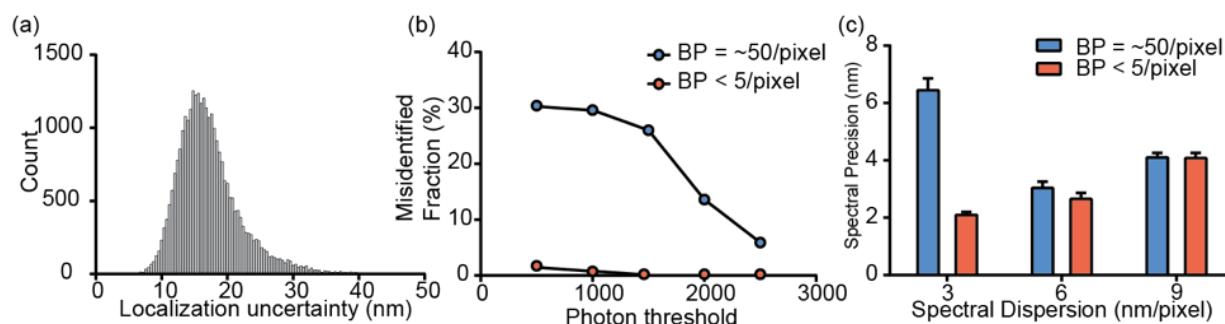
Figure 3.4 sSMLM imaging parameter characterizations. (a) Localization uncertainty of sSMLM images of COS-7 cells which the microtubule and mitochondria were labeled with AF647 and CF660C respectively; (b) Misidentified fraction of AF647 as CF660C in a pre-determined collection window of 692-698 nm based on the single-molecule SCs under different BP of 5 and 50 per pixel respectively with different photon thresholds of AF647 labeled microtubules of COS-7 cells at 3 nm/pixel SD; (c) Spectral precision measurements at different SDs of AF647 labeled microtubules in COS-7 cells. Error bars indicate the standard errors in each condition (Sample size for each condition = 10).

Limited number of photons collected in the spectral channel were dispersed to a large area (34×3 pixel) on the camera and resulted in low spectral precision in the case of 3 nm/pixel SD. In turn, decreasing the dispersion may increase the signal to background ratio and spectral precision, especially for sSMLM imaging in cells under high background conditions [19]. Remarkably, the adjustment of SD to 6 and 9 nm/pixel resulted in higher spectral precisions of 3.2 nm and 4.1 nm for BP of 50, respectively (Fig. 3.4(c)). These results were consistent with our CBC analysis that 6 nm/pixel SD showed the optimal imaging performance and agreed well with our numerical simulation studies [19]. Presumably, a sub-pixel systematic error in mapping the spatial distribution of the single-molecule blinking events to the associated spectral signatures during the spectral calibration procedure occurs at the SD of 9 nm/pixel thus decreasing the spectral precisions to 4.1 nm under these background conditions. Furthermore, the low spectral precisions appeared in both 3 and 9 nm/pixel resulted in incorrect classification of a large amount (~30% and 12% respectively) of single molecules in the two channels and degraded the image quality as discontinuous tubulin skeleton and scattered dots were observed (Figs. 3.3(a)-(c) and 3.3(g)-(i)).

In short, the SD of 6 nm/pixel showed the optimal spectral precision that tolerated relatively high intracellular background and was determined for acquiring multi-color sSMLM imaging.

3.3.4   Multi-color super-resolution imaging of COS-7 cell

We set the SD to 6 nm/pixel in simultaneous three-color sSMLM imaging experiments. The independent examination of the SC of AF647, CF660C and CF680 at the SD of 6 nm/pixel under the identical imaging condition labeled the microtubule structures of COS-7 cells demonstrated spectral precisions of 3.2, 4.3 and 3.1 nm, respectively (Fig. 3.5(a)). The relatively high spectral precision enabled the identification of the three dyes based on their SC positions. The classification of the SCs into three channels based on their maximal probability of SC at 683-689 nm, 692-698 nm and 703-709 nm resulted in more than 95% separation between AF647 and CF660C as well as between CF660C and CF680, where the separation between AF647 and CF680 was more than 99.5% (Fig. 3.5(b)).
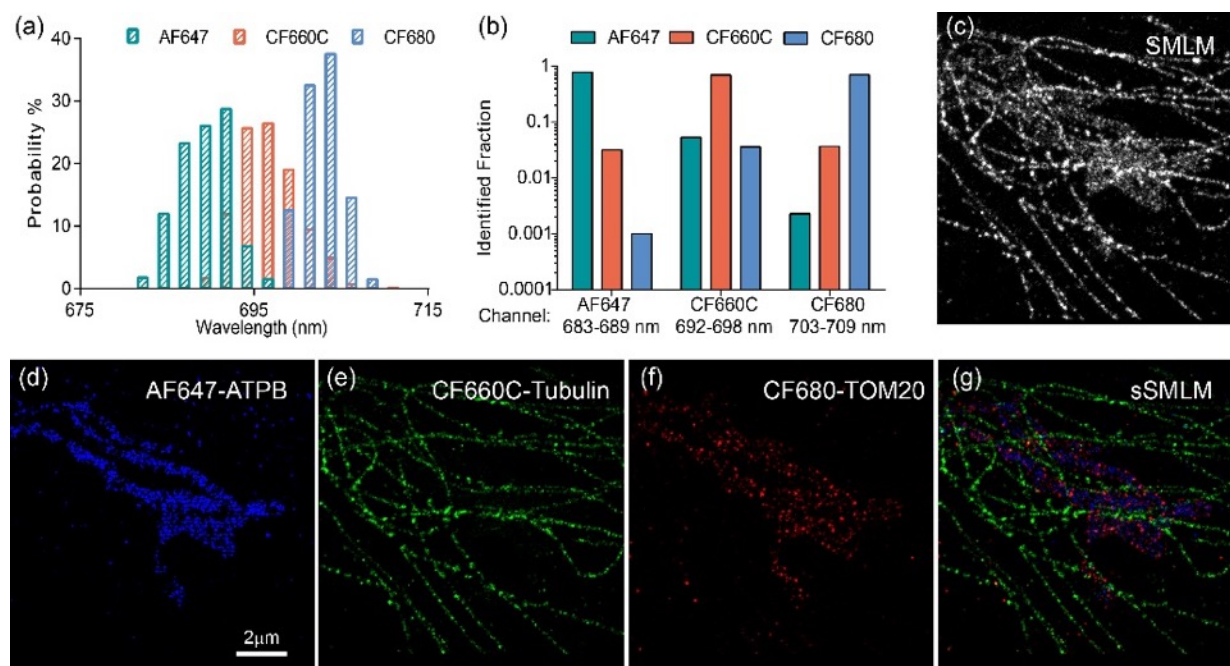
Figure 3.5 Multi-color sSMLM imaging of COS-7 cells. (a) SC distribution of AF647, CF660C and CF680; (b) Identification fraction of the three dyes in the preset channels; (c) SMLM imaging of a COS-7 cell which the ATPB, Tubulin and TOM20 proteins were labeled with AF647, CF660C and CF680 respectively; (d-f) pseudo color-coded images of the same sample in (c) classified in three spectral windows based on their spectral signature and the sSMLM image (g).

A conventional SMLM image of a COS-7 cell immunofluorescent labeled with AF647, CF660C, and CF680 to the ATP synthase (ATPB), Tubulin, and Mitochondrial Outer Membrane translocase complex (TOM20), respectively, as shown in Fig. 3.5(c). The tubulin cytoskeleton can be partially distinguished based on its morphology. However, the large overlapping region between the three targets of interests remained unresolved in the single far-red detection channel (Fig. 3.5(c)). Based on their respective SCs, sSMLM separated the three labels with high specificity as shown in Figs. 3.5(d)-(f). The distinct microtubule structures were exclusively located in CF660C channel, and the unresolved region in conventional SMLM can be clearly distinguishable in the pseudo color-coded images (Fig. 3.5(e)). Both the ATPB and TOM20 signals showed elongated patterns (Figs. 3.5(d) & 3.5(f)) while the TOM20 were located at the periphery of ATPB as shown in the overlaid sSMLM image (Fig. 3.5(g)). This feature was consistent with

the protein locations that TOM20 labels highlight the outer membrane of mitochondria and ATPB resides in the inner membrane of mitochondria [3]. As a result, we demonstrated that simultaneous multi-color sSMLM imaging could be achieved in immunostained cells using a single far-red detection channel with optimal SD at 6 nm/pixel.

3.4   CONCLUSION

We achieved simultaneous acquisitions of single-molecule positions and corresponding spectra of fluorescent probes with grating-based sSMLM using a single objective lens. We showed that both intrinsic single-molecule fluorescence spectral heterogeneity and noise uncertainty affect the system performance for identifying dyes emitting in close spectral region. Carefully tuning the spectral dispersion provides a suitable spectral precision for simultaneously multi-color imaging of multiple dye species with narrow spectral centroid shifts (~10 nm). We showed that using a SD of 6 nm/pixel the grating-based sSMLM can resolve three molecular labels in fixed cells at the same time with nanometer resolution. We anticipate that sSMLM will play an important role in investigating structural and dynamical biological processes involving interactions of multiple molecules.

Chapter 4

3D super-resolution imaging using biplane sSMLM

Along with spectroscopic single-molecule imaging, extending sSMLM's imaging capability from two-dimensional (2D) to three-dimensional (3D) in the spatial domain is essential for uncovering rich information about single molecules for the fundamental understanding of subcellular structures. For 3D sSMLM imaging, we found that implementing the biplane method based on the already-established spatial and spectral imaging channels offers a much more attractive solution. It allows for more efficient use of the limited photon budget and provides homogeneous lateral resolution compared with the astigmatism-based method using a cylindrical lens. In this chapter, we report 3D biplane sSMLM and demonstrate its multi-color 3D imaging capability by imaging microtubules and mitochondria in fixed COS-7 cells immunostained with Alexa Fluor 647 and CF 660C dyes, respectively. We showed a lateral localization precision of 20 nm at an average photon count of 550, a spectral precision of 4 nm at an average photon count of 1250, and an axial localization precision of 50 nm. This chapter is adapted from a previously published article in *Optica* [46].

4.1 INTRODUCTION

Spectroscopic single-molecule localization microscopy (sSMLM) has recently emerged as a new tool for obtaining molecular insights into cellular dynamics by capturing the spatial information of single molecules with their inherent spectroscopic signatures [3-6]. sSMLM enables direct observation of the nanoscopic features of biological systems beyond the diffraction limit. Its ability to probe spectroscopic variations associated with interactions between single

molecules and their local environment has allowed several functional studies to reveal subcellular hydrophobicity changes and photochemical transformation with single-molecule sensitivity [4, 11, 12]. In addition, by identifying individual molecules based on minute differences in their emission spectra, sSMLM has demonstrated its versatile imaging applications, including multi-color imaging, fluorescent impurity rejection, chemical recognition, and high throughput fluorescence spectroscopy at the single-molecule level [7, 15, 47].

Along with spectroscopic single-molecule imaging, extending sSMLM's imaging capability from 2D to 3D in the spatial domain is essential for uncovering rich information about single molecules for fundamental understanding of subcellular structures. In conventional SMLM, several methods have been developed to unambiguously determine the axial position of single molecules together with their in-plane lateral coordinates [48-62]. The 3D SMLM imaging is commonly realized by manipulating the point-spread-function (PSF) using artificially introduced astigmatism [48, 49]; however, this method is inherently sensitive to optical aberrations in thick samples [50]. In addition, the ellipticity of the PSF affects the localization precision, thus causing inhomogeneous lateral precision along the axial position [52]. Alternatively, the biplane method encodes the axial position of the same single molecules into distinctly defocused PSFs at two axially separated image planes [50-52]. In this approach, the lateral precision is not affected by the depth variation. However, this method divides the total number of photons emitted into two detection channels and reduces the photon budget in each channel, which consequently restricts the localization precision in either channel. The third method is based on 4π interferometric configuration [54, 55]. Despite its outstanding performance, its usage is restricted to a thin sample

limited by its imaging depth. Additionally, the alignment procedure using multiple cameras is quite demanding.

With sSMLM, researchers have already reported 3D imaging capability [3, 27, 63]. We and other groups have implemented 3D imaging using the astigmatism-based approach [3, 63]. Along with its drawbacks described above, this method suffered from the reduced signal-to-noise ratio (SNR) in sSMLM when the PSF were considerably enlarged. More importantly, it caused challenges in wavelength calibration, as the two beam paths for spatial and spectral images experienced different spherical aberrations, which is mainly caused by inserting a cylindrical lens only into the zeroth order (spatial imaging path). Reported by Smith et al. [64], a diffractive optic was used to obtain 3D spatial information of single molecules and the emission color, but it offers relatively low spectral precision and thus limits the range of functional imaging applications in sSMLM.

Methods focused only on manipulating PSFs in spatial images using double-helix PSFs and spherical aberration were also reported for SMLM [56, 61, 62]. These adaptive optics-based 3D imaging methods, which use a spatial light modulator or a deformable mirror, not only increase the complexity of system alignment but also result in undesirable attenuation of the photons, especially in sSMLM.

In fact, sSMLM fundamentally suffers from a limited photon budget because the emitted photons from single molecules need to be divided into two detection channels to simultaneously capture the spatial and spectral images. This fundamental constraint restricts the direct adoption of many different approaches for 3D imaging. Although the spectral image contains both the spatial

and spectral information of single molecules, only the spectral information has been used and the spatial information was often ignored in sSMLM.

Here, we present the 3D biplane sSMLM, which provides simultaneous acquisition of 3D spatial information and the spectroscopic signatures of single molecules by taking advantage of the two already-existing spatial and spectral imaging channels. By recognizing that sSMLM already divides the photons into two independent channels, 3D imaging can be efficiently implemented using the biplane method without the need for excessive additional optical elements or tedious modification of the system only in the spatial channel. Therefore, the drawback of dividing photons into two imaging channels becomes an added benefit. In this work, we demonstrate spectroscopic 3D imaging of single molecules using 3D biplane sSMLM and show multiplexed 3D imaging of subcellular structures in fixed cells.

4.2 METHODS

4.2.1 3D biplane sSMLM system
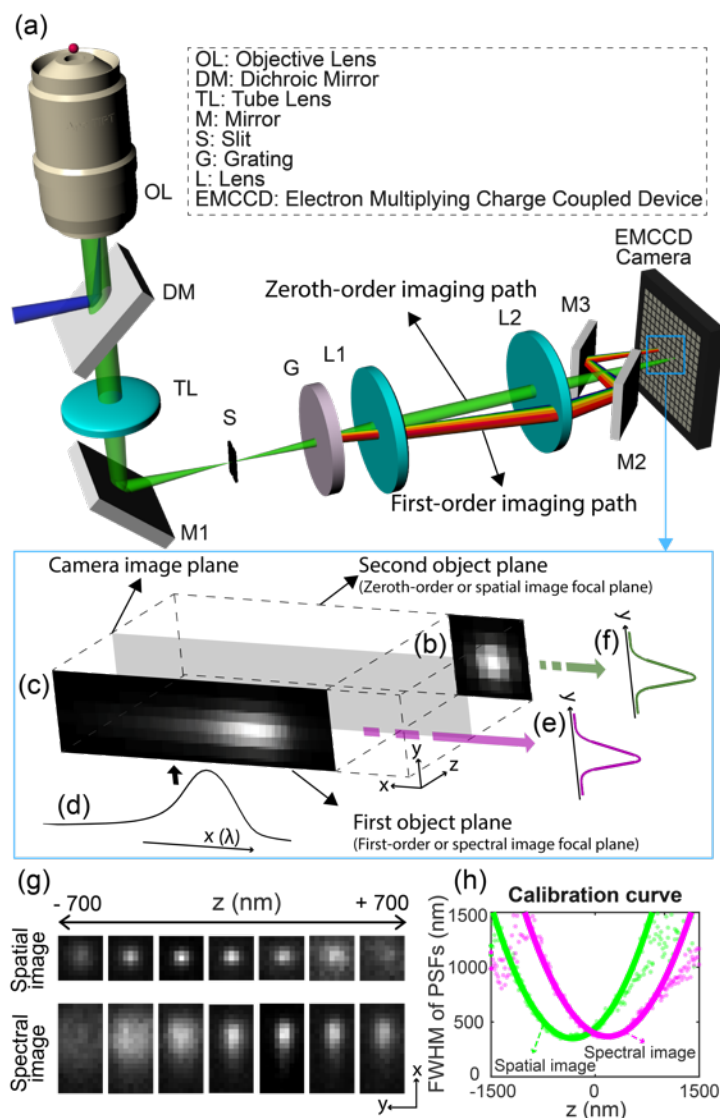
Figure 4.1 The schematic (a) and working principle (b-f) of 3D biplane sSMLM. The detected spatial image (b) and spectral image (c) of a single-molecule emission. The spectral image (c) is the result of the convolution of the diffraction-limited PSF of individual stochastic fluorescent-emitting molecules in the spectral imaging plane and the linearly spread spectroscopic signature (d). By integrating the spectral and spatial images along the x-axis, 1D PSF_ys in (e) and (f) are retrieved from both images and used for biplane imaging. (g) The experimentally acquired spatial (top row) and spectral (bottom) images at the different axial positions from single emitters. (h) The experimentally obtained depth calibration curve.

Figure 4.1(a) shows the schematic of the 3D biplane sSMLM. To divide the emitted photons into the zeroth- and first-order imaging paths for simultaneous spatial and spectral imaging, we added a diffraction grating to a conventional SMLM system. First, we focused a 640 nm CW laser to the back aperture of the objective lens (CFI Apochromat 100X, NA =1.49, Nikon) by a dichroic beamsplitter (FF649-DI01-25X36, Semrock). We offset the excitation beam from the optical axis of the objective lens for highly inclined and laminated optical sheet (HILO) illumination. Then, the emitted fluorescence photons were transmitted to the intermediate image plane by a mirror after passing through an emission filter (BLP01-647R-25, Semrock) and a tube lens inside an inverted microscope body (Eclipse Ti-U, Nikon). We inserted a slit in front of the spectrometer to confine the field-of-view (FOV) of the spatial distribution of the emitted fluorescence at the intermediate image plane. Subsequently, we inserted a transmission grating, with a ratio of 1:3 between the zeroth order and the first order in the far-red spectral range (100 grooves/mm, Star analyzer 100, Paton Hawksley Education Ltd.), to separate the spatial and spectral images.

The relative positions between the grating and the intermediate image plane determined a pixel-wavelength relationship, referred to as the spectral dispersion (SD) (nm/pixel) in the spectral image [19]. We used a SD of 8 nm/pixel. In addition, after a relay optics (focal length = 150 mm) we added a pair of mirrors in the first-order (spectral) imaging path in front of the electron-multiplying charge-coupled device (EMCCD) camera (iXon 897, Andor) to introduce a delay line. This delay created an axial separation of 500 nm between the spatial and spectral imaging object planes for biplane imaging. We placed the EMCCD camera in the middle of the two axially separated object planes, which enabled the simultaneous capturing of the spatial and spectral

images with different PSF sizes corresponding to the relative axial position to the optical focal plane. Except for the pair of mirrors, no additional optical elements were necessary.

Figures. 4.1(b)-(f) show the working principle of 3D biplane sSMLM. Figures 4.1(b) and 4.1(c) are illustrations of the detected spatial and spectral images of a single-molecule emission. Note that the camera image plane (the gray plane) is in the middle of the zeroth-order (or spatial imaging) and first-order (or spectral imaging) focal planes. The spectral image shown in Fig. 4.1(c) is the convolution of the PSF of individual stochastic fluorescent-emitting molecules in the spectral imaging plane and the linearly spread spectral profile shown in Fig. 4.1(d). Therefore, we can retrieve the emission spectrum (Fig. 4.1(d)) and the one-dimensional (1D) PSF (defined as PSF_y, Fig. 4.1(e)) by integrating the spectral image along the y-axis and x-axis, respectively. Meanwhile, we can calculate similar 1D PSF_y from the spatial image, as shown in Fig. 4.1(f). These two 1D PSF_ys collectively provide the z-axis information of the fluorescent emitter with respect to the camera image plane. Meanwhile, the emission spectrum, shown in Fig. 4.1(d), is still used for spectroscopic analysis. Experimentally acquired spatial (top row) and spectral (bottom) images at different axial positions (-700 nm to 700 nm) from single molecules are shown in Fig. 4.1(g).

For every single-molecule emission, we integrated the simultaneously acquired spectral and spatial images along the x-axis to extract the 1D PSF_ys from the two focal planes, as shown in Figs. 4.1(e) and 4.1(f). We then took the ratio of the full-width-at-half-maximum (FWHM) values of the two 1D PSF_ys and compared it with an experimentally obtained depth calibration curve (Fig. 4.1(h)) to determine the axial position. By combining with x-y localization from the spatial image, we can achieve 3D localization.

4.2.2 Definition of spectral dispersion

Spectral dispersion (SD) (nm/pixel) is defined as the wavelength range per individual pixel. Assuming the SD is linear in a given sSMLM system, it can be expressed by

$$\Delta\lambda = W_p \times R_d = W_p \times \frac{dcos\theta}{f \times m} \tag{4.1}$$

where W_p is the camera pixel size (µm); R_d is the reciprocal linear dispersion; d is the groove spacing; θ is the angle of diffraction at the mth order; m is the order of the maxima (typically 1); and f is the effective focal length of the relay optics in the spectrometer, which is defined as Df_2/f_1, where D is the distance from the grating position to the intermediate image plane; f_1 is the focal length of the collimating lens (L1); and f_2 is the focal length of the focusing lens (L2). Accordingly, it shows the separation of wavelength (nm) per interval distance (µm). In this work, the SD was adjusted to 8 nm/pixel.

4.2.3 Spectral calibration procedure

In order to obtain the emission spectra of single molecules from the recorded spectral images, a spectral calibration procedure is required and is specific to individual sSMLM systems. Using a calibration light source (Neon lamp, 6032, Newport), we first captured a reference image, which includes a straight line confined by a narrow slit and multiple spectral lines. These multiple spectral lines in the spectral image correspond to the emissions centered at a specific wavelength of the calibration light source, whereas the straight line in the spatial image corresponds to the slit position. We used two main emission peaks at 640.23 and 703.24 nm. Then, the pixel positions and wavelengths of these spectra lines were fitted by a polynomial function. We used the fitted

function to establish the spatial-spectral mapping relationship between the spatial image and spectral image. We point out that a grating offers a linear SD within the spectral range.

Next, the obtained spatial-spectral mapping relationship was applied to individual stochastic emission events. We used the spatial images of the emission events as the reference locations for the spectral analysis. Accordingly, we arranged individual spectroscopic signatures in the spectral window with the same wavelength range. Finally, by integrating the spectral images along the y-axis, we obtained the emission spectra of individual emission events.

4.2.4 Multi-color 3D sSMLM image reconstruction

To acquire a 3D calibration curve, we first captured a few PSFs in the spatial and spectral images at different axial positions using far-red nanospheres (200-nm diameter; F8807, Invitrogen). We translated the sample from -1.5 μm to 1.5 μm along the z-axis with a step size of 25 nm, as shown in Fig. 4.1(h). Then, we extracted the 1D PSF_ys in both the spatial and spectral images, as shown in Figs. 4.1(e) and 4.1(f), by integrating the intensities along the x-axis. After measuring the FWHM values of the two 1D PSF_ys, we calculated the ratio between them along the z-axis to use as the depth calibration curve.

We reconstructed 2D images using ThunderSTORM [25] and 3D images using customized MATLAB codes. For each individual molecule, we first localized its x-y positions in the spatial image and then calculated the PSF_y ratio between the spatial and spectral images to obtain its z position based on the depth calibration curve. Together with the spectral centroid calculated from the spectral image, we can obtain a 4D array for all individual molecules. During the spectral analysis, we rejected emissions with a detected intensity below 750 photons. We numerically

corrected the slight magnification difference between the spatial and spectral imaging channels caused by their different pathlengths before image reconstruction.

4.2.5 Sample preparation

COS-7 cells (ATCC) were cultured in Dulbecco's Modified Eagle Medium (DMEM, Gibco/Life Technologies) supplemented with 2 mM L-glutamine (Gibco/Life Technologies), 10 % fetal bovine serum (Gibco/Life Technologies), and 1 % penicillin/streptomycin (100 U mL^{-1}, Gibco/LifeTechnologies) at 37 $^{\circ}$C with 5 % CO2. The cells were plated on a No. 1 borosilicate-bottom 8-well Lab-TekTM Chambered Coverglass with ~ 30 % confluency. After 48 h, we fixed the cells in pre-warmed 3 % Paraformaldehyde and 0.1 % Glutaraldehyde in PBS for 10 min, washed with PBS twice, quenched with freshly prepared 0.1 % Sodium Borohydride in PBS for 7 min and rinsed twice with PBS at 25 $^{\circ}$C. The fixed samples were permeabilized with a blocking buffer (3 % BSA, 0.5 % Triton X-100 in PBS) for 20 min and then incubated with the primary antibodies (Mouse anti-TOM20, 2.5 μg mL^{-1}, Santa Cruz, sc-17764; Sheep anti-Tubulin, 2.5 μg mL^{-1}, Cytoskeleton, ATN02) in blocking buffer for 1 h. The samples were rinsed in a washing buffer (0.2 % BSA, 0.1 % Triton X-100 in PBS) three times for 5 min and further incubated with the corresponding secondary antibodies-dye conjugates (Donkey anti-mouse Alexa Fluor 647 and/or anti-sheep CF660C, 2.5 μg mL^{-1}, degree of labeling = 1-2 dyes per antibody, prepared according to the literature [17]) for 40 min. Finally, the cells were washed thoroughly with PBS three times for 5 min and stored at 4 $^{\circ}$C. Before imaging acquisition, an imaging buffer (pH = ~8.0) containing 50 mM Tris, 10 mM NaCl, 0.5 mg mL^{-1} Glucose Oxidase (Sigma, G2133), 2000 U mL^{-1} Catalase (Sigma, C30), 10 % (w/v) D-Glucose, and 100 mM Cysteamine replaced PBS in the sample chamber and was imaged without further preparation.

4.3   RESULTS

4.3.1   3D super-resolution imaging

To demonstrate the 3D imaging capability of this new biplane design, we imaged COS-7 cells with Alexa Fluor 647 (AF647)-labeled mitochondria. The illumination power was ~ 15 kW/cm^2, the EMCCD exposure time was 20 ms, and the axial separation between the spatial and spectral images was 500 nm. The FOV of the acquired images was ~ 15 × 30 μm^2. The average density of the fluorophores was < 15 emitters per raw image (camera frame). The number of raw images was 25,000 and the total acquisition time was ~ 9 min for one reconstructed super-resolution image. Figure 4.2(a) is the overall projection image of the reconstructed 3D sSMLM, with pseudocolors corresponding to the z-axis positions. We acquired three 3D biplane sSMLM datasets, with 450-nm axial translation at each acquisition, and combined them to form the overall 3D dataset, covering a depth range of 1.5 μm. Figures 4.2(b), 4.2(c), and 4.2(d) are the projection images from three 200 nm-thick volumes, as highlighted in Fig. 4.2(a). Figures. 2(e) and 2(f) are cross-sectional images of mitochondria along the y-z and x-z planes, respectively, as highlighted in Fig. 4.2(a). As we can see, the nanostructures of the mitochondria are clearly distinguished along all three-dimensional directions.

To characterize the performance of 3D biplane sSMLM, we experimentally quantified the spatial localization precisions and spectral precision using fluorescent nanospheres and compared them with theoretical values. As shown in Fig. 4.3, we confirmed that the experimentally obtained values agree well with the theoretical expectations. We also compared the localization precision and spectral precision of 3D biplane sSMLM with that of astigmatism-based 3D sSMLM. As shown in Fig. 4.4, both methods showed comparable spatial precisions and spectral precision. We further measured the depth variation of the ratio between the localization precisions along the x

and y directions (defined as lateral precision isotropy) and compared the depth variations of the precision isotropy in both biplane- and astigmatism-based 3D imaging methods. As shown in Fig. 4.5, the biplane-based method had a nearly uniform lateral precision isotropy within the entire 800-nm depth range. In contrast, the lateral precision isotropy varied significantly along the depth in the astigmatism-based method due to non-uniform photon densities along the x and y axes induced by astigmatism [50, 52].
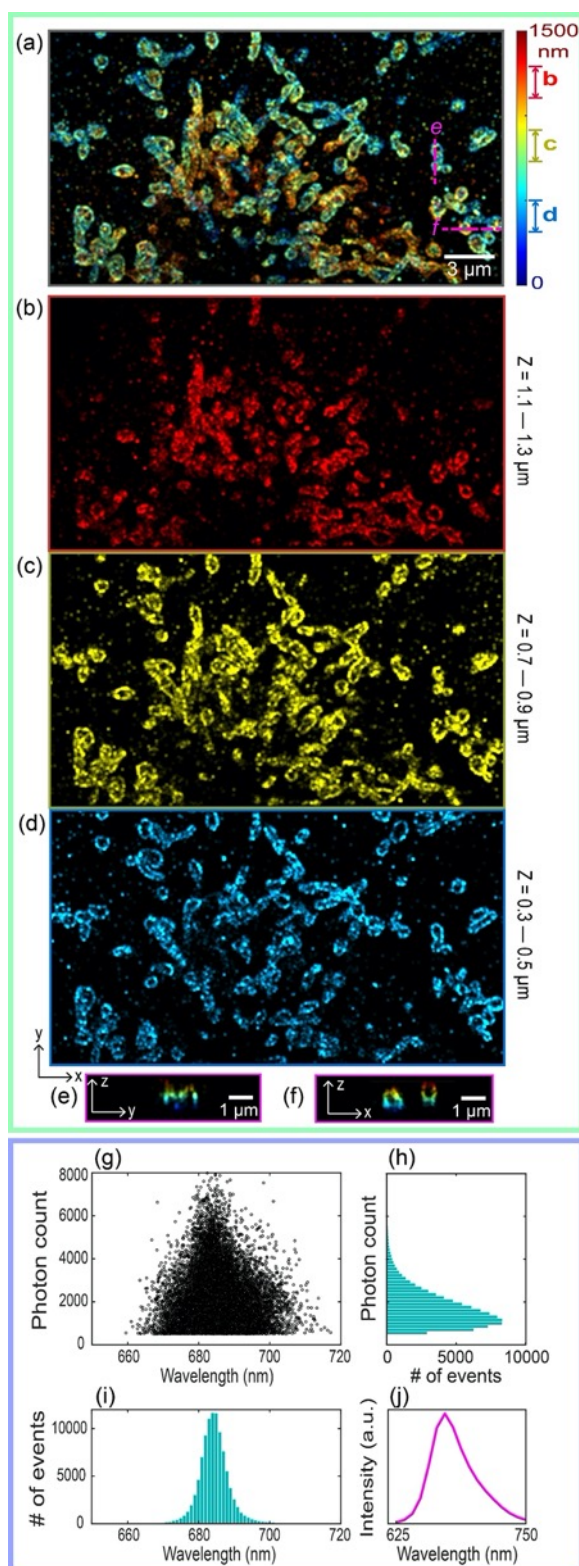
Figure 4.2 (a) The overall projection image of the reconstructed 3D sSMLM, with pseudocolors corresponding to the z-axis positions of individual molecules. (b-d)

The projection images from three 200 nm-thick sections, as highlighted in (a). The cross-sectional images in the y-z plane (e) and x-z plane (f) corresponding to the three magenta-dashed lines, as highlighted in (a). (g-j) Spectral analyses of same single AF647 molecules. (g) The scatterplot of the photon count versus the spectral centroids. (h) and (i) respectively show the statistics of the emission photon count versus the number of emission events and centroid wavelengths versus the number of emission events. (j) The averaged spectrum of AF647 of all emission events in (g).

Using the simultaneously captured spectral images, we characterized the spectroscopic signatures of the individual AF647 molecules based on the spectral centroid method [5]. The scatterplot of the photon count versus the spectral centroid is shown in Fig. 4.2(g). We extracted the spectral centroid values from 99211 molecules in one 3D sSMLM dataset. We rejected emissions with a detected intensity below 500 photons. Figures. 4.2(h) and 4.2(i) respectively show the statistics of the emission photon count versus the number of emission events and centroid wavelengths versus the number of emission events. We found that the average photon count was 1250 in the spectral images and 550 in the spatial images. As shown in Fig. 4.2(i), we observed a narrow wavelength centroid distribution, which corresponds to a spectral precision of 4.21 nm. Figure 4.2(j) shows the averaged spectrum of AF647 for all the detected emission events in Fig. 4.2(g).
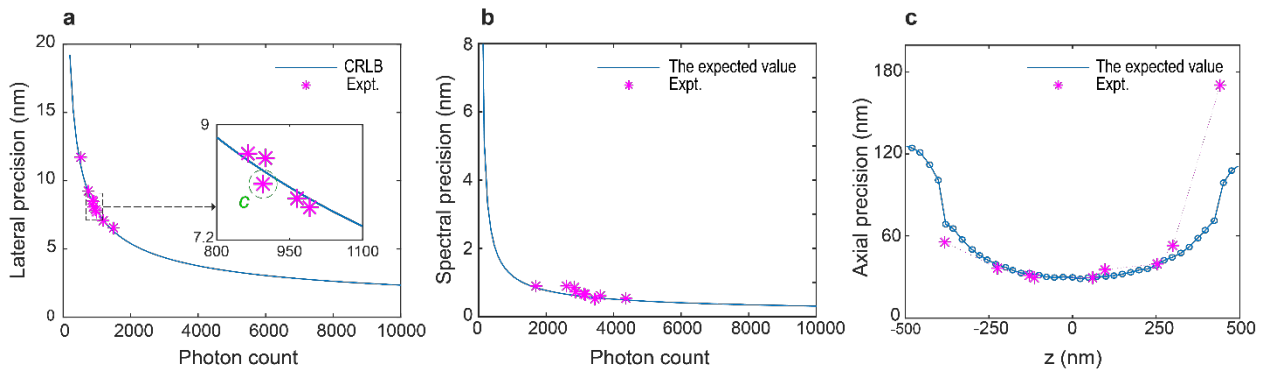
Figure 4.3 (a) The lateral localization precision and (b) the spectral precision as a function of photon count. The blue lines in (a-c) represent the theoretically expected values, while the magenta symbols represent the experimentally obtained values. We compared precisions at a single level

of 500 photons to 1500 photons in spatial image corresponding to the actual signal level in our sSMLM system. Given a splitting ratio between zeroth order and first order of a grating, approximately 1 to 3, the corresponding signal level in spectral image was 1500 photons to 4500 photons. (c) The axial localization precision as a function of the z-position at the signal level of 900 photons corresponding to the green marker, *c* in the inset in (a). The background level, readout noise, and the SD for theoretical estimation were 1 photon/pixel, 1e-/pixel, and 8 nm/pixel respectively in both analytical solution and numerical simulation.
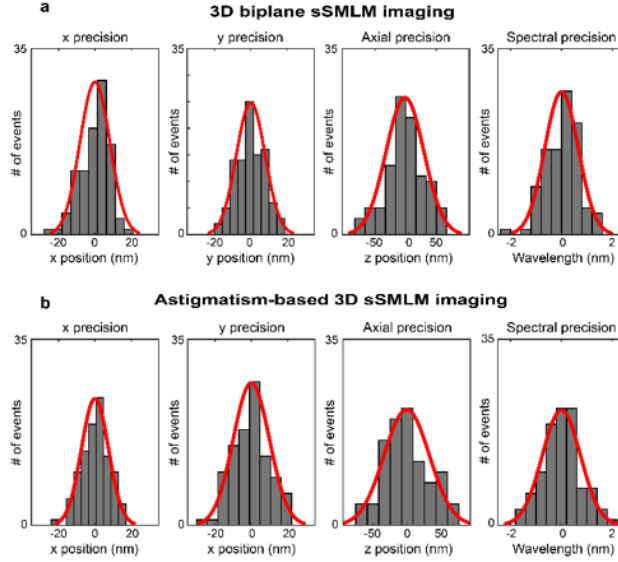
Figure 4.4 Spatial localization precisions and spectral precision for (a) biplane- and (b) astigmatism- based 3D sSMLM imaging. We estimated the precisions using a standard deviation of 100 recorded image frames of a single fluorescent nanosphere. The red lines represent the fitted Gaussian curve of histograms. Its standard deviation indicates precision value.
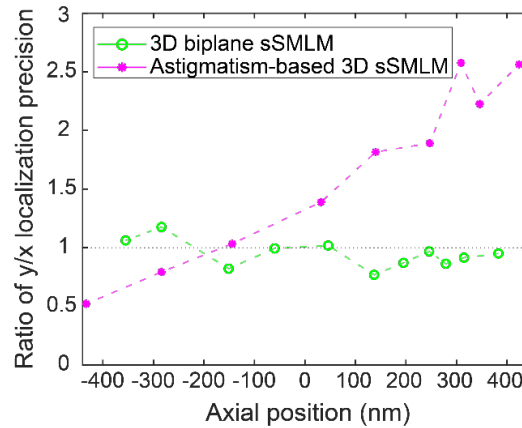
Figure 4.5 Lateral precision isotropy variations as a function of axial positions in biplane- and astigmatism-based methods.

4.3.2 Multi-color 3D super-resolution imaging

We further demonstrated simultaneous dual-color 3D imaging of two far-red molecular dyes with highly overlapping emission spectra using 3D biplane sSMLM. Several far-red dyes, which have similar fluorescent emission spectra (with typically 2.5 to 4.5 nm variation in emission wavelength centroid) and can be excited by a single laser, have recently been reported for sSMLM [3, 46]. We selected two dyes (AF647 and CF660C) with similar emission spectra to label microtubule and mitochondria, respectively. Figure. 4.6(a) shows the normalized emission spectra of AF647 (red) and CF660C (green) with their respective centroids (686 nm for AF647 and 695 nm for CF660C) highlighted. Figure 4.6(b) shows the histogram of the spectral centroid of the multi-color 3D sSMLM image of Tubulin and TOM20, labeled with AF647 and CF660C, respectively. Most of the detected spectral centroids for microtubules (labeled with AF647) are around 686 nm, and most of the detected spectral centroids for mitochondria (labeled with CF660C) are around 695 nm. We separated them by defining different color channels in the spectral image: the first channel from 674 nm to 689 nm for AF647 (red) and the second channel from 692 nm to 707 nm for CF660C (green).
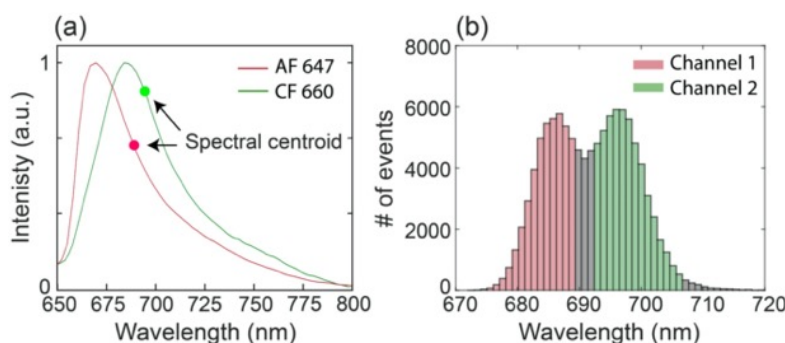
Figure 4.6 (a) The normalized emission spectra of AF647 (red) and CF660C (green) with their centroids (686 nm for AF647 and 695 nm for CF660C), respectively. (b) The histogram of the spectral centroid of multi-color 3D sSMLM image of Tubulin and TOM20, labeled with AF647 and CF660C, respectively. To

separate the two dyes, we defined two different color channels: (1) 674 to 689 nm for AF647 and (2) 692 nm to 707 nm for CF660C.
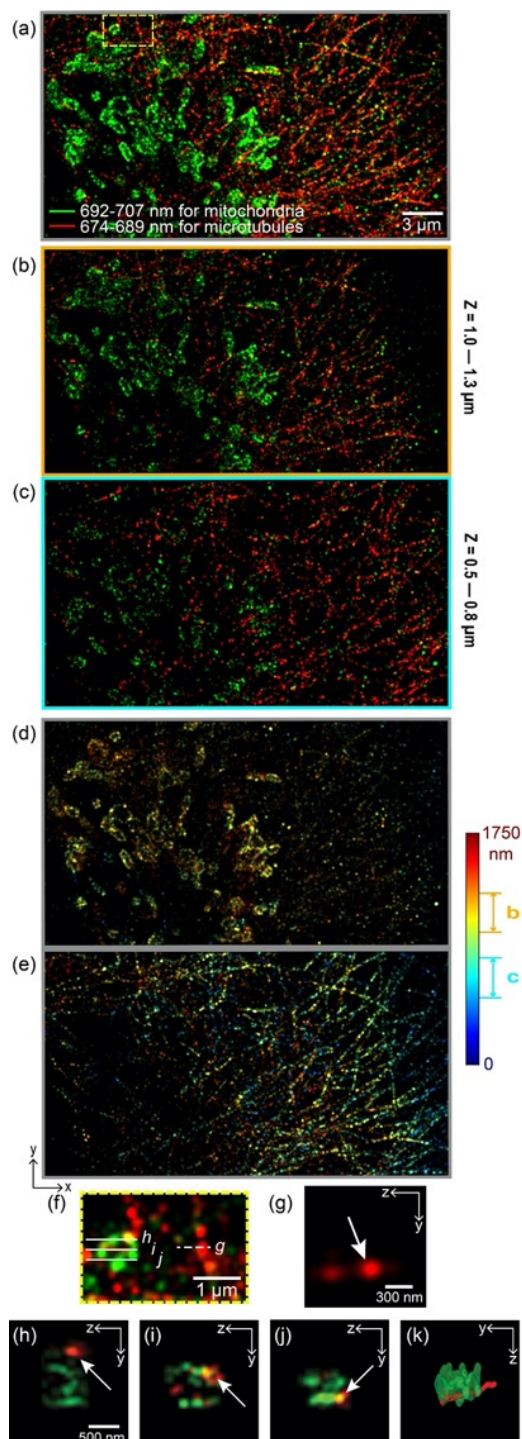
Figure 4.7 (a) An overall 2D projection view over a whole depth range of 1.75 µm. The red and green colors represent AF647 labeled microtubules and CF660C

labeled mitochondria, respectively. The projection images (a) for different axial ranges, from 1.0 μm to 1.3 μm (b) and from 0.5 μm to 0.8 μm (c) (color-coded along the spectral centroid in (a-c)). The separated 3D sSMLM images for different color channels, 692 to 707 nm for mitochondria (d) and 674-689 nm for microtubules (e) (color-coded along the axial-axis in (d-e)). (f) The magnified view of the region indicated by the yellow-dashed box in (a). (g) The cross-section image corresponding to the white-dashed lines in (f). (h-j) The cross-section images corresponding to the three white-solid lines in (f) (color-coded along the spectral centroid in (f-j)). (k) The volumetric rendering of the region covering (h-j). The rendering was visualized with the interpolation for a microtubule

Figure 4.7 shows multi-color 3D sSMLM images of Tubulin and TOM20 in COS-7 cells labeled with AF647 and CF660C, respectively. Similar to the data acquisition shown in Fig. 4.2, we combined three datasets translated along the z-axis at a step size of 450 nm. Figure 4.7(a) shows the 2D projection of the whole depth range of 1.75 μm. The red and green colors in Fig. 4.7(a) represent microtubules and mitochondria, respectively. We observed well-distinguished mitochondria and microtubules with negligible misidentification in their morphologies. In addition, we show the projection images with depth ranges from 1.0 μm to 1.3 μm and from 0.5 μm to 0.8 μm in Figs. 4.7(b) and 4.7(c), respectively. We clearly observed different morphologies for both distinct subcellular structures at the different axial ranges over all the images. Figures 4.7(d) and 4.7(e) are separated 3D sSMLM images of mitochondria and microtubules, respectively. Figure 4.7(f) is a magnified view of the region, highlighted by the yellow-dashed box in Fig. 4.7(a), showing spatially overlapping mitochondria and microtubule structures. The cross-sectional image of a microtubule along the y-z plane is shown in Fig. 4.7(g) from the position highlighted by the dashed-line in Fig. 4.7(f). From the axial line profiles of microtubules, we measured the axial precision to be ~ 50 nm. Figures 4.7(h)-(j) show the cross-sectional images of a mitochondrion and a microtubule and their spatial colocalization from positions highlighted by three white solid-lines (h, i, and j) in Fig. 4.7(f). We provide a 3D surface-rendering result in Fig. 4.7(k), which

shows the microtubule is close to the bottom of the mitochondria. These results demonstrate that 3D biplane sSMLM has the potential to provide insight into nanoscopic intracellular structures.

4.4 CONCLUSION AND DISCUSSION

By taking advantage of the axial position information encoded in the already-existing spatial and spectral imaging channels, we developed 3D biplane sSMLM. This method allows for simultaneous 3D spectroscopic imaging of multiple dyes without the need for sophisticated optics modification for PSF manipulation. Compared with reported 3D sSMLM work, we only added a pair of mirrors to introduce an optical delay in the spectral imaging channel and maximized the benefits of the two already-existing imaging channels. We showed a lateral localization precision of 20 nm at an average photon count of 550 with an axial localization precision of 50 nm at an average photon count of 1250 in the multi-color 3D imaging. We also confirmed the spectral precision of 4 nm in the single-color 3D imaging, and we confirmed a nearly uniform lateral localization precision within an imaging depth range of 800 nm using fluorescent nanospheres.

It is worth mentioning that we found a wavelength calibration challenge in the astigmatism-based 3D sSMLM imaging. When a cylindrical lens is inserted only into the zeroth order (spatial imaging) path, the beam paths for the spatial and spectral imaging experience different spherical aberrations, and this error may cause a spectral bias. Such spectral bias can be worse in sSMLM systems with lower SD and larger FOVs. Therefore, the astigmatism-based 3D method can be applicable to sSMLM only after a careful spherical aberration compensation. In contrast, the biplane-based 3D method does not introduce an aberration difference between the two imaging paths, inducing no additional wavelength calibration error.

The active area of the EMCCD camera is relatively limited in sSMLM, as we simultaneously acquired both the spatial and spectral images. This is one of the key limitations to restrict the FOV and the density of fluorophores. Furthermore, spectroscopic signatures in the spectral image are dispersed into several pixels along the spectral-axis (typically ~ 30 pixels under our experimental conditions) whereas the PSF along the y-axis can be covered by 7 pixels (> 99 %), given the sigma value of the PSF is approximately 1 pixel under our experimental conditions. Therefore, the density of fluorophores is rather limited and the overlapping issue between adjacent molecules in the spectral image is less tolerable in sSMLM.

The 3D biplane sSMLM offers several potential benefits to molecular biology investigations. First, it allows not only direct 3D observation of co-localized nanoscopic structures, but also comprehensive analyses of multi-molecular functions and interactions. Second, 3D biplane sSMLM can reliably identify multiple molecular dyes, which can have highly overlapped emission spectra. Third, the system's SD can be tuned and thus it can afford relatively high SD for more in-depth single-molecule spectroscopic analysis. In addition, it further helps to effectively suppress undesirable background, including the autofluorescence of impurities by separating them from target molecules based on their different spectroscopic signatures. Finally, 3D biplane sSMLM is compatible with and can be readily implemented in practically all existing Photoactivation localization microscopy (PALM) or stochastic optical reconstruction microscopy (STORM) systems. Therefore, biplane sSMLM provides an opportunity to investigate nanoscopic biological 3D structures at spectroscopic precision levels previously far out of reach.

4.4.1 FOV characterization of 3D biplane sSMLM system

The usable FOV is generally determined by the selection of the objective lens and the field of illumination. For sSMLM system, the FOV is further constrained by the diffraction angle (typically < 10 degrees) of the grating to avoid overlapping of the zeroth and the first order images. However, in the case of 3D biplane sSMLM method reported here, such constraint can be relaxed as the corresponding beam paths of the zeroth- and first-order images are manipulated independently. Assuming the illumination fully covers the entire FOV, the achievable FOV of our 3D biplane sSMLM using a 100x objective lens is $\sim 40 \times 40 \ \mu m^2$. In this study, due to the constraint of illumination beam shape, the FOV of the acquired images was $\sim 15 \times 30 \ \mu m^2$.

4.4.2 Spatial and spectral precision of 3D biplane sSMLM imaging

We first estimated the lateral localization precision in 3D biplane sSMLM using a maximum-likelihood estimation (MLE) method as reported by Mortensen and Rieger [16, 18]:

$$\Delta x^2 = \frac{F_{\text{EM}} \sigma^2 + a^2/12}{N} \left(1 + 4\tau + \sqrt{\frac{2\tau}{1 + 4\tau}}\right) \tag{4.2}$$

where $\tau = \frac{2\pi b (\sigma^2 + a^2/12)}{N a^2}$; F_{EM} is the noise factor when using the EMCCD camera (typically 2); σ is the standard deviation of a fitted Gaussian PSF in nm; a is the back-projected pixel size in nm; N is the number of photons detected for a given molecule; and b is the background photons. The expected lateral localization precision shown in Fig. 4.3(a) (blue solid line) was estimated based on Cramer–Rao lower bound (CRlb) using actual experimental conditions. In addition, we further quantified the lateral localization precision experimentally using far-red fluorescent nanosphere (200-nm diameter; F8807, Invitrogen) as the test subject. By controlling the illumination power and integration time, we constrained the recorded photon numbers within the zeroth order image

in the range of 500 to 1500, which corresponds to the photon number in our sSMLM measurements. We estimated the lateral localization precision using the standard deviation of 100 recorded image frames of the same far-red fluorescent nanosphere. As shown in Fig. 4.3(a), the experimentally obtained lateral localization precision agrees well with theoretical estimate.

Regarding the spectral precision, we have recently published the theoretical model in Ref. [19]. Using this model, the expected spectral localization precision is shown in Fig. 4.3(b) as blue solid line. In addition, we further quantified the spectral precision from the experimental data, which corresponds to the photon numbers in the range of 1500 to 4500 in the spectral image. As shown in Fig. 4.3(b), the experimental results agree-well with the theoretical estimation.

Finally, we estimated the axial precision with respect to the z position using a representative case marked as green circle shown in the inset in Fig. 4.3(a). Our established theoretical model for spectral precision [19] captures the localization precision in the spectral images. It can be further extended to the 3D biplane sSMLM imaging to estimate the axial precision based on a calibration measurement; we first obtained the sigma value of the PSF corresponding to different axial position from a calibration curve. Using this value, we generated spatial and spectral images in the numerical simulation reported in Ref. [19]. Then, we calculated the axial precision at different axial position. As shown in Fig. 4.3(c), trends of experimentally observed axial precision at the different z-position follows the theoretical values well.

4.4.3 Comparison of spatial and spectral precisions between biplane- and astigmatism- based 3D sSMLM imaging

To characterize the performance of 3D biplane sSMLM system, we experimentally quantified the spatial localization precisions and spectral precisions using fluorescent nanospheres and compared them with that of astigmatism-based 3D sSMLM. As shown in Fig. 4.4, both the biplane- and astigmatism-based approaches showed a comparable localization spatial precisions and spectral precisions. We found that the localization precisions along the x-axis are 8.25 nm and 7.42 nm, the localization precisions along the y-axis are 7.90 nm and 9.94 nm, and the axial localization precisions are 29.76 nm and 35.60 nm at ~ 900 photons for biplane- and astigmatism- based 3D sSMLM imaging methods, respectively. The spectral precisions are 0.66 nm and 0.75 nm at ~ 3000 photons for biplane- and astigmatism- based methods.

We further measured the depth variation of the ratio between the localization precisions along the x- and y-axis (defined as lateral precision isotropy) and compared the depth variations of the precision isotropy in both the biplane- and astigmatism-based methods. As shown in Fig. 4.5, the biplane-based method had a nearly uniform lateral precision isotropy within the entire 800-nm depth range. In contrast, the lateral precision isotropy varied significantly along the depth in the astigmatism-based method, due to non-uniform photon densities along the x and y axes induced by astigmatism. This is caused by changes in elongated PSFs as a function of the axial position, which affects the localization precisions along the x- and y-axes differently in the astigmatism-based method [50, 52].

4.4.4 Estimation of misidentification of two dyes between two color channels

We estimated misidentification of AF647 and CF660C between two color channels from statistical information obtained in the single-color 3D sSMLM imaging. We maintained similar experimental conditions, such as SD, photon counts of emission, and the background level, between single-color and multi-color 3D biplane imaging experiments. To do this, we first randomly selected the centroid wavelengths of 1000 molecules among 99211 molecules and counted the number of centroid wavelengths categorized into each channel as shown in Fig. 4.8(a). Then, we calculated the misidentification fraction of AF647 for the channel 2. We repeated this estimation 50 times and calculated the mean value and its standard deviation (s.d.). We confirmed that the misidentification of AF647 for the channel 2 was 6.44% with a s.d. of 0.65% as shown in Fig. 4.8(b). Considering similar spectral variations of AF647 and CF660C in their centroid wavelengths [7], we assumed that misidentification of CF660C for the channel is also relatively insignificant.
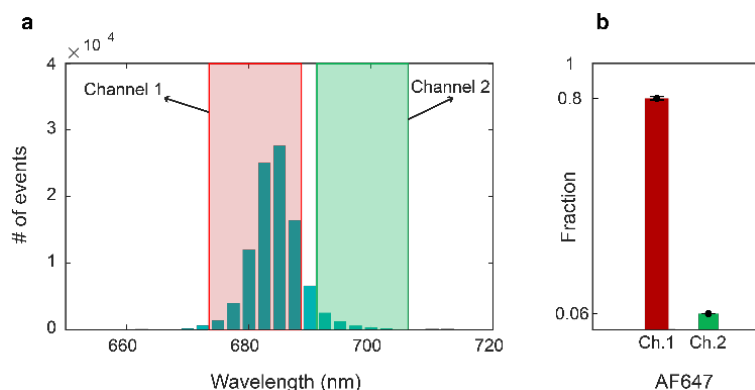
Figure 4.8 (a) Histogram of centroid wavelengths of same single AF647 molecules in single-color 3D sSMLM imaging (b) The misidentification fraction of AF647 for the channel 2.

4.4.5 Additional analyses of spatial and spectral precisions obtained in 3D biplane sSMLM imaging

The estimation for the lateral localization precision was performed in ThunderSTORM plugin in ImageJ software [25]. We first obtained the histogram of the estimated lateral localization precision of individual molecules for single/multi-color 3D sSMLM images and calculated the average precision value. We obtained the average lateral localization precision of 18 nm for a single-color 3D sSMLM image and 20 nm for a multi-color 3D sSMLM image, together with the average intensity of 550 photons in the spatial image, as shown in Figs. 4.9(a) and 4.9(b) respectively.
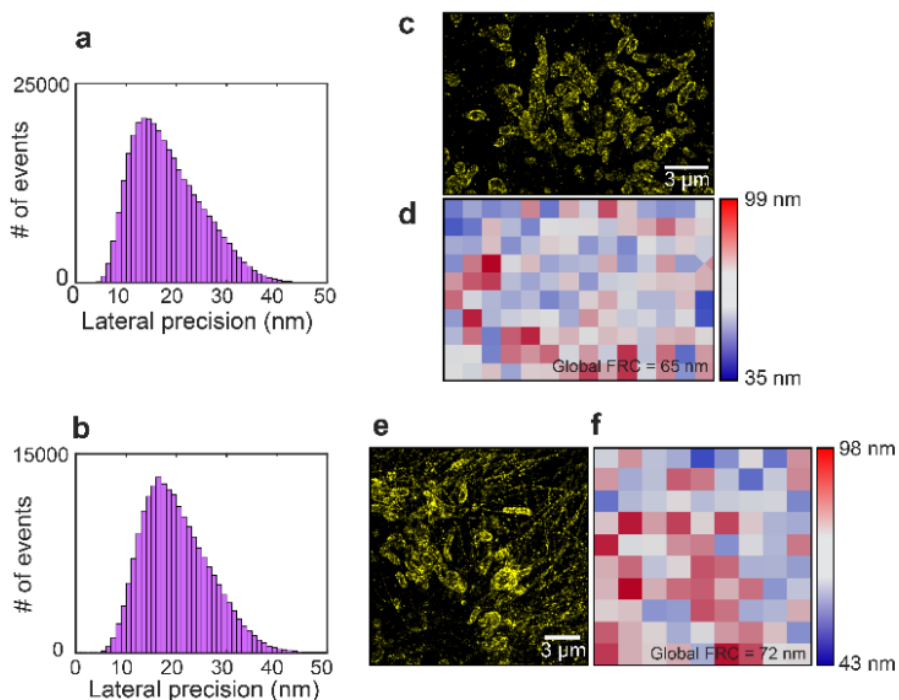
Figure 4.9 Histograms of the lateral localization precision for (a) a single-color 3D sSMLM image and (b) a multi-color 3D sSMLM image. (c) A super-resolved image of Fig. 4.2(a); (d) the corresponding local mapping of FRC values. (e) A super-resolved image of Fig. 4.7(a); (f) the corresponding local mapping of FRC values.

In addition, we quantified the lateral resolution using the Fourier Ring Correlation (FRC) method [65-67]. We visualized the local FRC-estimated resolution of super-resolved images using NanoJ-Squirrel plugin in ImageJ software [65]. Figure 4.9(c) shows a super-resolution image from Fig. 4.2(a). The corresponding local mapping of FRC values is plotted in Fig. 4.9(d). The global FRC value was 65 nm and the minimum FRC value was 35 nm. Additionally, the super-resolution image in Fig. 4.7(a) is shown as Figs. 4.9(e). Figure 4.9(f) shows the corresponding local mapping of FRC values. The global FRC value was 72 nm and the minimum FRC value was 43 nm. It should be noted that the final image resolution could be further affected by several other factors, such as biological drift, stage drift, the density of fluorophores, and the photo-switching property of its blinking, as compared to the localization precision [67].

Next, spectral precision was quantified by precision in fitting the spectral centroids, which is determined as the standard deviation of the fitted Gaussian function. This value provides an insight to understand noise contribution to the spectral precision as well as a heterogeneity of spectroscopic signature of single molecules. We obtained a spectral precision of 4.21 nm for single-color 3D sSMLM imaging (corresponding to Fig. 4.2(i)), as shown Fig. 4.10(a). This value agrees with reported values in our previous work [7].

In addition, we measured the axial precision, which can be empirically estimated by the localization distribution along the axial-axis from an isolated cluster from our multi-color 3D sSMLM images. We estimated the axial precision from the FWHM of the distribution by $\Delta z = FWHM/2.35$, assuming the distribution follows a Gaussian distribution [61] as shown in Fig. 4.10(b). From the axial line profiles of microtubules near the region highlighted by the white-dashed line (Fig. 4.7(f)), we obtained the axial precision to be ~ 50 nm.
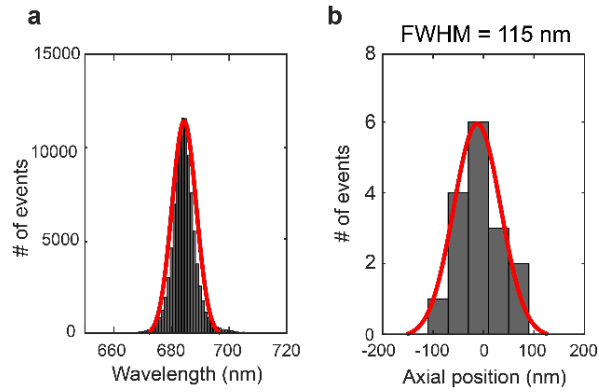
Figure 4.10 (a) Histogram of the spectral centroid wavelength distribution extracted from a single-color 3D sSMLM image of Fig 4.2(i) (b) Histogram of the localization distribution in the axial-axis near the region highlighted by the white-dashed line (Fig. 4.7(f)) from a multi-color 3D sSMLM image.

4.4.6 Wavelength calibration challenge in the astigmatism-based 3D sSMLM system

The astigmatism-based 3D sSMLM system inherently suffers from a wavelength calibration challenge because the spatial and spectral imaging channels experienced different spherical aberrations, which is caused by inserting a cylindrical lens only into the spatial imaging (zeroth order) channel. This error may cause a significant spectral bias. To illustrate the spectral bias, we tested it using fluorescent nanospheres. We acquired 100 frames, which contained emission events of nanospheres, captured without and with a cylindrical lens. Figure 4.11(a) shows the overlapped average image of 100 frames with the localization. The green and red colors in the spatial image (the orange dashed-box) represent the PSFs captured without and with the cylindrical lens, respectively, while the yellow color in the spectral image (the blue dashed-box) indicates their overlapped spectroscopic signatures. As a result, we observed different distances between the PSFs in the two situations. These differences in the spatial image introduced a wavelength calibration error up to 5 pixels (corresponding to 40 nm spectral bias) at the 8-nm/pixel SD, as illustrated in Fig. 4.11(b). Such spectral bias can be worse in sSMLM systems with lower SD and larger FOVs.

Therefore, the astigmatism-based 3D method should not be directly applicable to sSMLM without careful spherical aberration compensation.
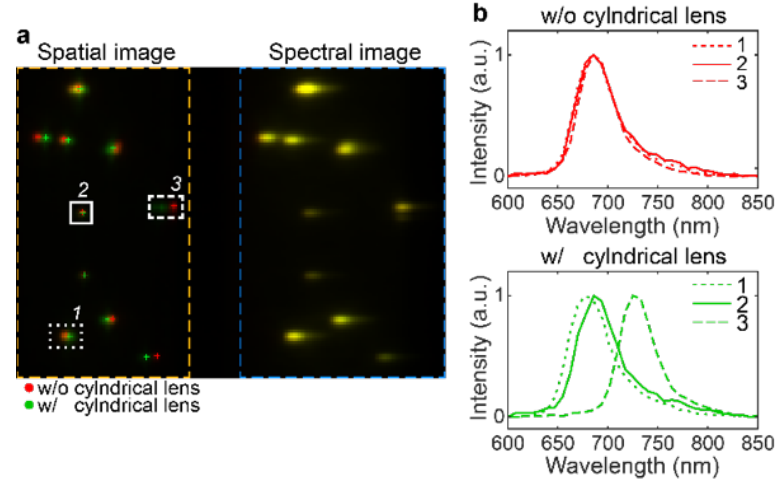
Figure 4.11 Spectral bias caused by astigmatism. (a) The overlapped average image of 100 frames, which contain emission events of nanospheres in the spatial image (the orange dashed-box) and their spectroscopic signatures in the spectral image (the blue dashed-box), captured without and with a cylindrical lens. The green and red colors represent the PSFs in spatial images captured without and with the cylindrical lens, respectively, while the yellow color indicates their overlapped spectroscopic signatures. Their localized positions were marked with a plus symbol (+). The emission spectra corresponding to the PSFs in the white boxes captured without and with a cylindrical lens were visualized on the top and bottom in (b), respectively.

Chapter 5

Symmetrically dispersed sSMLM for improving spatial resolution and spectral precision

The recent development of sSMLM greatly extended the boundary of super-resolution imaging by providing additional spectral analysis besides nanoscopic spatial information of fluorescent molecules. However, existing sSMLM fundamentally suffers from a reduced photon budget because of dividing photons from individual stochastic emissions into spatial and spectral channels. Therefore, both spatial localization and spectral analysis only use a portion of the total photons, leading to reduced precisions in both channels. To improve the spatial and spectral precisions, we present symmetrically dispersed sSMLM (SDsSMLM) by fully utilizing all photons of individual molecules in both spatial and spectral channels. Comparing with existing sSMLM using a 1:3 splitting ratio between spatial and spectral channels, SDsSMLM improves the spatial and spectral precisions by 42% and 10%, respectively, under the same photon budget. We also demonstrate multi-color imaging in fixed cells and three-dimensional single-particle tracking using SDsSMLM.

The proposed SDsSMLM method not only significantly improves spatial imaging resolution and spectral precision over existing sSMLM techniques, but also it can be accessible to a wider range of users due to its simplicity. Accordingly, SDsSMLM enables more precise spectroscopic single-molecule analysis in broader cell biology and material science applications. This chapter is adapted from a previously published article in *Light Science and Applications*.

5.1 INTRODUCTION

The ability of spectroscopic single-molecule localization microscopy (sSMLM) to capture spectroscopic signatures of individual molecules together with their spatial distribution allows observing subcellular structure and dynamics at nanoscale. As a result, sSMLM has shown great potential in understanding fundamental biomolecular processes in cell biology and material science [3-6, 11, 12, 15]. It also enables characterizing nanoparticle properties based on the emission spectrum at the single-particle level [68-72]. Similar to other localization-based super-resolution techniques, such as stochastic optical reconstruction microscopy (STORM) and point accumulation for imaging in nanoscale topography (PAINT), the localization precision of sSMLM is fundamentally limited by the number of collected photons per emitter [18]. However, sSMLM suffers from further photon budget constraint since the collected photons of each molecule need to be divided into two separate channels to capture the spatial and spectral information simultaneously. Thus, spatial localization precision of sSMLM also depends on the splitting ratio between the spatial and spectral channels and is typically limited to 15-30 nm in cell imaging [3-5, 7]. Although a dual-objective sSMLM design was previously demonstrated with improved spatial localization precision, it imposes a constraint on live-cell imaging and adds complexity to system alignment. Splitting photons into two channels in sSMLM forces an inherent trade-off between spatial and spectral localization precisions. Currently, a method to fully utilize the full photon budget to maximize both spatial and spectral localization precisions in sSMLM is still lacking.

To overcome this inherent trade-off, we develop the symmetrically dispersed sSMLM or SDsSMLM, which has two symmetrically dispersed spectral channels instead of one spatial and

one spectral channel. SDsSMLM fully utilizes all collected photons for both spatial localization and spectral analysis. We showed improvements in spatial and spectral localization precisions via numerical simulation and validated them through imaging fluorescent nanospheres and quantum dots (QDs). We further demonstrated multi-color imaging of subcellular structures and three-dimensional (3D) single-particle tracking (SPT) capabilities.

5.2 METHODS

5.2.1 Optical setup and image acquisition for SDsSMLM imaging

We performed all experiments using a home-built SDsSMLM system, which is based on an inverted microscope body (Eclipse Ti-U, Nikon) (Fig. 5.1(a)). We used a 640-nm laser to excite nanospheres, AF647, and CF680 and used a 532-nm laser to excite QDs. The laser beam was reflected by a dichroic filter (FF538-FDI01/FF649-DI01-25X36, Semrock) and focused onto the back aperture of an oil immersion objective lens (CFI Apochromat 100X, Nikon). We used a high oblique angle to illuminate the samples. The emitted fluorescence light was collected by the objective lens and focused by the tube lens onto the intermediate image plane after passing through a long pass filter (LPF) (BLP01-532R/647R-25, Semrock). We inserted a slit at the intermediate image plane to confine the field-of-view (FOV) and subsequently placed a transmission grating (46070, Edmund Optics) to disperse the emitted fluorescence into the -1st, 0th, and 1st orders. Then, the dispersed fluorescence emissions were captured by an EMCCD camera (iXon 897, Andor) with a back-projected pixel size of 160 nm after passing through the relay optics (f = 150 mm, AC508-150-B-ML, Thorlabs).

For SDsSMLM imaging of nanospheres, we acquired 200 frames at a power density of ~0.02 kW/m^2 with an exposure time of 20 ms. For the experimental validation of localization precision

using QDs, we acquired 200 frames while varying signal intensity (photon count) by adjusting EMCCD exposure time and controlling illumination power using a neutral density filter (NDC-50C-4M, Thorlabs). For multi-color SDsSMLM imaging of fixed COS7 cells, we acquired 20000 frames at ~10 kW/cm^2 with an exposure time of 20 ms. For SPT in 3D, we acquired 160 frames at ~0.02 kW/cm^2 with an exposure time of 5 ms.

5.2.2 Image reconstruction for SDsSMLM imaging

For image reconstruction, we first localized two spectral images of individual molecules with 2D Gaussian fitting using ThunderSTORM [25]. Then, using customized MATLAB codes, we classified them into two groups corresponding to the -1st and 1st orders and estimated the spatial locations of pairs of localizations by calculating their mean values. Next, we formed the virtual image using the estimated spatial locations.

For spectral calibration, we first captured a calibration image using a narrow slit and a calibration lamp. This calibration image includes multiple spectral lines of the calibration lamp in the two spectral images. By integrating the two spectral images along the y-axis, we obtained the emission peaks centered at 487.7, 546.5, and 611.6 nm. Then, we obtained a calibration curve by fitting the wavelengths of the emission peaks with their corresponding pixel distances using a linear polynomial function. Using the obtained calibration curve, we calibrated the emission spectra of individual molecule pairs. Lastly, we obtained the final emission spectra by combining the two symmetrical emission spectra. We used three emission peaks of 487.7, 546.5, and 611.6 nm of a calibration lamp for the first experiment demonstration using nanospheres while using two emission peaks at 620.23 and 603.24 nm of the Neon lamp (6032, Newport) in all other experiments.

To characterize spectroscopic signatures of individual molecules, we used the spectral centroid [19]. For all the experimental demonstrations, we estimated the spectral centroid in the same manner except multi-color imaging using nanospheres. Unfortunately, in this experiment, we rarely distinguished two different types of nanospheres based on spectral centroid values as the emission of one of the nanospheres (crimson) was partially rejected by the LPF. Thus, we fitted the emission spectrum using Gaussian function and used the emission peak as an approximation of spectral centroid.

For imaging nanospheres, QDs, and fixed cells, we used the spectral window of 650-750 nm, 565-665 nm, and 625-775 nm, respectively. Besides, we rejected blinking events below 500 photons during the spectral analysis in multi-color imaging of fixed cells. In addition, we used a spectral dispersion (SD) of 8.8 nm/pixel in nanosphere imaging and a SD of 10.5 nm in all other experiments.

5.2.3 Image reconstruction for 3D biplane SDsSMLM imaging

We reconstructed the 3D image in a similar manner as previously described in 3D biplane sSMLM, except that we used one symmetrically dispersed spectral image (-1st order) instead of the spatial image (0th order), together with another spectral image (1st order) for biplane imaging. We first captured a 3D calibration image using QDs. This image contains a few samples in both spectral images at different depths. The QDs were scanned from -1.5 μm to +1.5 μm along the z axis with a step size of 25 nm. Next, we obtained one dimensional (1D) PSF$_y$s by integrating the spectral images along the x-axis. Then, we measured the FWHM of two 1D PSF$_y$s and estimated their ratio. We used this ratio to calibrate the axial coordinate of each molecule.

5.2.4 Sample preparation for SDsSMLM imaging

We prepared nanosphere samples for single and multi-color SDsSMLM imaging according to the following steps. Cover glasses were rinsed with phosphate-buffered saline (PBS), coated with poly-l-lysine (PLL, P8920, Sigma-Aldrich) for 1 hour, and washed with PBS 3 times. Nanospheres (200 nm diameter; F8806 and F8807, Invitrogen) were diluted 10^4 times with a cross-linking buffer containing EDC (1 mg mL^{-1}, 1-ethyl-3-(3-dimethylaminopropyl) carbodiimide hydrochroride) and NHS (1 mg mL^{-1}, N-Hydroxysuccinimide) in 50 mM MES buffer (2-(N-morpholino) ethanesulfonic acid, pH = ~6, 28390, ThermoFisher). 200 μL of the cross-linking buffer with nanospheres was added to the PLL-coated cover glass. The cover glass was rinsed with PBS and dried under filtered air. Then, a drop of antifade mounting medium (P36965, Invitrogen) was added to a coverslip. The cover glass with samples was mounted on the coverslip by sandwiching the samples between them.

We prepared the QD sample according to the following steps. QDs (777951, Sigma-Aldrich) were diluted 10^4 times in water. 400 μL of the QD solution with a concentration of 0.5 μg mL^{-1} was deposited onto the cover glass using Laurell WS-650SZ-23NPPB spin-coater at 2000 rpm for 1 min. The cover glass with samples was mounted on the coverslip by sandwiching the samples between them.

For multi-color SDsSMLM imaging, COS7 cells (ATCC) were maintained in Dulbecco's Modified Eagle Medium (DMEM, Gibco/Life Technologies) supplemented with 2 mM L-glutamine (Gibco/Life Technologies), 10 % fetal bovine serum (Gibco/Life Technologies), and 1 % penicillin and streptomycin (100 U mL^{-1}, Gibco/Life Technologies) at 37°C with 5 % CO2. Cells

were plated on a cover glass with about 30 % confluency. After 48 hours, we rinsed cells with PBS, then fixed the cells with 3 % paraformaldehyde and 0.1 % glutaraldehyde in PBS for 10 min at room temperature. After washing with PBS twice, the cells were quenched with 0.1 % sodium borohydride in PBS for 7 min and rinsed twice with PBS. The fixed cells were permeabilized with a blocking buffer (3 % bovine serum albumin (BSA), 0.5 % Triton X-100 in PBS for 20 min), followed by incubation with the primary antibodies in the blocking buffer for 1 hour. For multi-color imaging of mitochondria and peroxisomes, the primary antibodies used in the study are mouse anti-TOM20 directly labeled with AF647 (2.5 µg mL^{-1}, sc-17764-AF647, Santa Cruz) and rabbit anti-PMP70 (1:500 dilution, PA1-650, ThermoFisher). The samples were washed three times with washing buffer (0.2 % BSA, 0.1 % Triton X-100 in PBS) for 5 min and incubated with the secondary antibodies labeled with CF680 (2.5 µg mL^{-1} donkey anti-rabbit IgG -CF680) for 40 min. For multi-color imaging of microtubules and mitochondria, the primary antibodies used in the study were sheep anti-tubulin (2.5 µg mL^{-1}, ATN02, Cytoskeleton) and mouse anti-TOM20 (2.5 µg mL^{-1}, sc-17764, Santa Cruz). After washing with washing buffer three times for 5 min, the samples were incubated with the secondary antibodies labeled with AF647 and CF680 (2.5 µg mL^{-1} donkey anti-sheep IgG-AF647, anti-mouse IgG-CF680) for 40 min. The dyes were conjugated to the IgG following a literature protocol (degree of label = ~1) [17]. The cells were then washed with PBS three times for 5 min and stored at 4°C. An imaging buffer (pH = ~8.0, 50 mM Tris, 10 mM NaCl, 0.5mg mL^{-1} glucose oxidase (G2133, Sigma-Aldrich), 2000 U mL^{-1} catalase (C30, Sigma-Aldrich), 10 % (w/v) D-glucose, and 100 mM cysteamine replaced PBS) was replacing PBS before image acquisition.

For 3D SPT, a QD solution of 0.5 μg mL^{-1} in water was mix with Glycerol (v/v = 1:9) and vortexed for 10 s. Then 50 μL of the final solution was added onto a cover glass immediately. The free-diffusing single QD was then observed and tracked.

5.2.5 Numerical simulation

To simulate two symmetrical spectral images in SDsSMLM, we first generated a spatial image. The spatial image was modeled as a 2D Gaussian function with a sigma value of 0.94 pixel, which represents the experimental conditions: back-projected pixel size of 160 nm and PSF FWHM of 350 nm. Then, we convolved the generated spatial image with the emission spectrum of the dye molecule being simulated to generate a spectral image (1st order). Next, we generated an identical spectral image (-1st order). We modeled various noise sources, such as the signal and background shot noise, and the readout noise. The shot and readout noises follow Poisson and Gaussian distributions, respectively. Finally, we generated noise-added spectral images at different signal and noise levels. We used the readout noise of 1e- and 3000 iterations in all simulations.

We estimated the spatial precision of SDsSMLM using the simulated spectral images. The spatial precision was calculated using the standard deviation of the distribution of the estimated (x_0, y_0) in the virtual spatial image (Fig. 5.1(e)). By averaging the two spatial precisions along the x and y axes, we calculated a final spatial precision. In addition, we estimated the spectral precision of SDsSMLM using the simulated spectral images. The spectral precision was calculated using the standard deviation from the distribution of the spectral centroid λ_{SC}.

To compare the performance of SDsSMLM with that of sSMLM, we also estimated the spatial precision in sSMLM. We first generated noise-added spatial images at different signal and noise levels. Then, we estimated the spatial precision using the standard deviation from the spatial

location distributions. Additionally, we estimated the spectral precision of sSMLM. This procedure was essentially the same as described for SDsSMLM, except that only one spectral image corresponding to the 1st order was used to obtain the emission spectrum.

Finally, we compared the spatial and spectral precisions of SDsSMLM with those obtained from sSMLM given varying splitting ratios between the 0th and 1st orders. For fair comparisons, we assumed that SDsSMLM and sSMLM share the same total number of photons. For SDsSMLM, the total photons were split equally between the -1st and 1st orders while sSMLM varied splitting ratios between the 0th and 1st orders.

5.3   RESULTS

5.3.1   SDsSMLM

The concept of SDsSMLM is illustrated in Fig. 5.1. SDsSMLM is based on a conventional SMLM system with a grating-based spectrometer. In the emission path, the fluorescence light is confined by a slit at the intermediate image plane and symmetrically dispersed into the -1st and 1st orders by a transmission grating with equal splitting ratio (Fig. 5.1(a)). Then, these dispersed fluorescence emissions are captured by an EMCCD camera to form two symmetrical spectral images after passing through the relay optics. In addition, Figure 5.1(b) shows the layout of the SDsSMLM spectrometer in Zemax based on the optical components and dimensions used in the experiment.
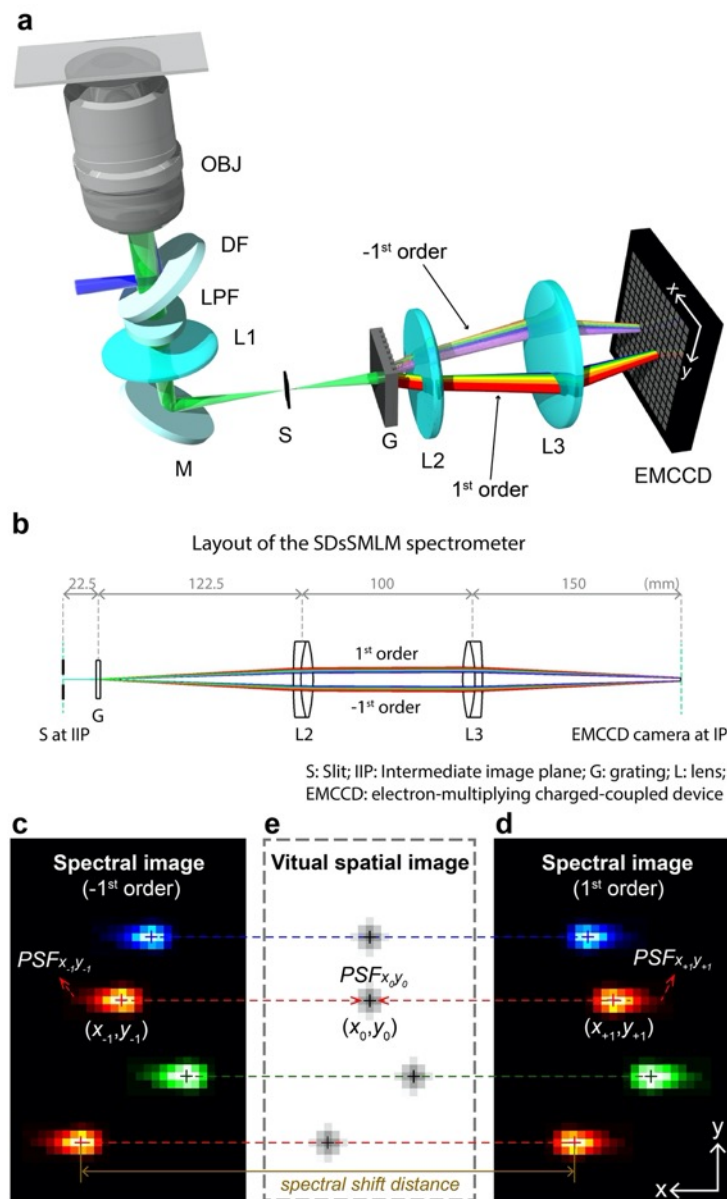
Figure 5.1 (a) Schematic of SDsSMLM; (b) Layout of the SDsSMLM spectrometer in Zemax based on the optical components and dimensions used in the experiment; (c) Illustrative image containing four molecules from the -1st order spectral channel; (d) Corresponding image of the same molecules from the 1st order spectral channel; **e** Calculated virtual spatial image from the two spectral images shown in the panels b and c. OBJ: Objective Lens; DF: Dichroic Filter; LPF: Long Pass Filter; L: Lens; M: Mirror; S: Slit; G: Grating; EMCCD: Electron-Multiplying Charge-Coupled Device.

While existing sSMLM simultaneously captures spatial (0th order) and spectral (1st order) images, SDsSMLM captures only two spectral images (-1st and 1st orders, Figs. 5.1(c) & 5.1(d)).

The two spectral images of a particular single molecule emission are mirror images of each other with respect to the true location of the molecule. Therefore, we can localize single molecules by identifying the middle points (black plus symbols in Fig. 5.1(e)) between the two symmetrically dispersed spectral images. This symmetry-middle point relationship holds true for all molecules regardless of their emission spectra and minute spectral variations even among the same species of molecules. Identifying all the middle points will generate a virtual spatial image (Fig 5.1(e)). This virtual spatial image utilizes all the detected photons in each EMCCD frame as compared with a portion of the photons in existing sSMLM. It also should be noted that the virtual spatial image is not affected by the spectral heterogeneity of individual molecules, which is cancelled out through the symmetry-middle point relationship.

In SMLM, we estimate the localization position of individual molecules in the spatial image with a limited certainty [73]. When the localization position is estimated repeatedly, the spatial localization precision (referred to as the spatial precision) is described as the standard deviation of the distribution of the estimated localization positions. Similarly, in SDsSMLM, we estimate the localization positions (x_{-1}, y_{-1}) and (x_{+1}, y_{+1}) from the -1st order and 1st order spectral images ($PSF_{x_{-1}y_{-1}}$ and $PSF_{x_{+1}y_{+1}}$ in Figs. 5.1(c) & 5.1(d)). Then, we determine the localization position (x_0, y_0) in the virtual spatial image ($PSF_{x_0y_0}$ in Fig. 5.1(e)) using (x_{-1}, y_{-1}) and (x_{+1}, y_{+1}), as shown in Figs. 5.1(c)-(e). Accordingly, the spatial precision in SDsSMLM is described by the standard deviation of the distribution of the estimated (x_0, y_0) in the virtual spatial image ($PSF_{x_0y_0}$).

In addition, from the two spectral images ($PSF_{x_{-1}y_{-1}}$ and $PSF_{x_{+1}y_{+1}}$), we generate new spectral images ($PSF_{\lambda y_{-1}}$ and $PSF_{\lambda y_{+1}}$) based on spectral calibration. Then, we integrate them along the y-axis and extract spectral centroids (λ_{SC}) to represent emission spectra of individual molecules. We

calculate λ_{SC} as $\lambda_{SC} = \sum_\lambda \lambda I(\lambda) / \sum_\lambda I(\lambda)$, where λ is the emission wavelength and $I(\lambda)$ is the spectral intensity at λ. Accordingly, the spectral localization precision (referred to as the spectral precision) is described as the standard deviation of the spectral centroid distribution.

Specifically, to generate the virtual image, we first localize the two spectral images ($PSF_{x_{-1}y_{-1}}$ and $PSF_{x_{+1}y_{+1}}$) of individual molecules along the x-axis using Gaussian fitting based on a maximum likelihood estimators (MLE) [16]. Then, we obtain the two localization positions x_{-1} and x_{+1}, which are symmetrically distributed with respect to the true location of the molecule. Therefore, we can determine the spatial location x_0 in the virtual image by calculating the mean value of x_{-1} and x_{+1}. In addition, we localize the two spectral images ($PSF_{x_{-1}y_{-1}}$ and $PSF_{x_{+1}y_{+1}}$) along the y-axis, which generates two localization positions y_{-1} and y_{+1}. These localization positions share the same location of the molecule along the y-axis. Hence, we can determine the spatial location y_0 in the virtual image by calculating the mean value of y_{-1} and y_{+1}.

We can also perform spectral analysis of individual molecules using all the detected photons. We define the distance between x_{-1} in Fig. 5.1(c) and x_{+1} in Fig. 5.1(d) as the spectral shift distance (SSD) [69]. For individual molecules with longer emission wavelengths (the red plus symbols in Figs. 5.1(c) & 5.1(d)), their SSD values are larger than the SSDs of molecules with shorter emission wavelengths (the green and blue plus symbols in Figs. 5.1(c) & 5.1(d)). Therefore, we can distinguish individual molecules based on their distinctive SSDs. To obtain emission spectra of individual molecules, we combine photons from the two spectral images ($PSF_{x_{-1}y_{-1}}$ and $PSF_{x_{+1}y_{+1}}$) with respect to their spatial locations (x_0, y_0) before spectral fitting, fully utilizing all the collected photons for spectral analysis.

5.3.2 Single- and multi-color SDsSMLM imaging of nanospheres

To test the feasibility of SDsSMLM, we first imaged fluorescent nanospheres (200-nm diameter, F8807, Invitrogen). As a proof of principle, we used a grating (#46070, Edmund Optics) that splits the emitted fluorescence photons into -1st, 0th, and 1st orders at 22.5%, 28.5%, and 24% transmission efficiency, respectively. The -1st order and 1st order images are the symmetrically dispersed spectral images and the 0th order image is the spatial image. Using the 0th order image, we compared the virtual spatial image estimated from the -1st and 1st order spectral images. Figures 5.2(a) & 5.2(b) show the two symmetrically dispersed spectral images and Figure 5.2(c) shows the simultaneously captured actual spatial images overlaid with the virtual spatial image. We observed that the virtual spatial locations (the green plus symbols in Fig. 5.2(c)) of nanospheres estimated from the spectral images agree well with the PSFs and further with the directly obtained spatial locations (the magenta circle symbols). The accuracy of the nanosphere in the highlighted region in Fig. 5.2(c) is 4.99 nm. (The average accuracy of five nanospheres is 20.59 nm with a standard deviation of 12.71 nm). The magnified views of the highlighted region in Fig. 5.2(c) are shown in Figs. 5.2(d)-(f). Note that each localization is rendered using a circle with 1-pixel diameter for better illustration in Figs. 5.2(d) & 5.2(f). In addition, we numerically corrected the location offset (17.68 ± 23.28 nm and 32 nm ± 9.99 nm (mean $\pm$ standard deviation) along the x and y axes respectively) between the virtual and actual spatial locations after image reconstruction.
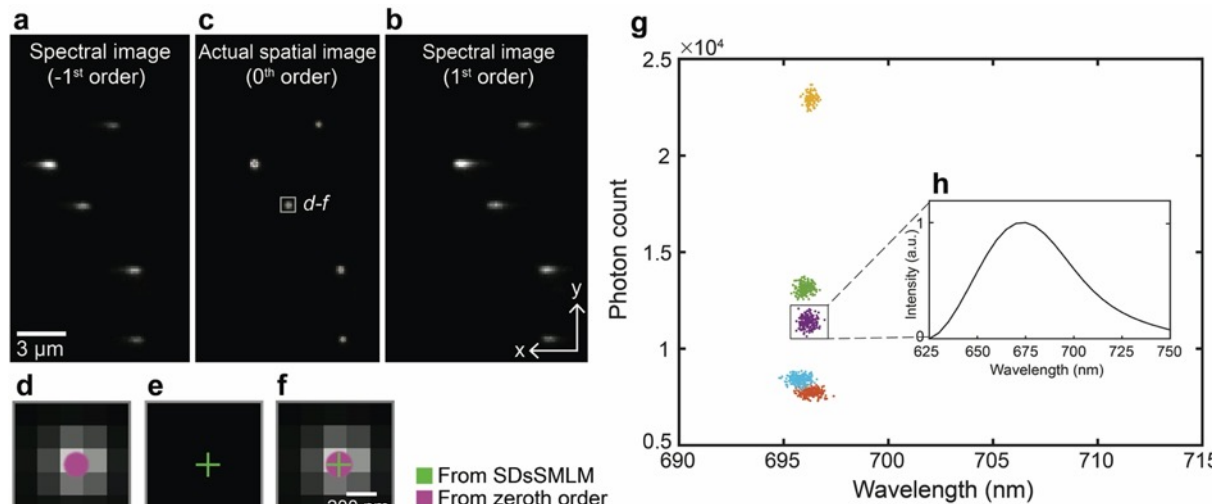
Figure 5.2 (a) to (b) The first frame of the simultaneously captured spectral images and actual spatial image of nanospheres, corresponding to the -1st, 1st, and 0th orders, respectively; (d), (e) Magnified views to compare virtual and actual spatial images of the region highlighted by the white-box in panel c; (f) The corresponding overlaid image; (g) The scatter plot of the photon count versus the spectral centroid; (h) The averaged spectrum of one nanosphere from 200 frames, corresponding to the purple cluster in panel g.

We characterized the spectroscopic signatures of the nanospheres using the spectral centroid method [46]. Figure 5.2(g) shows the scatter plot of photon count versus spectral centroid for five nanospheres. We observed a narrow spectral centroid distribution of five nanospheres centered at 696 nm with a spectral precision of 0.35 nm. Figure 5.2(h) shows the averaged spectrum of one of the nanospheres from 200 frames (purple cluster in Fig. 5.2(g)).

Besides functional imaging based on spectral analysis, sSMLM allows multi-color imaging with theoretically unlimited multiplexing capability. The multiplexing capability is predominantly determined by the spectral separation of selected dyes and the spectral precision under given experimental conditions [7]. We validated this capability in SDsSMLM using two types of nanospheres (200-nm diameter, F8806 and F8807, Invitrogen). Figures 5.3(a) & 5.3(b) show the first frame of the simultaneously recorded spectral images. While estimating the spatial locations of individual molecules (Fig. 5.3(c)), we successfully classified different types of nanospheres

based on their spectral centroid distribution (Fig. 5.3(d)). The red and blue colors in Fig. 5.3(c) correspond to spectral centroids of the crimson nanospheres (centered at 690.6 nm with the spectral precision of 0.48 nm) and of the far-red nanospheres (centered at 696.5 nm with the spectral precision of 0.53 nm), respectively in Fig. 5.3(d).
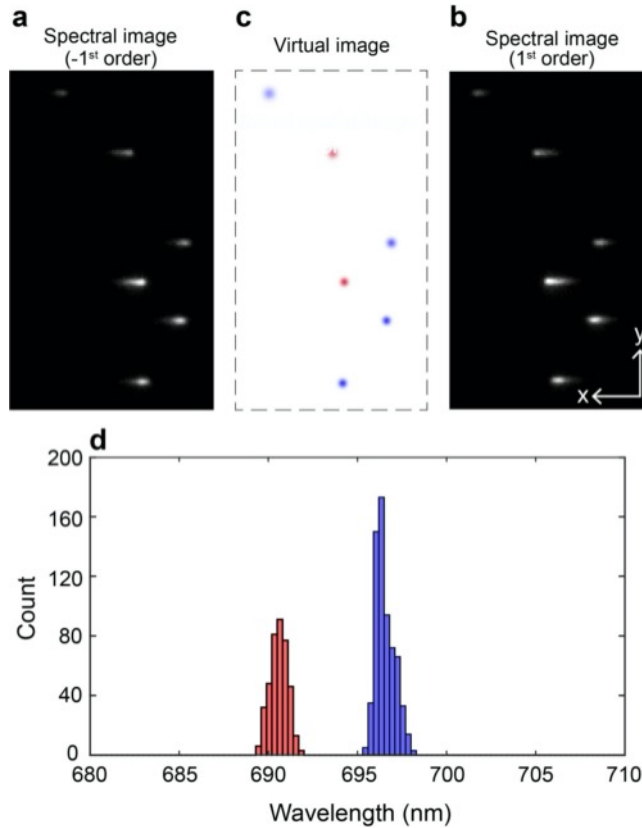
Figure 5.3 (a), (b) The first frame of the simultaneously captured spectral images of nanospheres from the -1st and 1st spectral channels, respectively; (c) Calculated virtual spatial image of the nanospheres; (d) The spectral centroid distribution of individual nanospheres. The red and blue color in panel c respectively correspond to the spectral centroids of 690.6 nm and 696.5 nm with the spectral precision of 0.48 nm and 0.53 nm.

5.3.3 Numerical simulation and experimental validation of localization precision in SDsSMLM

In SDsSMLM, collected photons are dispersed into more pixels in spectral image compared with in spatial image. Thus, spatial precision of PSF in spectral images (-1st and 1st orders) is more

sensitive to noise contribution than spatial precision of PSF in spatial image (0th order). Such spatial precision is not only affected by the number of collected photons and background, but also experimental parameters in the spectral channel, such as SD [19] and full width at half-maximum (FWHM) of the emission spectrum, which refers to emission bandwidth of single molecule. Through numerical simulation, we investigated the influence of SD and emission bandwidth of the emission spectrum on spatial precision as well as spectral precision under different experimental conditions. We further compared the spatial and spectral precisions in SDsSMLM and sSMLM both numerically and experimentally using QDs.
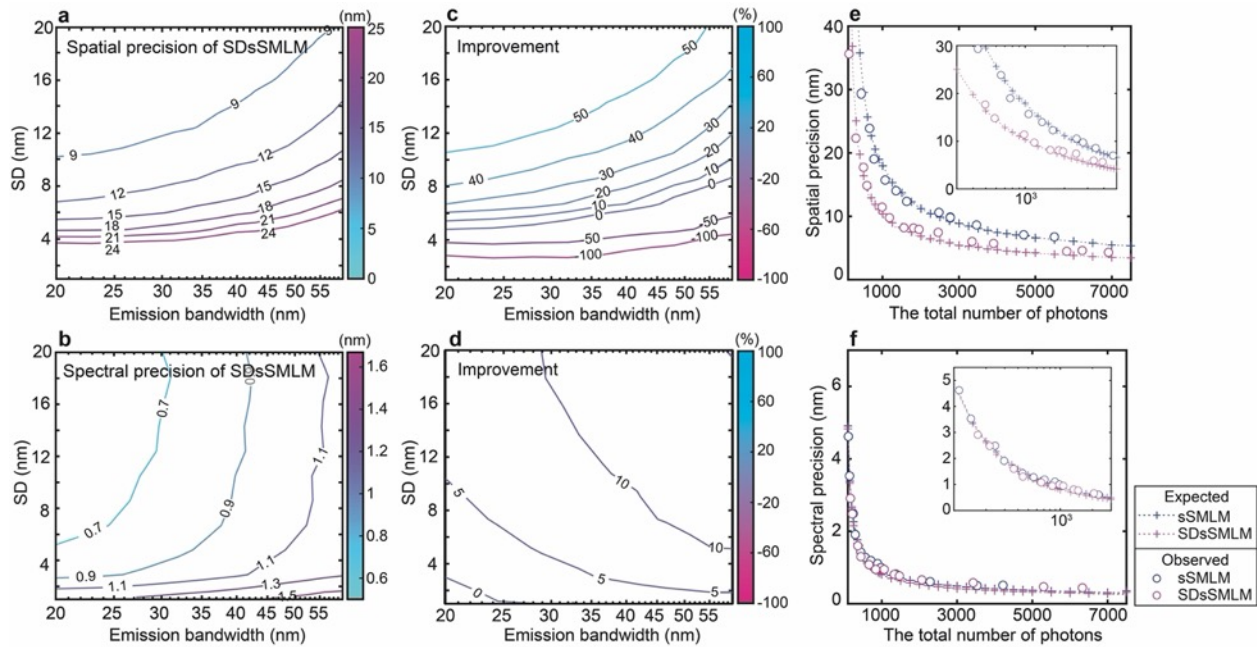
Figure 5.4 (a), (b) Contour map of spatial and spectral precisions under varying SD and emission bandwidth in SDsSMLM; (c), (d) Contour map of improvements in spatial and spectral precisions in SDsSMLM comparing with sSMLM; (e), (f) Spatial and spectral precisions of SDsSMLM and sSMLM as a function of the number of photons at 10.5-nm SD and 35-nm emission bandwidth. The magenta and blue colors represent SDsSMLM and sSMLM, respectively. The plus and circle symbols represent the theoretically and experimentally estimated precisions, respectively.

We compared achievable spatial and spectral precisions under different SD values and emission bandwidth values, where the total photon count is 1000. In sSMLM, we set the splitting

ratio between the spatial (0th order) and spectral (1st order) channels to be 1:3, following previously reported experimental conditions [7]. We approximated the emission spectrum shape as a Gaussian function. Figure 5.4(a) shows a 2D contour map of the estimated spatial precision of SDsSMLM. Overall, larger SD and narrower emission bandwidth favor high spatial precision. They also favor high spectral precision (Fig. 5.4(b) and Fig. 5.5(b)). These trends are fundamentally governed by contributions from various noises, such as the signal shot noise, the background shot noise, and the readout noise, and they agree well with analytical solutions, especially for spectral precision . In comparison, sSMLM shows a uniform spatial precision regardless of SD and emission bandwidth (Fig. 5.5(a)). This is because that information in the spectral image in sSMLM is only used for spectral analysis, which is independent of and does not contribute to spatial localization.
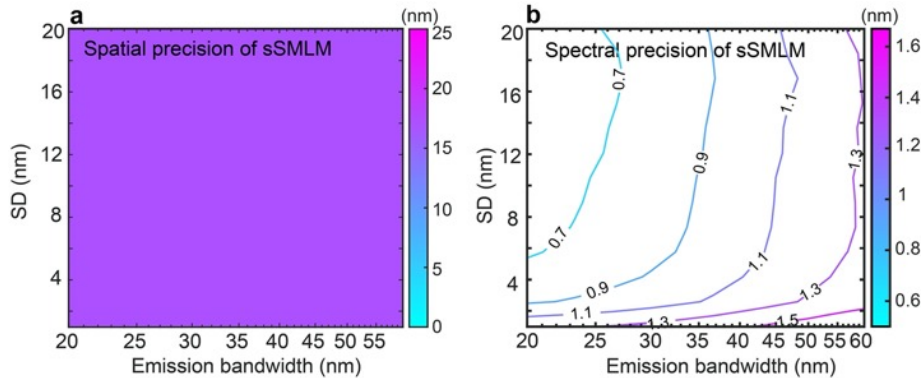
Figure 5.5 Influences of SD and emission bandwidth of the emission spectrum on the spatial and spectral precisions in sSMLM. (a), (b) Contour map of spatial and spectral precisions under varying SD and emission bandwidth.

Figures 5.4(c) & 5.4(d) show improvements in spatial and spectral precisions, respectively, with respect to SD and emission bandwidth in SDsSMLM as compared with sSMLM. For example, at 10.5-nm SD and 35-nm emission bandwidth, which represent the experimental conditions in imaging QDs, SDsSMLM shows approximately 42% (from 17.93 to 10.34 nm) and 10% (from 0.90 to 0.81 nm) higher spatial and spectral precisions, comparing with sSMLM. In

particular, SDsSMLM offers a relatively uniform improvement, approximately 10%, in the spectral precision overall. This improvement is proportional to the square root of the ratio of the number of photons allocated to the spectral channel between SDsSMLM and sSMLM (Fig. 5.4(d)). We further estimated the achievable spatial and spectral precisions when the number of photons increases. As shown in Figs. 5.4(e) & 5.4(f), the theoretical estimations are in good agreement with experimental results using QDs. In addition, we investigated the influence of splitting ratios on the spatial and spectral precisions (Fig. 5.6).
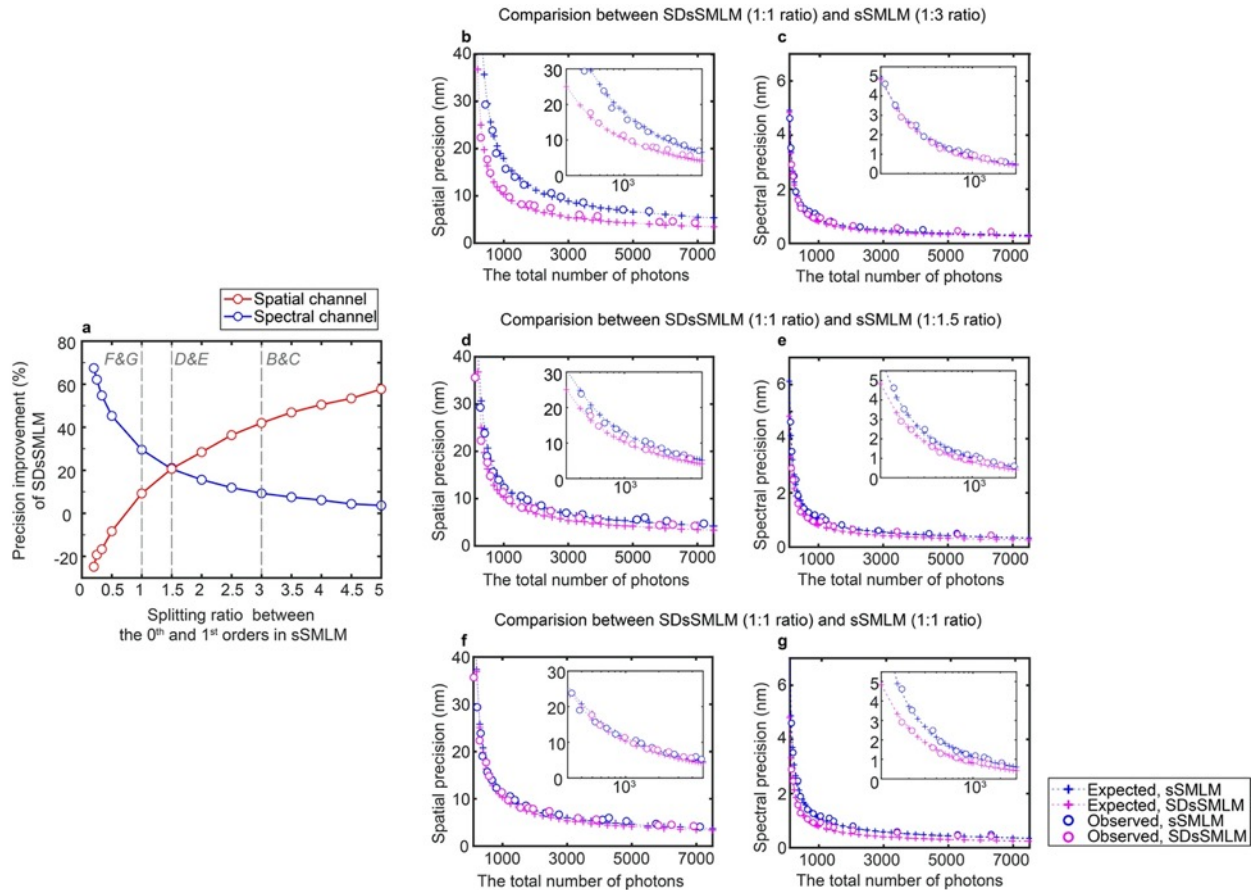
Figure 5.6 Additional comparisons of spatial and spectral precisions between SDsSMLM and sSMLM. (a) Expected precision improvement of SDsSMLM when splitting ratio between the 0th and 1st orders in sSMLM varies. The signal level is 1000 photons. At the splitting ratio of (b), (c) 1:3, (d), (e) 1:1.5, and (f), (g) 1:1 for sSMLM, the achievable spatial and spectral precisions as a function of the number of photons. SDsSMLM achieves 42% (from 17.93 nm to 10.34 nm) and 10% (from 0.90 nm to 0.81 nm) improvements in spatial and spectral precisions, respectively,

compared with sSMLM featuring a 1:3 ratio; (1) 19% spatial (from 12.73 nm to 10.34 nm) and 21% spectral (from 1.03 nm to 0.81 nm) precision improvements compared to sSMLM with a 1:1.5 ratio; (2) 10% spatial (from 11.42 nm to 10.34 nm) and 30% spectral (from 1.15 nm to 0.81 nm) precision improvements compared to sSMLM with a 1:1 ratio.

5.3.4   Multi-color SDsSMLM imaging of COS7 cells

We demonstrated multi-color imaging capability of SDsSMLM using fixed COS7 cells. We selected Alexa Fluor 647 (AF647) and CF680, which emit at wavelengths only ~30 nm apart (Fig. 5.7(a)), to label mitochondria and peroxisomes, respectively [7]. To classify them, we used different spectral bands based on the spectral centroid distribution: the first band from 682 nm to 694 nm for AF647 and the second band from 699 nm to 711 nm for CF680, as respectively highlighted by the yellow and cyan colors in Fig. 5.7(b). We visualized the colocalization of mitochondria (yellow) and peroxisomes (cyan) (Fig. 5.7(c)). We also imaged microtubules labeled with AF647 (magenta) and mitochondria labeled with CF680 (green) (Fig. 5.7(d)). By measuring the FWHM of a segment of imaged microtubule (dashed square in Fig. 5.7(d)), we estimate the spatial resolution of SDsSMLM to be 66 nm, as shown in Fig. 5.7(e). Also, we observed that the minimum resolvable distance between two tubulin filaments is within the range of 81-92 nm from multiple Gaussian fittings of the intensity profiles (Figs. 5.7(f) & 5.7(g)). Using a Fourier ring correlation method (FRC) method [67], we also evaluated the resolution of another reconstructed image (Fig. 5.7(c)) that visualizes mitochondria and peroxisomes. The FRC curve estimated a resolution of 111 nm (Fig. 5.8) at a threshold level of 1/7.
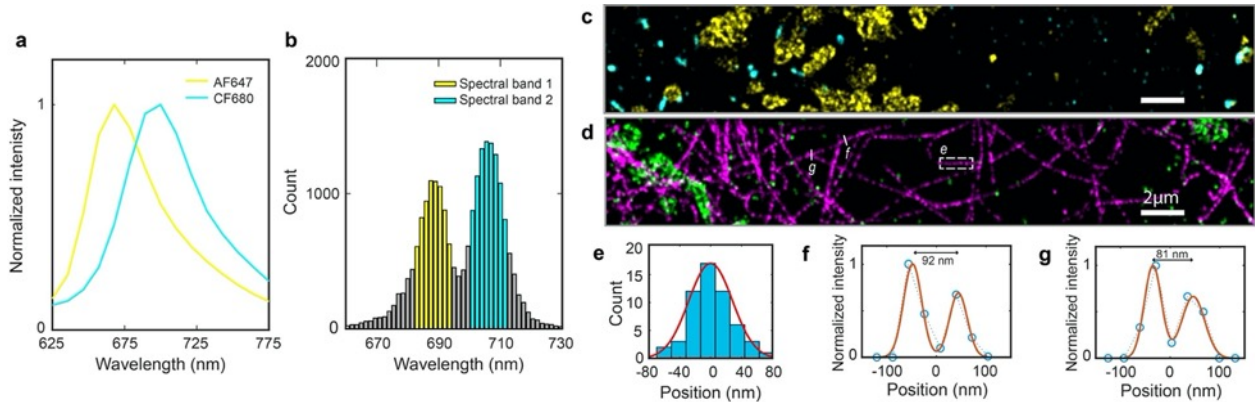
Figure 5.7 (a) Normalized emission spectra of AF647 (yellow) and CF680 (cyan); (b) Spectral centroid distributions of AF647 (yellow, 682 nm to 694 nm) and CF680 (cyan, 699 nm to 711 nm); (c) Reconstructed multi-color SDsSMLM image of mitochondria (yellow) and peroxisomes (cyan); (d) Reconstructed multi-color SDsSMLM image of microtubules labeled with AF647 (magenta) and mitochondria labeled with CF680 (green); (e) Histogram of the cross-section highlighted by the white-dashed box in panel d. (f), (g) Intensity profiles of two imaged tubulin filaments highlighted by the white-solid lines in panel d.

In addition, we quantified the utilization ratio, which is defined as the ratio between the number of localizations allocated into each spectral band to the total number of localizations, in the reconstructed image (Fig. 5.7(c)). We calculated the utilization ratio in SDsSMLM using both spectral images. We also calculated the utilization ratio by using only one spectral image (1st order channel), which mimics conventional sSMLM with a 1:1 splitting ratio between the spatial and spectral channels, for comparison. We obtained a 17.4% improvement in utilization ratio in SDsSMLM, on average for the two spectral channels, comparing with sSMLM (Fig. 5.9). This result demonstrates that SDsSMLM benefits from improved spectral precision by fully utilizing all collected photons for spectral analysis, which, subsequently, leads to improved spectral classification for multi-color imaging.
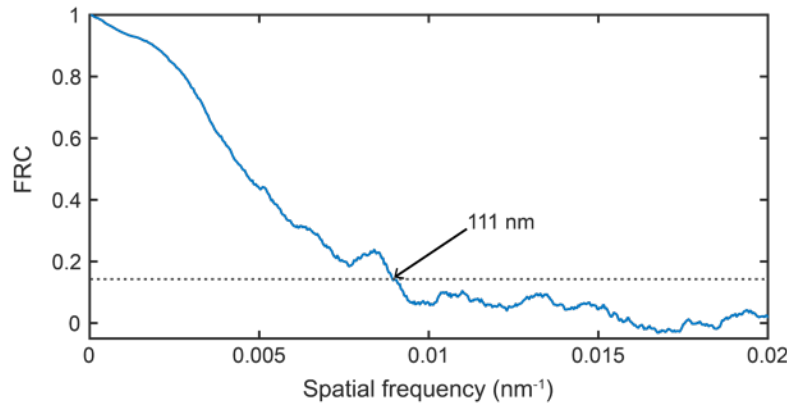
Figure 5.8 FRC curve of the reconstructed multi-color image shown in Fig. 5.7(c).
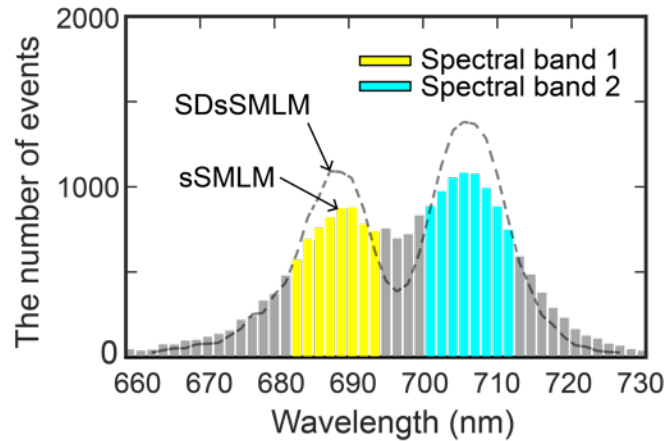
Figure 5.9 Analysis of utilization ratio for the reconstructed multi-color image shown in Fig. 5.7(c). The histogram represents the spectral centroid distribution estimated from only one spectral image corresponding to the 1st order. This case reasonably mimics conventional sSMLM with a 1:1 splitting ratio between the spatial and spectral channels. The dashed line shows the profile of the spectral centroid distribution estimated from two spectral images in the SDsSMLM case. The number of localizations allocated to each spectral band was increased from 6074 to 7119 for the first spectral channel and from 7759 to 9124 for the second spectral channel, which correspond to 17.2% and 17.6% improvements in the utilization ratio, respectively.

5.3.5   3D single particle tracking

We added 3D imaging capability to SDsSMLM through biplane imaging, similar to what we reported in sSMLM [46]. Since SDsSMLM already has two symmetrically dispersed spectral channels, we can efficiently implement biplane imaging by introducing an extra optical pathlength

in one channel. As shown in Fig. 5.10(a), we added a pair of mirrors in the 1st order spectral channel in front of the EMCCD camera to generate such optical pathlength difference. This optical pathlength difference introduced a 500-nm axial separation between the imaging planes of the two spectral channels. As a result, individual molecules are imaged with differently PSF sizes according to their axial locations. By measuring the ratio between the sizes of the PSFs, we can determine the axial coordinate of each molecule through an axial calibration curve.
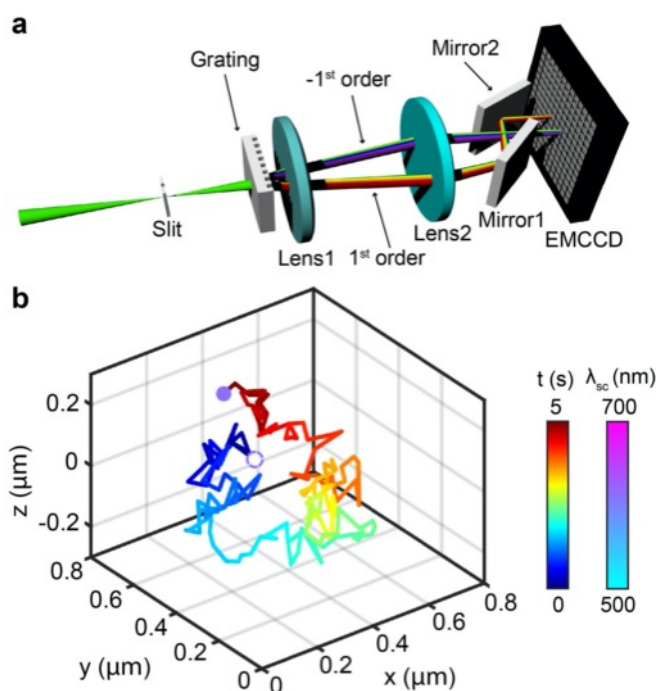
Figure 5.10 (a) Schematic of the 3D biplane SDsSMLM system; (b) Imaged 3D trajectory of a single QD color-coded with respect to acquisition time (solid line). The QDs at the first and last frames are highlighted by color-coded circles with respect to measured spectral centroids.

We demonstrated 3D biplane SDsSMLM by tracking individual QDs in a suspension. We tracked the movement of QDs for 5 s. We recorded 160 frames with an exposure time of 5 ms at a frame rate of 30 Hz. Figure 5.10(b) shows the 3D trajectory of one QD, color-coded along the time (represented by the line). The QD locations at the first and last frames are highlighted by the color-coded circles according to the measured spectral centroids. We observed that the spectral centroids

remained near 614 nm throughout the tracking period with a spectral precision of 1.5 nm (Fig. 5.11(a)). We approximated the diffusion coefficient from the 3D trajectory using $D = MSD/6t$, where MSD is the mean squared displacement and t is frame acquisition time [74]. The calculated diffusion coefficient is 0.0127 μm²/s. These results demonstrate the capability of 3D biplane SDsSMLM to precisely reconstruct the 3D spatial and spectral information of single molecules in SPT.
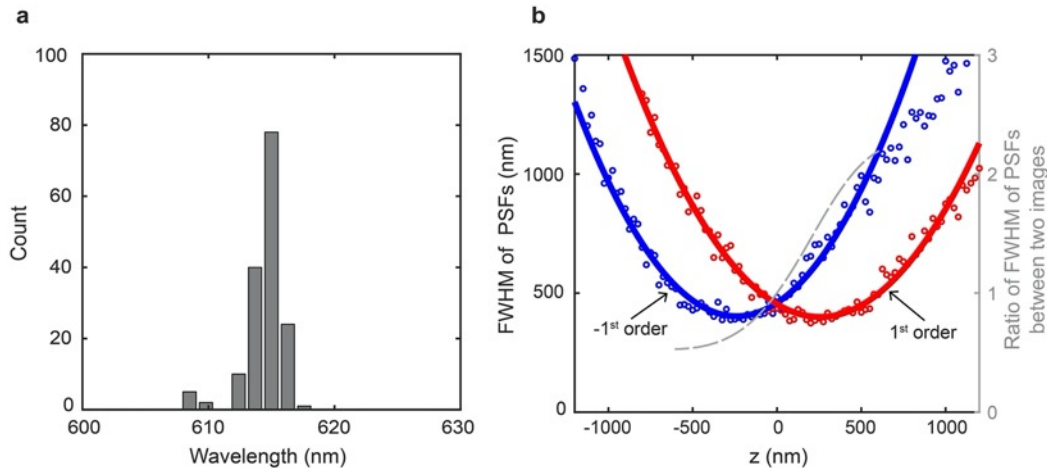
Figure 5.11 (a) Histogram of spectral centroids of the QD during tracking; (b) 3D calibration curve. The blue and red solid lines indicate the FWHM of PSFs in the 1st and -1st orders respectively. The gray color dash line represents the corresponding ratio.

5.4   CONCLUSION AND DISCUSSION

We demonstrated that SDsSMLM acquires both spatial and spectral information of single molecules from two symmetrically dispersed spectral images without capturing the spatial image. SDsSMLM maintains the highest achievable spectral precision per each emitter in a given experimental condition as it fully uses all collected photons for spectral analysis. In addition, it addresses an inherent trade-off between spatial and spectral precisions by sharing all collected photons in both spatial and spectral channels. We observed that SDsSMLM achieved 10.34-nm spatial and 0.81-nm spectral precisions with 1000 photons, which correspond to 42%,

approximately doubled photon enhancement, and 10 % improvements in the spatial and spectral precisions, respectively, comparing with sSMLM using a 1:3 ratio between the spatial and spectral channels.

We applied SDsSMLM to multi-color imaging and 3D SPT. It should be noted that these experimental demonstrations were based on a grating that splits the beam to the -1st and 1st orders with an efficiency of 22.5 % and 24 %, respectively. Thus, only approximately half of photons of the emitted fluorescence were used for image reconstruction in multi-color imaging. Consequently, the current implementation of SDsSMLM had a reduced image resolution. This can be improved by replacing this grating with a new phase grating, which can significantly suppress the 0th order and maximize the transmission efficiency only at the -1st and 1st orders, with a relatively high total transmission efficiency expected to be more than 85 % [75]. For comparison, a blazed grating previously reported in the conventional sSMLM system [7] has a ~ 18 % absolute transmission efficiency for the 0th order and ~ 50 % absolute transmission efficiency for the 1st order at the far-red channel, which corresponds to an overall efficiency of ~ 68 %. Considering the ~ 85 % efficiency of the phase grating, the localization precision will scale favorably due to increased efficiency of photon utilization. In this work, to compare both spatial and spectral precisions between SDsSMLM and the conventional sSMLM, we assumed an identical total number of photons in both systems and 100 % absolute transmission efficiency. Specifically, we compared two cases: (1) 25 % absolute transmission efficiency for the 0th order and 75 % absolute transmission efficiency for the 1st order in the standard sSMLM system and (2) 50% absolute transmission efficiency for both the 1st and -1st orders in SDsSMLM. This reasonably mimics a comparison study using the optimized phase grating and the normal blazed grating. In addition, the resolution can be further improved by using a larger SD and narrower emission bandwidth as

SDsSMLM favors a large SD and narrow emission bandwidth for higher spatial precision. However, an extremely low SD may compromise one of the benefits of SDsSMLM for functional studies that involve resolving minute spectroscopic features in single-molecule spectroscopy. This suggests that SDsSMLM requires a careful dye selection and system optimization to achieve desired spatial and spectral precisions.

The FOV in SMLM is mainly determined by the objective lens, the field of illumination, and the active area of the camera. For sSMLM equipped with a grating-based spectrometer, the FOV is further restricted by the diffraction angle of the 1st order of the grating, which determines the separation between the spatial and spectral images. In this work, our FOV was restricted to $\sim 30 \times 5$ μm^2 as we also captured the 0th order to compare the virtual and actual spatial images. This constraint can be relaxed in the future by a customized grating, which suppresses the 0th order. In this case, the FOV primarily depends on the separation between the -1st and 1st orders, which could increase the FOV by at least two-fold. Also, it can be further addressed in 3D biplane SDsSMLM by manipulating two diffraction orders separately.

In 3D biplane SDsSMLM, the PSFs of individual molecules in the spectral images are blurred when they are at out of focus planes. This does not allow for a detailed spectral analysis. However, the spectral centroid calculated still can be used to separate two dyes with slightly different fluorescence spectra [46]. In addition, we have small differences in the magnification and the SD between the two spectral images caused by their different pathlengths. However, the spectral centroid is not significantly affected by these issues and is sufficient for extracting spectroscopic signatures of individual molecules. We numerically corrected them before image reconstruction and spectral analysis. And we observed the spectral precision of 1.5 nm throughout tracking period

in a given experimental conditions: the signal level is ~6700 photons, and the background level is ~800 photons in total.

5.4.1 Achievable SD in sSMLM

SD is defined as the wavelength range per individual pixel (nm/pixel) [19]. It is mainly determined by the camera pixel size, the diffraction angle at the -1st or 1st orders, and the effective focal length of the relay optics. This can be approximated by [46],

$$\Delta\lambda = W_{\mathrm{p}} \times \frac{d\cos\theta}{f \times m} \tag{5.1}$$

where W_{p} [μm] is the camera pixel size; d [μm] is the groove spacing; θ [degree] is the diffraction angle; m [dimensionless] is the order of the maxima of the blazed grating (typically 1); and f [mm] is the effective focal length of the relay optics defined by Df_2/f_1. D [mm] is the distance from the grating position to the intermediate image plane; f_1 [mm] is the focal length of the collimating lens (L2 in Fig. 5.1(a)); f_2 [mm] is the focal length of the focusing lens (L3 in Fig. 5.1(a)).

As shown in Eq. 5.1, increasing the diffraction angle (θ) will reduce the achievable spectral dispersion $\Delta\lambda$. Our desired SD in sSMLM, however, is relatively low (typically 3-9 nm/pixel) [3, 5, 7], which corresponds to a relatively low diffraction angle (typically < 10 degrees). This can be sufficiently covered by the 2-inch imaging lens used in our experiment.

We quantified the achievable SD as a function of D and θ at given experimental conditions both theoretically and experimentally. As shown in Fig. 5.12(a), we can tune the SD by changing D [7]. The blue dotted line indicates the approximate distance (22.5 mm) used in our experiment to achieve a SD of 9 nm/pixel. In addition, at $D = 22.5$ mm, we can tune the SD from 7.5 nm/pixel to 9 nm/pixel by changing the diffraction angle (Fig. 5.12(b)), which is primarily determined by the groove density of a grating and the emission wavelength range.
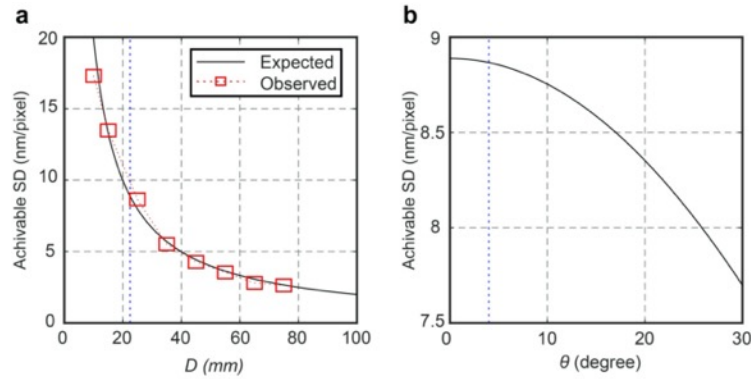
Figure 5.12 Achievable SD values as a function of (a) distance from the intermediate image plane to the grating and (b) diffraction angle of -1st or 1st orders. For estimation, we used experimental conditions: the focal length of 150 mm, the groove density of 80 grooves/mm, the camera pixel size of 16 μm.

While the SD can be determined by the grating position, spatial information at the intermediate image plane is preserved and formed at the EMCCD chip, which is a conjugate image plane of the intermediate image plane, regardless of the grating. In this work, the grating position was set to be 22.5 mm from the intermediate image plane, which corresponds to an SD of 9 nm/pixel.

5.4.2 Estimation of accuracy in SDsSMLM
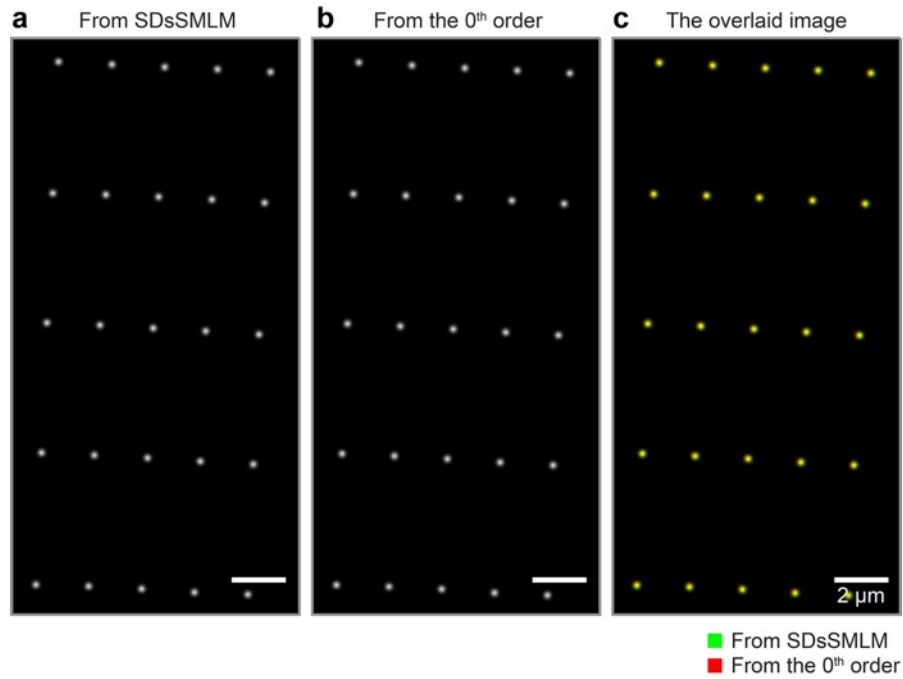
Figure 5.13 Comparison between (a) Reconstructed virtual spatial image and (b) actual 0th order spatial image of the nanohole array. (c) overlaid image of panels a and b.

In SDsSMLM, misalignment of the optical system or imperfect lens system can cause an uncertainty issue in a reconstructed image. This is a well-known issue caused by spherical aberration, field distortion, or asymmetricity of a lens pair with respect to the optical axis. Such imperfection especially influences localization accuracy, which describes the deviation of the mean of the obtained position coordinates from the true position of single emitters, rather than localization precision [73]. Accordingly, we quantified the accuracy of the SDsSMLM system using a custom-made nanohole array with known spacing. We imaged the nanohole array using a white-light lamp and a 532 nm laser line filter with an exposure time of 50 ms. Figures 5.13(a) and 5.13(b) show the reconstructed virtual spatial image and the actual 0th order spatial image of the nanohole array, respectively. The image contains 5 holes with spacings of 2 μm along the x-axis

and 5 µm along the y-axis, respectively; and the hole size is 200 nm. From the overlaid image (Fig. 5.13(c)), we observed that their spatial locations agree reasonably well with each other over the entire FOV. We considered the 0th order image as the ground truth and estimated the difference between Figs. 5.13(a) and 5.13(b). The accuracies over the entire FOV were 14.43±10.25 nm along the y-axis and 19.86±12.08 nm along the x-axis. Thus, overall the lens imperfection led to a localization error of <20 nm along both axes, which was smaller than the localization resolution in sSMLM cell imaging using a grating-based spectrometer, typically 40-80 nm.

Chapter 6

Photon-ACcumulation Enhanced Reconstruction

for achieving sub-2-nm spatial precision

The spatial resolution in SMLM is limited to around 20 nm due to the physical photon limit in individual stochastic single-molecule emissions, where all emissions are treated as independent events. Using sSMLM, we observed that single-molecule emissions from the same molecular species exhibit detectable spectral heterogeneity, which establishes the foundation for molecular identification. Taking advantage of such spectral heterogeneity, we developed photon-accumulation enhanced reconstruction (PACER) for sSMLM to break the physical photon limit by accumulating photons over repeated stochastic emissions from the same dye molecule through spectral identification. Using PACER, we experimentally demonstrate a 1.7-nm localization precision and resolved quantum dots that are 6.1 nm apart by utilizing their high spectral heterogeneity. We further validate the localization precision using two types of Alexa Fluor 647 labeled DNA origami nanostructures with known feature size as small as 6 nm.

The reported PACER method not only significantly improves imaging resolution over conventional SMLM techniques, but, more importantly, allows users to stay with existing SMLM fluorescence labels and imaging protocols. The broad accessibility and the molecular-scale resolution can potentially provide new insights into biological phenomena and enable significant research progress to be made in the life sciences.

6.1 INTRODUCTION

Pushing the limit of spatial resolution in optical nanoscopic imaging gained significant momentum since the award of the 2014 Nobel Prize in Chemistry to single molecule analysis and super-resolution imaging. Super-resolution imaging technologies, such as stimulated emission depletion (STED) microscopy and single-molecule localization microscopy (SMLM), surpassed the diffraction limit with demonstrated resolution of 10-20 nm [76-80]. In particular, SMLM technologies, including photoactivation localization microscopy (PALM), stochastic optical reconstruction microscopy (STORM), and point accumulation for imaging in nanoscale topography (PAINT), employ a stochastic switching or binding approach to regulate the density of fluorescent blinking within a recorded image frame. Accumulating the precise localization of individual single molecule fluorescence events from thousands of recorded image frames allows for the reconstruction of a super-resolution image. Despite being widely successful, the prerequisite stochastic process of single molecule florescence often produces a rather limited number of photons, which practically restricts the localization precision of SMLM techniques to around 20 nm.

To further improve the localization precision, DNA-PAINT and MINFLUX have been developed [81-83]. DNA-PAINT exploits transient binding between a docking strand and dye-conjugated imager strands to replace the stochastic switching process to eliminate the influence of photobleaching and allow the use of brighter non-blinking dyes. DNA-PAINT is capable of imaging discrete arrangements of fluorescent molecules with ~5 nm spacing on synthetic DNA nanostructures [81, 82] but more sophisticated labeling strategies are needed for imaging biological samples. On the other hand, MINFLUX relies on prior knowledge of the donut-shaped

illumination to triangulate the spatial location of individual emitters with greatly improved precision of ~2 nm, but at a reduced field of view (FOV) [83].
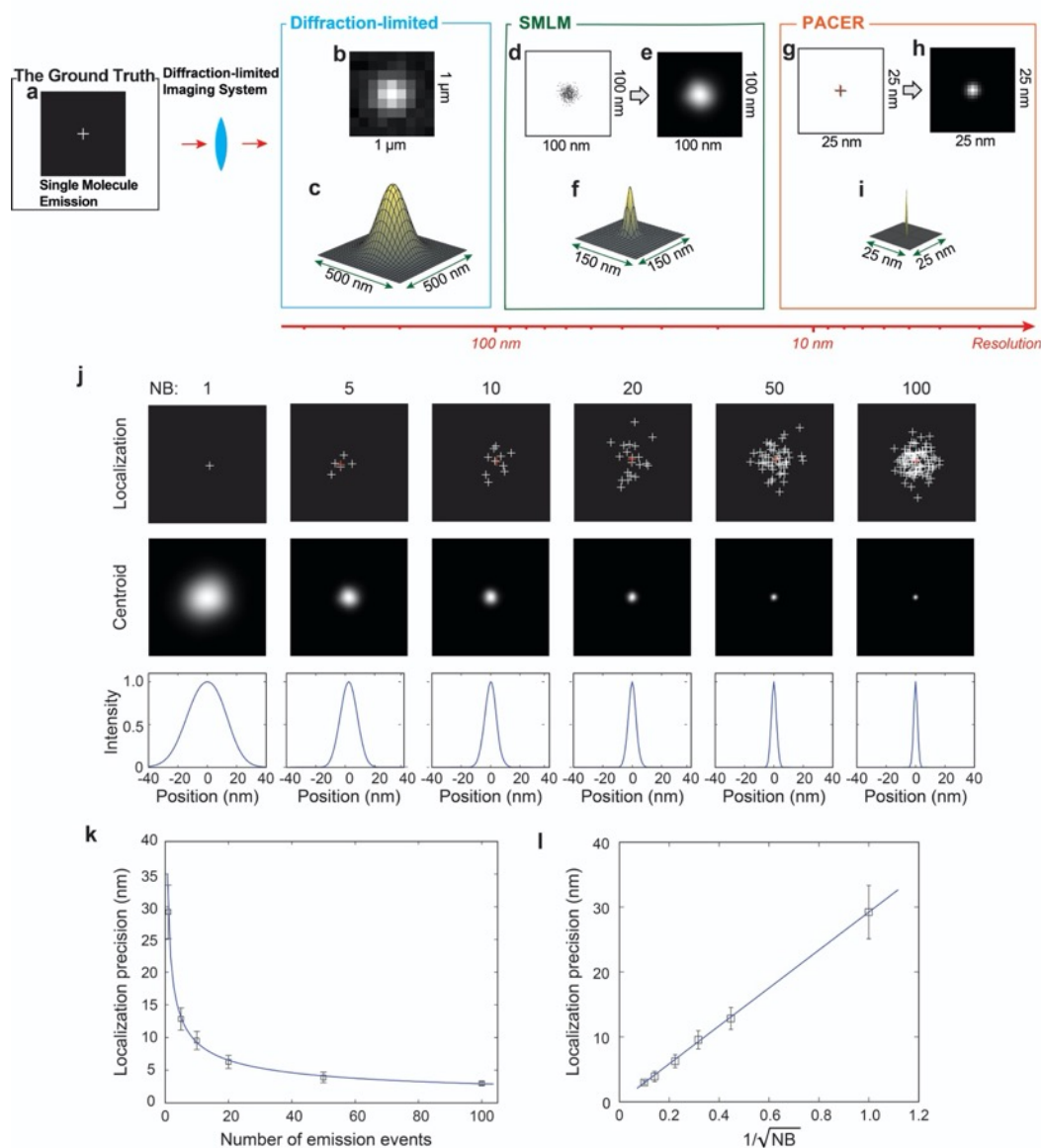
Figure 6.1 Schematic showing how image resolution is improved by molecular discrimination. (a) Due to the wave nature of light, when light comes from a point emitter focused by an optical imaging system, the interference can result in a blurred distribution of light or, called point spread function (PSF). (b-c) The size of the PSF sets up the fundamental resolution limit of an optical imaging system, namely Abbe diffraction limit. (d-f) In single-molecule localization microscopy

(SMLM), the probable location of a single fluorescent molecule can be estimated from the centroid of the fluorescence diffraction pattern produced on a camera. The localization precision is determined by the photon count collected in each captured frame. The scatter plot and rendered image of 100 blinking events indicate a localization precision of ~30 nm. (g-i) Through molecular discrimination, blinking events can be combined, resulting an improved localization precision of sub-3 nm. (j) Improved resolution using photon accumulation with respect to the number of blinking events (NB). White crosses denoted positions of all localizations in each test and red crosses denoted their centroids (upper panel). Reconstructed images only using centroids (middle panel). Localization precision is calculated along the x-axis and its intensity was then normalized for comparison, which are 28.57 nm, 13.24 nm, 9.02 nm, 6.40 nm, 3.89 nm, and 2.85 nm for NB=1, 5, 10, 20, 50, and 100, respectively (lower panel). (k) Simulated localization precision with respect to NB. Error bars are from 100 independent simulations. (l) The black line is the curve calculated by $\sigma_0/\sqrt{NB}$, where σ_0 is the localization precision at NB=1.

In fact, commonly used blinking dyes produce a large number of photons over the repeated occurrence of stochastic blinking events. However, due to the lack of molecular discrimination, the repeated stochastic blinking from the same molecule are all treated as independent events with limited localization precision around 20 nm. Thus, a method to identify the molecular origin of the stochastic blink events and subsequently accumulate the emitted photon from the same dye molecule can significantly improve the localization precision, without the need to reinvent the labeling and imaging protocols. To illustrate this concept, let's consider a single fluorescent molecule located at the center of the 1×1 µm² FOV as a representative example (Fig. 6.1(a)). The diffraction-limited imaging system forms a blurred image (Fig. 6.1(b)), which can be mathematically represented by a point spread function (PSF) with a typical diffraction-limited resolution of ~200 nm (Fig. 6.1(c)). The calculated centroid location of the recorded PSF is used to approximate the true location of the fluorescent molecule with a precision greatly exceeding the diffraction-limited resolution [23, 84, 85]. By programmatically switching the majority of the fluorescent molecules to the "off" state, SMLM detects a small subset of the fluorescent molecules that are stochastically restored to the "on" state. The centroids of the sparsely distributed PSFs

from a subset of molecules can be individually localized. These localized events are then accumulated over thousands of recorded image frames to build-up a super-resolution image. The localization precision in this process is inversely proportional to the square root of the photon number for individual blinking events [16]. Figure 6.1(d) shows a simulated SMLM image of 100 repeated stochastic blinking events from the same molecule, with 200 photons per stochastic blinking. Despite the fact that the photons originated from the same molecule, each stochastic blinking event is individually localized at photon-number limited precision of 30 nm (Figs. 6.1(e) and 6.1(f)). Since all the photons are originated from the same molecule, in principle, repeated blinking events can be aggregated to accumulate a much larger photon number to improve the localization precision as compared to localization precision being limited to each event (Figs. 6.1(g)-(i)). Figure 6.1(j) shows a simulation results on how accumulating photons from different numbers of repeated blinking events can improve the localization precision. As shown in Figs. 6.1(k) and 6.1(l), localization precision is inversely proportional to the square root of the number of blinking events (NB). After accumulating photons from 100 sequential blinking events, the localization precision is improved by 10-fold to ~ 3 nm, showing that the centroid location agrees well with the ground truth (Figs. 6.1(g)-(i)).

Thus, accumulating photons to improve localization precision can be accomplished if the true origin of the stochastic blinking can be specifically identified. This can be implemented via spatial clustering when the fluorescence molecules are sparsely distributed. As previously demonstrated, aggregating photons over prolonged detector exposure time can reach a localization precision of 1.5 nm in well-separated single molecule tracking [84]. However, imaging biological systems often requires much higher molecular labeling densities and thus, spatial locations alone become

insufficient for identifying the sources of emitted photons to specific individual molecules among a densely packed ensemble.

In addition to their spatial locations, the fluorescence spectra of emission events may provide additional dimensionality to specifically identify individual molecules for potential photon accumulation [5]. Simultaneously recording the spatial and spectral information of each stochastic fluorescent emission event was recently made possible using spectroscopic single-molecule localization microscope (sSMLM) developed by us and other groups [3-6]. In our previous study, we have demonstrated the use of sSMLM to identify fluorescent molecules of different species based on their distinct emission spectra [7]. Interestingly, single-molecule spectroscopy studies suggest individual fluorescent molecules of the same species also exhibits distinct dissimilarity in their emission spectra, this phenomenon is often referred to as the spectral heterogeneity (SH) [3, 7]. Thus, capturing the inherent SH of individual fluorescent molecules further enables for spectroscopic discrimination of individual molecules of the same species in sSMLM [8, 86].

In this work, we report photon-accumulation enhanced reconstruction (PACER), which accounts for photons in repeated emission events from the same molecules through spectroscopic discrimination by sSMLM. Using PACER, we demonstrated a 1.7-nm localization precision using quantum dots (QDs), which exhibit high SH. We further showed that even with fluorophores with

low SH (Alexa Fluor 647, AF647), PACER resolved 6-nm spatial features in DNA origami nanostructures.

6.2   METHODS

6.2.1   Optical setup

The optical setup contains an inverted optical microscope (Eclipse Ti-U, Nikon), equipped with 645-nm and 445-nm solid-state lasers with 500-mW maximum output, a high numerical aperture objective lens (100x, NA1.49, Nikon CFI apochromat TIRF) for TIRF illumination, and a home-built transmission spectrometer. The illumination power was controlled by a set of linear polarizers. The imaging filter set was consisted of a laser clean-up filter (FF01-642/10-25, Semrock), a dichroic mirror (FF649-DI01-25X36, Semrock), and a long-pass filter (BLP01-647R-25, Semrock) at the emission port to reject the reflected laser beam. The fluorescence image was then coupled into a transmission spectrometer featuring a blazed dispersive grating (150 grooves/mm). The image further divided into a non-dispersed zero-order spatial image and a spectrally dispersed first-order spectral image and can be simultaneously collected by a high-sensitivity electron multiplying charge-coupled device (EMCCD, ProEM, Princeton Instruments).

6.2.2   sSMLM imaging procedure

The samples were placed on the microscope stage and imaged under a TIRF objective with an additional magnification of 1.5X by a tube lens. We used a 445-nm laser to excite fluorescence from QDs and a 645-nm laser to excite fluorescence from Alexa Fluor 647 on DNA nanorulers and nanogrids. The illumination intensity was set to be 10 kWcm^{-2} and 3 kWcm^{-2} to create stochastic radiations from QDs and Alexa Fluor 647 for sSMLM imaging, respectively. The EMCCD camera acquired images from the monochromator with integrating time of 10 ms at a

frame rate of 85 Hz. Unless specifically noted, 5,000 frames were recorded for imaging reconstruction using PACER.

6.2.3 Sample preparations

The QD nanoparticles used in the experiment is core-shell CdSe/ZnS Lumidots™ (product #: 694614) with mean particle size of 5.2 nm and emission peak at 610 nm. QDs were immobilized on a coverslip (#1.5, VWR) by spin-coating of their suspension (~100 ng/mL) and covered with silicon oil to protect them from photo-oxidation.

The nanorulers was customized from Gattaquant DNA Nanotechnologies with mark-to-mark distances of 23 nm, 11 nm, and 6 nm, respectively. Each mark only contains one Alexa Fluor 647 molecule. All samples were delivered in solution and then immobilized on BSA-biotin-neutravidin surface in LabTek (VWR) chambers.

The LabTek chamber (VWR) was washed three times with 500 µL PBS and then incubated with 200 µl of BSA-biotin solution (1 mg/ml in PBS) for 5 min. After removing the BSA-biotin solution, the chamber was washed 3 times with 500 µl of PBS. Then the chamber was incubated with 200 µl of neutravidin solution (1 mg/ml in PBS) for 5 min and washed three times with 500 µl of 1x PBS supplemented with 10 mM magnesium chloride. 1 µl of the DNA origami solution were diluted with 200 µl of 10 mM magnesium chloride. The chamber was incubated with the diluted DNA origami solution for 5 min to achieve the desired surface density of DNA origami structures (~ 0.1 μm^{-2}) and then washed three times with 500 µl of PBS. The chamber was filled with the imaging buffer prior to imaging.

A standard imaging buffer was freshly made and added to the DNA nanoruler samples prior to imaging. It contained TN buffer (50 mM Tris and 10 mM NaCl), an oxygen scavenging system

(0.5 mg/ml glucose oxidase (Sigma-Aldrich)), 40 µg/ml catalase (Sigma-Aldrich) and 10 % (w/v)

glucose (Sigma-Aldrich), and 143 mM βME (Sigma-Aldrich).

6.3   RESULTS

6.3.1   Imaging Quantum dots with PACER
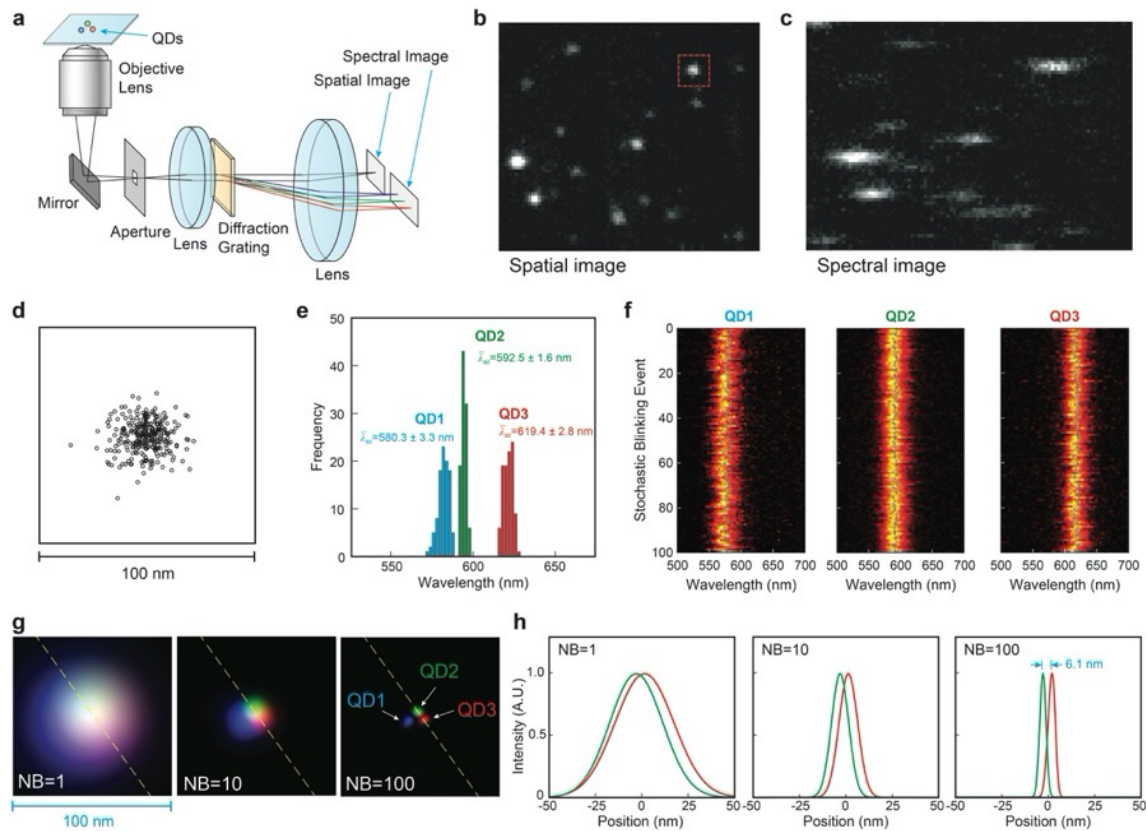
Figure 6.2 Experimental demonstration of PACER in achieving a 1.7-nm localization precision. (a) The schematic of sSMLM. (b) One frame of the spatial images and (c) one frame of the simultaneously acquired spectral images of the QD sample. (d) The scatter plot of localization events in the red dashed box in (b). (e) Histogram of the SC distribution. (f) Fluorescence spectra of three QDs after classifying by SCs using spectral intensity threshold of 300, 460, and 480 photons, respectively, and spectral windows of 575-585 nm, 585-600 nm, and 615-625 nm, respectively, as filtering criteria. The corresponding SC of each fluorescence spectrum is noted as an open circle in the plot. (g) Rendered sSMLM images after combining multiple emission events with NB of 1, 10, and 100, respectively. (h) Line profiles across two QDs in (g) with NB of 1, 10, 100.

We first experimentally demonstrate the feasibility of PACER in achieving sub-2-nm resolution using QDs. Figure 6.2(a) shows the schematic of the sSMLM system. It employs a dispersive optical component to simultaneously capture the full fluorescent emission spectrum along with the spatial location of every single-molecule emission event. We chose QDs for their high SH due to structural variation and crystalline defects [87]. The high SH enabled us to easily distinguish individual QDs using their distinct fluorescence spectra. Before imaging, we sparsely dispersed QDs (Lumidot, #694614, Sigma-Aldrich Co.) onto cover slides. Using sSMLM, the captured emission spectra are associated with the locations of individual blinking events. Figure 6.2(b) shows one frame of the spatial images and Figure 6.2(c) shows the simultaneously acquired spectral image of the QDs. Among all the recorded localization events, some "outliers" caught our attention. Specifically, the red dashed box highlights a region, within which we observed more frequent stochastic blinking events compared to the surroundings. The corresponding spectral image also appears to be much wider than the typical single QD emission spectrum. The repeated occurrence of single molecular blinking events within this highlighted region are spatially clustered in close vicinity. In conventional SMLM image reconstruction, these blinking events are treated independently, leading to a cluster of localizations without knowledge of their exact origins as shown in Fig. 6.2(d).

From the spectral image, we extracted spectral centroids (SCs) [9, 19] to represent the spectroscopic signature of each QD. We calculate SC as

$$\lambda_{\text{SC}} = \frac{\sum_{\lambda} \lambda I(\lambda)}{\sum_{\lambda} I(\lambda)} \tag{6.1}$$

where λ is the emission wavelength and $I(\lambda)$ is the spectral intensity at λ. As shown in Fig. 6.2(e), the SC distribution of the blinking events from the highlighted region reveals three distinct

distributions. Such a SC distribution suggests that the highlighted region may contain three QDs and these QDs demonstrated distinct spectroscopic signatures, which are 580.3 ± 3.3 nm (QD1), 592.5 ± 1.6 nm (QD2), and 619.4 ± 2.8 nm (QD3), as the result of SH. For reference, individual frames showing each spatial and spectral image of QD1, QD2 and QD3 with the corresponding emission are shown in Fig. 6.3. Based on the SCs, we can identify and classify the origin of each detected blinking event to one of the three QDs. The first 100 repeated blinking events originating from each of the three QDs after classification were further selected to demonstrate the principle of PACER. Their corresponding spectra and SCs were shown in Fig. 6.2(f).
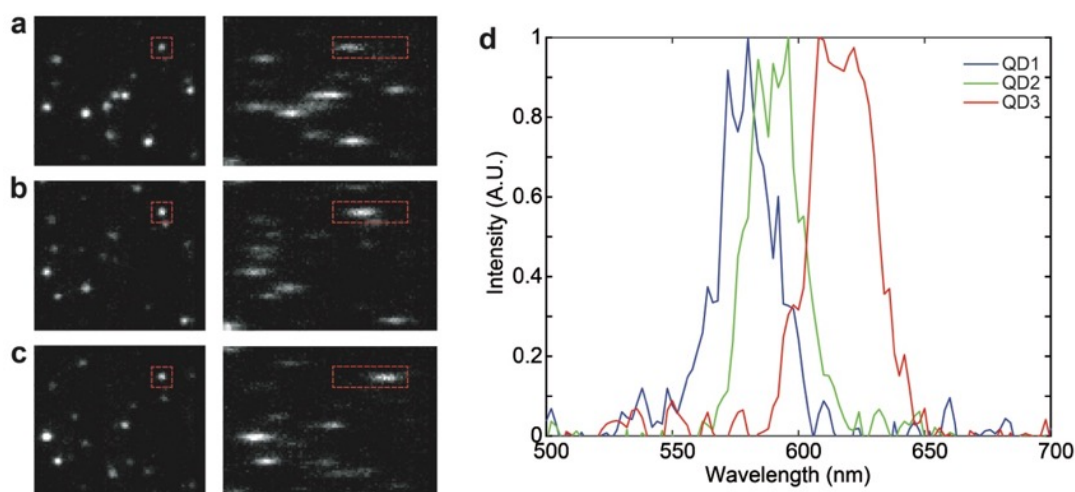
Figure 6.3 Identification of individual QDs. (a-c) Single frames with emission from QD1, QD2 and QD3 respectively occurring from the same location highlighted in the red dashed box. (d) Normalized emission spectra of QD1, QD2 and QD3 extracted from spectral images in (a-c).

The observed SH establishes the foundation for PACER to discriminate individual molecules from the ensemble populations based on their spectroscopic signature. In PACER, the emitted photons originated from repeated blinking of the same QD can all be combined to collectively improve the localization precision. Figure 6.2(g) illustrates the improved localization precision with respect to increasing number of NB, where we overlay three rendered QDs with pseudo-

colors. When NB=1 the localization precision is limited to 17.0 nm, corresponding to an average of 250 photons in the spatial image. Such a localization precision is insufficient to spatially distinguish the three QDs in the reconstructed image (Fig. 6.2(g), NB=1). After applying PACER, we can positively classify all stochastic blinking events to their respective true origins based on their unique heterogeneous fluorescence emission spectra. After classifying the origins of the blinking events, we accumulate photons from repeated blinking events that are from the same QD from multiple recorded frames to increase the total photon number and, thus, to improve the localization precision. Accumulating photons from 10 blinking events (Fig. 6.2(g), NB=10) leads to a more than 3-fold improvement in localization precision to ~4.9 nm, where three QDs can be resolved in the reconstructed sSMLM image. When NB=100, an approximated 10-fold improvement in localization precision to ~1.7 nm shows that QD2 and QD3 are 6.1 nanometers apart. Considering QDs have the mean diameter of 5.2 nm, it is possible that QD2 and QD3 are almost in contact. Figure 6.2(h) shows the line profiles of the reconstructed image across the QD2 and QD3 with NB of 1, 10, 100, further illustrating the improvement in localization precision as NB increases.

6.3.2 Imaging DNA nanorulers with PACER
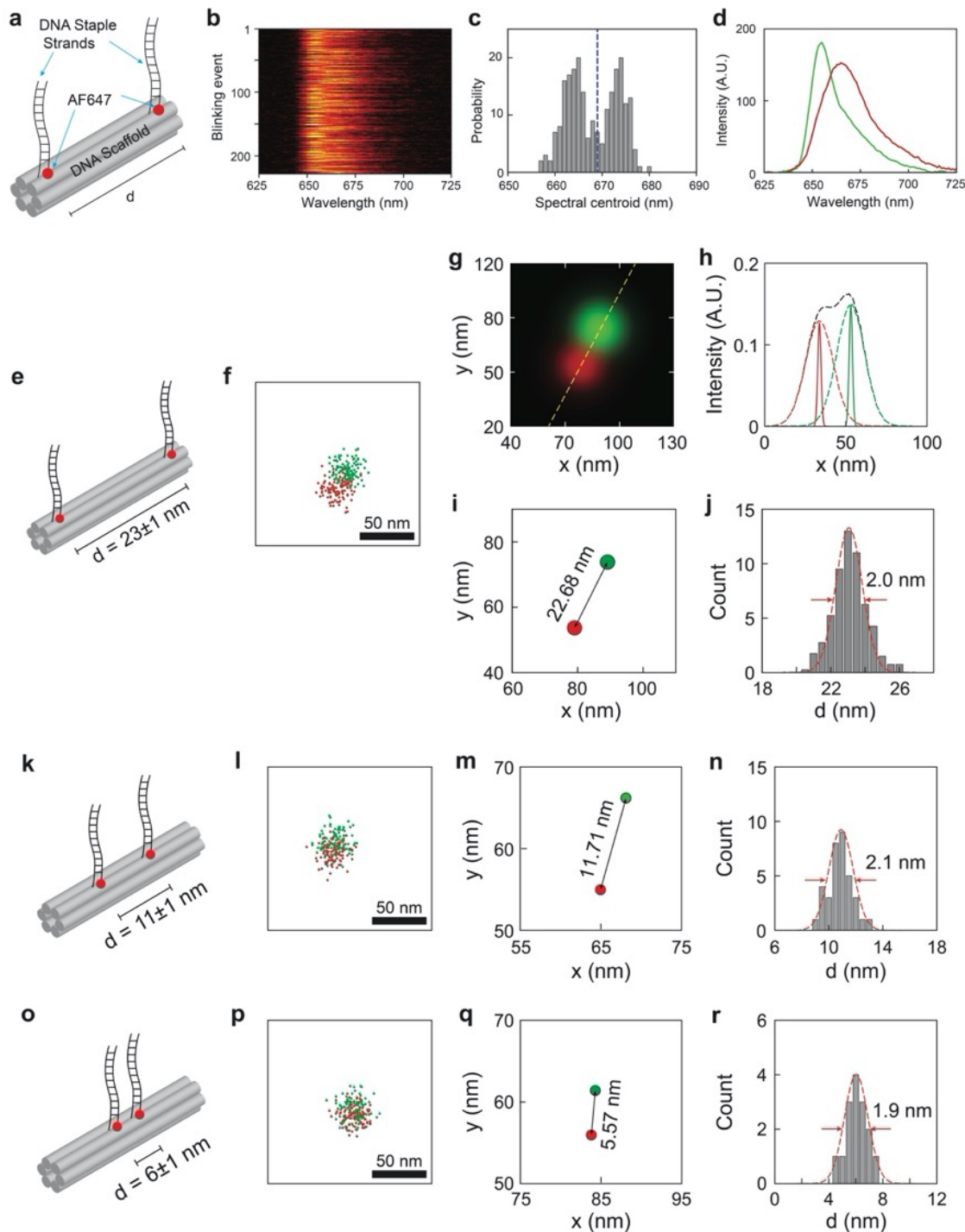
Figure 6.4 Experimental validation of PACER using DNA nanoruler samples. (a) Schematic illustration of a DNA nanoruler labeled with a pair of AF647 featuring a

predefined mark-to-mark distance. (b) Representative emission spectra of two molecules on one nanoruler. (c) Histogram of SCs indicates the existence of two molecules with distinct spectral signatures on one nanoruler. (d) The average spectra of the two molecules separated by SC at the wavelength of 669 nm. (e) Schematic of a DNA nanoruler featuring mark-to-mark distance of 23 nm. (f) The scatter plot and (g) the rendered sSMLM image of localization events with colors indicating distinct spectral signatures after stage drift correction. (h) Comparison of molecule location in SMLM image (the dashed black line) and sSMLM images without (the dashed colored lines) and with (the solid colored lines) PACER. (i) Calculated location of molecules through PACER. (j) Histogram of mark-to-mark distance measured from 57 nanorulers. The representative results of a DNA nanoruler featuring mark-to-mark distance of (k-n) 11 nm and (o-r) 6 nm.

Upon successful demonstration of improved localization precision using QDs sample, we further experimentally validate PACER using the model system with known inter-molecular spacing. Figure 6.4 shows the results of PACER resolving up to 6-nm spacing in DNA nanorulers (Gatta-Storm Nanoruler, Gattaquant GMBH) labeled with AF647 fluorescent molecules. The nanoruler comprises DNA origami backbone with precise placement of two fluorescence molecules at controllable inter-molecular spacing [88, 89] (Fig. 6.4(a)). We acquired 2,000 frames with an integration time of 10 ms per frame. The recorded spectra of all the individual stochastic blinking from the nanoruler sample labeled with two AF647 molecules are plotted in Fig. 6.4(b) and the corresponding histogram of the SCs is shown in Fig. 6.4(c). Nanoruler samples with contrast in the measured SC histogram exceeding the threshold value of 20% are accepted. Two distinct peaks with mean SCs separated by approximately 10 nm, which underlie the effect of SH of AF647, can be clearly observed in Fig. 6.4(c). Each individual molecule exhibits consistent emission spectra during stochastic switching, with the measured spectral precision less than 2 nm, as estimated by the Standard Deviation (S.D.) of the SC distribution. The averaged fluorescent

spectra of the two AF647 molecules are shown in Fig. 6.4(d) after classification based on Fig. 6.4(c).

We imaged nanorulers with inter-molecular spacing values of 23 nm (Fig. 6.4(e)), 11 nm (Fig. 6.4(k)), and 6 nm (Fig. 6.4(o)). After classifying each localized event to one of the two AF647 molecules and corrected the stage drift based on the position of a fiducially marker, the scatterplot of all the localized blinking events is color-coded in red and green to represent the origins of the two AF647 molecules (Fig. 6.4(f)). Two molecules can be readily separated with colors indicating distinct spectral signatures after classification as shown in Fig. 6.4(g). After PACER, the localization precision improved from 18.2 nm to 2.6 nm, as denoted by the red and green solid lines in Fig. 6.4(h). The measured distance between the imaged two molecules is 22.7 nm (Fig. 6.4(i)). Figure 6.4(j) shows the histogram of the measured inter-molecular spacing from all the 57 nanoruler samples, which shows a mean value of 23.2 nm with a S.D. of 0.8 nm. It agrees well with the expected value of 23 ± 1 nm according to manufacturer's specification.

Figure 6.4(k) illustrates the nanorulers with an inter-molecular spacing of 11 nm. The color-coded scatter plot of the localization events and the reconstructed PACER image after drift correction of one representative sample are shown in Figs. 6.4(l) and 6.4(m), respectively. Figure 6.4(n) is the histogram of the measured inter-molecular spacing from 35 nanoruler samples, showing the mean spacing of 10.8 nm with a S.D. of 0.9 nm. Again, it agrees well with the expected value of 11 ± 1 nm according to manufacturer's specification. Finally, we performed PACER on the nanoruler sample with inter-molecular spacing of 6 nm (Fig. 6.4(o)). The corresponding results are shown in Figs. 6.4(p) and 6.4(q). The histogram of the measured inter-molecular spaces from 15 nanoruler samples shown in Fig. 6.4(r) indicates the mean spacing of 6.1 nm with S.D. of 0.8

nm, which agrees well with the expected value of 6 ± 1 nm according to manufacturer's specification. Thus, even in a rather challenging case, using AF647 with rather weak SH, PACER can still successfully resolve the fluorescent molecules at the inter-molecular spacing of 6-nm distance, which represent 5-fold improvement in the localization precision under the identical experimental conditions.

6.3.3   Imaging DNA origami nanogrids with PACER
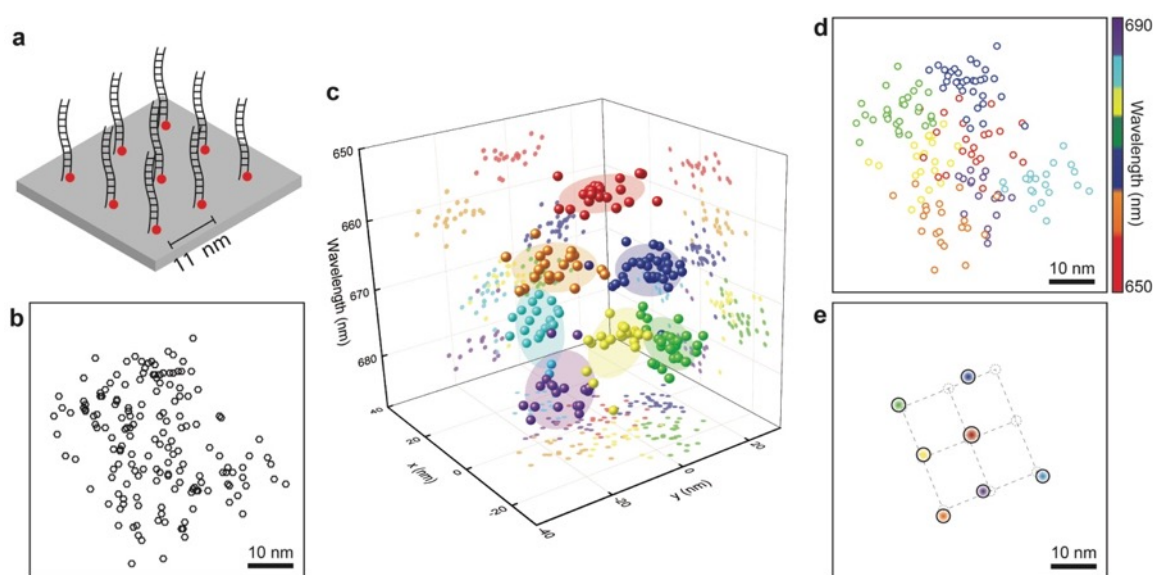
Figure 6.5 PACER imaging DNA origami nanogrids consisting of a 3×3 array of AF647 fluorescent molecules with 11-nm inter-molecular spacing. (a) Schematic illustration of the DNA origami nanogrid labeled with 3×3 array of AF647 with 11-nm inter-molecular spacing. (b) Conventional SMLM reconstruction of all stochastic blinking events. (c) All events can be separated to seven clusters based on their spatial locations and SCs in the extended spatial-spectral domain. (d) The corresponding sSMLM reconstruction with pseudo-colors assigned to seven clusters. (e) Locations of fluorophores calculated after PACER. Black circles represent the localization precision after PACER. The gray dashed circles represent the best guess of the location and orientation of the nanogrid.

Finally, we tested PACER in identifying individual fluorescent molecule from a densely packed cluster. We imaged DNA origami nanogrids (Brightness 9R, GattaQuant GMBH) consisting of a 3×3 array of AF647 fluorescent molecules with a uniform inter-molecular spacing

of 11 nm (Fig. 6.5(a)). While initially being developed as a brightness standard, the same nanogrid was used by Stefan Hell's group in the development MINFLUX method to represent densely packed fluorescent-labeled samples [83]. The average number of photons recorded from AF647 molecules in the spatial image is 834 photons, leading to a localization precision of 9.21 nm and a spatial resolution of 21.69 nm. Thus, it is impossible to spatially resolve individual AF647 molecules at inter-molecular spacing of 11 nm from reconstructed SMLM image (Fig. 6.5(b)). However, capturing the spectral signature associated with each blinking events provides additional information to better sperate the otherwise overlapping localization events in the extended spatial-spectral domain. Figure 6.5(c) shows the scatter plot of the same localization events in the spatial-spectral domain, with SCs of each blinking events being used to represent the spectral coordinates. We applied a k-means cluster analysis, a built-in function in MATLAB [90] to classify the localization events into seven clusters based on the spatial coordinates and SCs and then assigned pseudo-colors to seven clusters. Figure 6.5(d) is the corresponding sSMLM image with pseudo-colors to the seven clusters. Figure 6.5(e) shows the final PACER sSMLM image with an average NB of 23.7 for the seven clusters. On average, the improved localization precision is 3.7 nm and the improved spatial resolution of 8.7 nm, which resolved the majority of the AF647 molecules in the nanogrid. The gray circles show the best guesses of the locations and orientations of the nanogrid, indicates a great match of six but with one molecule mislocated (the blue dot in Fig. 6.5(e)). This is likely due to a manufacturing artifact or misidentification of fluorophores at neighboring labeling sites which happens to exhibit similar spectral signatures [82, 83, 91].

.

6.4   CONCLUSION AND DISCUSSION

In this study, we demonstrated a single-digit nanometer resolution that can be achieved by combining sSMLM and PACER. We first validated its feasibility of distinguishing molecules/particles of the same type by capturing the intrinsic SH. By using the spectroscopic signature as a unique identifier, photons from individual molecules can now be accumulated in achieving greatly improved localization precision. We have experimentally validated sub-2-nm localization precision using QDs, and synthetic DNA origami nanostructures (nanorulers and nanogrids) with the smallest feature size of 6 nm. The experimental results indicate that spectroscopic signature of individual molecules would greatly benefit molecular identification and resolution improvement using PACER. This technique offers significantly improved image resolution over the conventional SMLM technique but remains compatible with the existing fluorescence labels and imaging protocols. The broad accessibility and the molecular-scale resolution can potentially provide new insights into biological phenomena and enable significant research progress to be made in the life sciences.

Chapter 7

Compact 3D spectroscopic single-molecule localization microscopy using a dual-wedge prism-based lensless spectrometer

We propose a compact 3D sSMLM design using a dual-wedge prism (DWP)-based lensless spectrometer. We show its feasibility using ray-tracing and numerical simulation. The proposed DWP unit disperses the incident beam without beam deviation, which allows for manufacturing a single unit of the optical element. It thus significantly reduces optical alignment requirement and minimizes its absolute transmission loss, which results in an improved localization precision.

7.1 INTRODUCTION

Spectroscopic single-molecule localization microscopy (sSMLM) simultaneously provides spatial and spectral information of fluorescent molecules. It has been demonstrated as a powerful tool for cell biology and material science [3-7, 72]. Existing sSMLM implementations can be classified into two categories: (1) prism-based [3, 6, 72] and (ii) grating-based designs [4, 5, 7]. In prism-based sSMLM, it suffers from an inherent difficulty as it splits the collected photons into two separate optical beam paths, using a beam splitter (BS) and additional discrete optical components, to simultaneously form spatial and spectral images. Spectral analysis of sSMLM requires a precise mapping of the recorded spatial and spectral images, which imposes stringent requirement of precise alignment of these discrete optical components. It thus requires users with

sophisticated optical alignment skills to achieve and maintain optimal performance of sSMLM systems.

In contrast, grating-based sSMLM better addresses these practical issues. It uses one diffraction grating to separate an incident beam into 0th and 1st diffraction orders, both of which are imaged onto a camera using the same imaging lens. Grating-based design significantly reduces the number of required discrete optical components [4, 7] and improves system's reliability. However, grating-based design has its own limitations. Specifically, the 1st diffraction order beam has angular incidence with respect to the imaging lens (or an optical axis), which is prone to induce geometrical and chromatic aberrations especially for high groove density gratings. Both aberrations may undermine localization uncertainty, either accuracy or precision, of the reconstructed image and the spectra analysis. The worsen uncertainty is particularly problematic in three-dimensional (3D) sSMLM using either astigmatism or biplane method as extra discrete optical elements, such as a cylindrical lens or pickoff mirrors, are necessary [46, 63]. Hence, 3D grating-based sSMLM further required users to have with advanced expertise in optical instrumentation. Moreover, gratings often have higher transmission losses (~30%) comparing with prisms, which reduces photon budgets for spatial imaging and spectral analysis. The transmission loss issue has not yet been fully addressed in grating-based sSMLM.

To make sSMLM accessible by biology research community, we aim to (1) vastly reduce the number of discrete optical components for simplified optical configuration and alignment and (2) significantly improve transmission loss. We designed a compact optical assembly using dual-wedge prism (DWP), referred to as DWP unit, to achieve our goals. By integrating the DWP unit into a lensless spectrometer, we can achieve 2D sSMLM with improved spatial precisions.

7.2 METHODS

7.2.1 3D sSMLM module using dual wedge prism lesless spectrometer
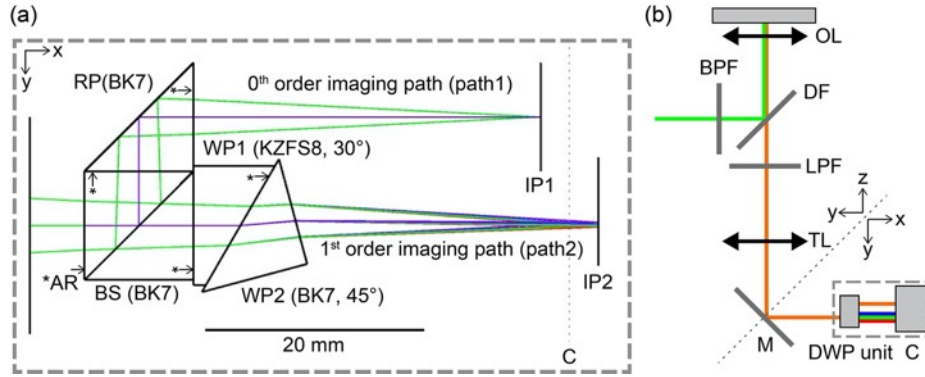
Figure 7.1 (a) Proposed 3D sSMLM module design using Zemax. The preliminary model was demonstrated using off-the-shelf optics; (b) Optical setup of the integrated 3D sSMLM system. BS: cube beam splitter; RP: right-angle prism; WP: wedge prism; AR: anti-reflection; OL: objective lens; BPF: band pass filter; DF: dichroic filter; LPF: long pass filter; TL: tube lens; M: mirror; DWP unit: dual-wedge prism unit; IP: Image plane; C: Camera.

Fig. 7.1(a) illustrates the DWP unit, which consists of a cube BS with a 1:1 split ratio, a right-angle prism (RP), and two wedge prisms (WP) that have different refractive index values. The incident beam is first split into two beam paths by the BS. The reflected beam (path 1) by the BS is further reflected by the RP towards the horizontal direction to form a spatial image at its corresponding image plane (IP1). The transmitted beam (path 2) passes through WP1 (KZFS8 material, $n=1.79$ at 550 nm) and WP2 (BK7 material, $n=1.52$ at 550 nm) to be spectrally dispersed parallel to the horizontal direction. This design was inspired by grating-prism or Grism, which has been widely used for spectroscopy in astronomy [92]. As a result, the dispersed beam ensures the flatness of the spectral image formed at its corresponding image plane (IP2). All incident surfaces of optics are anti-reflection coated to minimize transmission loss. This DWP unit permits an in-line optical layout because light is dispersed while canceling out the beam deviations with respect to an optical axis (or an image plane of a camera) by WP1 and WP2.

We adjusted the optical path length difference between the path 1 and the path 2 to ~4 mm for axial separation of IP1 and IP2, which enables 3D biplane imaging, as described in our previous work [46]. We cemented all the optical components together to form the single DWP unit and the size of each component can be customized based on a specific requirement. In this work, we used off-the-shelf optical components for feasibility test and its layout is shown in Fig. 7.1(a). We selected WP1 (PS873-A, Thorlabs, KZFS8 material, a wedge angle of 30°) for mainly dispersing the beam to obtain emission spectra of single molecules and WP2 (PS910H-A, Thorlabs, BK7 material, a wedge angle of 45°) to compensate for the deviation angle of WP1, together with a cube BS (BS010, Thorlabs, BK7 material) and a RP (PS910L-A, Thorlabs, BK7 material).

7.2.2 Optical setup of the integrated 3D sSMLM system

Fig. 7.1(b) shows the schematic of sSMLM using the new DWP unit, which is placed in front of a scientific complementary metal–oxide–semiconductor (sCMOS) camera (Prime95B, photometrics). The overall system is based on an inverted optical microscope (Eclipse Ti-U, Nikon), equipped with 647-nm laser (2RU-VFL-P-2000-647-B1R, MPB communications) with 2-W maximum output and an objective lens (100x, NA1.49, CFI apochromat TIRF, Nikon). The filter set consisted of a band-pass filter (FF01-642/10-25, Semrock), a dichroic mirror (FF649-DI01-25X36, Semrock), and a long-pass filter (BLP01-647R-25, Semrock). The emitted fluorescence is guided by a mirror to the DWP unit after passing through the tube lens (TL). The fluorescence is further divided into a non-dispersed spatial channel and a spectrally dispersed spectral channel, and then captured by the sCMOS camera, which is placed in the middle of the two IPs, which is highlighted by C in Fig. 7.1(a).

7.3   RESULTS

7.3.1   Qualitative evaluation of the 3D sSMLM module using Zemax
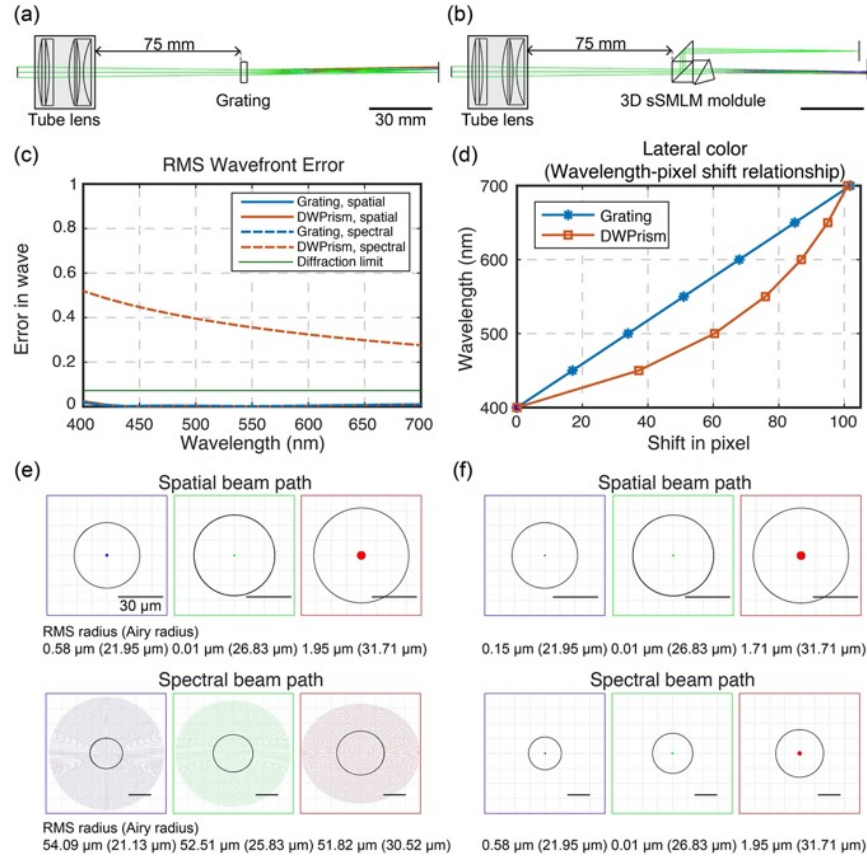
Figure 7.2 Layout of (a) the grating-based and (b) the proposed DWP-based designs using Zemax. (c) Simulated RMS wavefront errors of spatial and spectral beam paths in both designs. (d) Wavelength-pixel shift relationship. Simulated spot diagrams at different wavelengths (from the left to right: 450, 550, and 650 nm; from the top to bottom: spatial and spectral beam paths) for (e) the grating-based and (f) the DWP-based designs. We used a groove density of 50 grooves/mm showing comparable SD value to the proposed DWP-based design using off-the-shelf optics. Overall SD of bot designs is 3nm/pixel. Scale bar: 30 μm in (e) and (f).

The proposed design was firstly evaluated using Zemax in comparison with the existing grating-based design. Figures 7.2(a) and 7.2(b) show layouts of the grating-based and DWP-based designs, respectively. In both designs, an incident beam was focused by a TL, which was modeled an actual microscope component reported in [93]. And, the proposed module or the grating was

placed a 75-mm distance from the TL. As shown in Fig. 7.2(c), the simulated root-mean-square (RMS) wavefront errors in both designs are significantly lower than the reference diffraction-limited criterion over the visible range except for a spectral beam path in the DWP-based design, which shows the error less than 0.5 wave. This result indicates that both designs offer the diffraction-limited performance in the spatial image. Although slight errors observed in the spectral beam path for the DWG-based design may influence the PSF in the y-axis in spectral image, the error in the spectral image is not coupled with lateral spatial localization. Besides, calculating spectral centroid (SC) is tolerant enough to characterize emission spectra of single molecules and its influence on spectral precision is negligible [3, 7, 13, 19].

Figure 7.2(d) shows a wavelength-pixel shift relationship, which indicates an achievable spectral dispersion (SD) [19] considering a given configuration and a camera pixel size of 11 μm. The grating is known for its linear dispersion (the blue curve in Fig. 7.2(d)) while the prism shows non-linear dispersion (the orange curve in Fig. 7.2(d)), which can be fitted using a third polynomial equation [3]. Overall, both designs provide an SD of 3 nm/pixel and, notably, the DWP-based design offers an optimal SD for multi-color imaging in a far-red channel, reported as ~ 6nm/pixel [7]. Figures 7.2(e) and 7.2(f) show spot diagrams at different wavelengths in the grating-based and the DWP-based designs, respectively. The diffraction-limited performance of the spatial beam paths in both designs was also demonstrated by spots diagrams, as shown in Figs. 7.2(e) and 7.2(f); We observed 0.147-μm RMS radius with 21.95-μm Airy Radius in the DWP-based design and 0.147-μm RMS radius with 21.95-μm Airy Radius in the grating-based design, at 450 nm as an example.
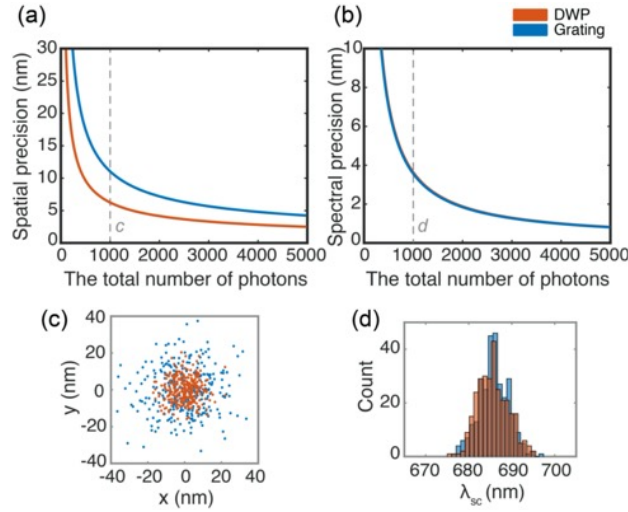
Figure 7.3 (a) Theoretically estimated lateral spatial precision and (b) spectral precision of the grating-based and the proposed DWP-based designs. (c) Scatterplot of spatial precision and (d) histogram of spectral precision of both designs at 1000 photons.

We further estimated spatial and spectral precisions of the proposed DWP-based design and compared it with the grating-based sSMLM system, which generally contains a transmission grating and two imaging lenses [7, 13]. Given manufacturer's specifications, we assumed absolute transmission loss (at 670 nm) of 1 % for each lens and 30 % for the grating in the grating-based sSMLM system, and 5 % for BS, 0.5 % for RP, 3 % for WP1 and 0.5 % for WP2 in the DWP-based sSMLM system. It should be noted that we only considered the transmission loss of materials, in this estimation, by ignoring any absorption loss. Accordingly, absolute transmission efficiencies of the spatial and spectral images in the grating-based sSMLM system are 14 % and 42 %, respectively, given a quantum efficiency of the used sCMOS camera (85 % at 670 nm) and a previously reported ~1:3 split ratio [7, 13]. And, absolute transmission efficiencies of the spatial and spectral images in the DWP-based sSMLM system are 38 % and 41 % for, respectively. Then, we estimated lateral spatial precisions using Eq. (7.1) [18] and spectral precision using Eq. (7.2) [19].

$$\Delta x^2 = \frac{\sigma^2 + a^2/12}{N}\left(1 + 4\tau + \sqrt{\frac{2\tau}{1+4\tau}}\right) \qquad (7.1)$$

where $\tau = 2\pi(b + n_{ro}^2)(\sigma^2 + a^2/12)/Na^2$, σ is the standard deviation of the Gaussian function

(nm); a is the back-projected pixel size (nm); N is the number of detected photons; b is the number

of background photons per pixel; and n_{ro} is the readout noise (e-);

$$\sigma_\lambda^2 = \frac{s_\lambda^2}{N} + \frac{1024 n_{bg}^2 s_\lambda^3 s_y}{3\Delta\lambda\Delta y N^2} + \frac{1024 n_{ro}^2 s_\lambda^3 s_y}{3\Delta\lambda\Delta y N^2} \qquad (7.2)$$

where s_λ and s_y are standard deviations of the Gaussian function along the spectral-axis and the

y-axis (nm); n_{bg}^2 is the number of background photons per pixel; $\Delta\lambda$ is the SD (nm/pixel); Δy is

the back-projected pixel size along y-axis (nm).

As shown in Fig. 7.3(a), we observed the proposed DWP-based design offers a significantly

improved lateral spatial precision, almost doubled precision, (as 6.42 nm at 1000 photons),

compared with the grating-based design (11.65 nm). This improvement is primarily originated

from higher transmission efficiency of the dispersive prism itself comparing to the grating.

Meanwhile, both provides comparable spectral precisions (3.42 nm for the DWP-based design and

3.36 nm for the grating-based design) as their absolute transmission efficiencies are quite similar.

We further performed a numerical simulation to understand a physical behavior of each parameter

under realistic experimental conditions and compared with the results obtained by the analytical

solution. The numerical simulations were implemented in the same manner described our previous

works in Ref. [46] (for the spatial precision) and Ref. [19] (for the spectral precision). All the

related key parameters used in the estimation are listed in Table. 7.1. From the numerical

simulation, we obtained the spatial precisions of 6.66 nm in the DWP-based design and 12.71 nm

in the grating-based design (Fig. 7.3(c)), while we observed similar spectral precisions as 3.61 nm in the DWP-based design and 3.42 nm in the grating-based design (Fig. 7.3(d)), which nicely have matched with the analytical solution. These results suggest that the proposed design allows not only for reduced system complexity but also better photon utilization, which potentially can facilitate the limited photon budget issues in sSMLM.

Table 7.1 List of parameters used in analytical solutions.

	σ (nm)	a (nm)	b (photons/pixel)	n_{ro} (e-)		
For Δx						
	96	110	5	1.6		

	s_λ (nm)	s_y (nm)	n_{bg}^2 (photons/pixel)	n_{ro} (e-)	$\Delta\lambda$ (nm/pixel)	Δy (nm)
For σ_λ						
	20	96	5	1.6	6	110

Table 7.2 List of parameters used in simulations.

Pixel size (µm)	QE @ 670 nm (%)	Readout noise (e-)	Background (photons)	Standard deviation of PSF (nm)	Precision	Signal (photons)	Iteration number	Spectral dispersion (nm/pixel)	Axial separation (nm)
					For lateral	1000	300	-	
11	85	1.6	5	96	For spectral	1000	300	6	
					For axial	3000	1000	-	450
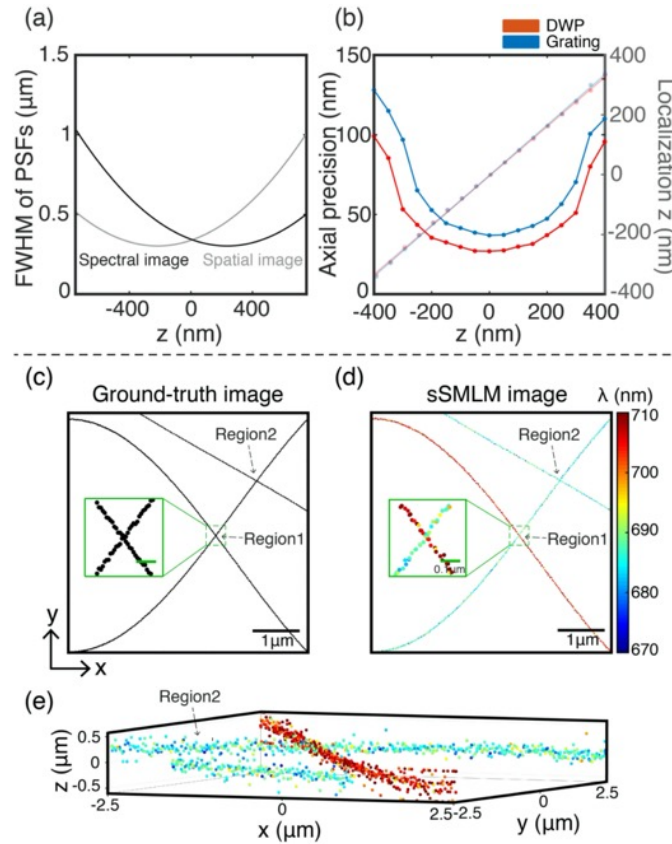
Figure 7.4 (a) Depth calibration curve of biplane imaging. (b) Theoretically estimated axial spatial precision of the grating-based and the proposed DWP-based designs. (c) 2D projection of Simulated 3D image with a labeling density of 100 molecules/μm along the line structure. (d) Reconstructed sSMLM image with pseudo colors corresponding to the SC of single molecules. (e) The corresponding 3D scatter plot.

We further extended the numerical simulation into 3D to estimate axial spatial precision of the proposed 3D sSMLM module. As shown in Fig. 7.2(b), the proposed design using the off-the-shelf-optics has an optical path difference of ~ 4 mm between the spatial (IP1) and spectral (IP2) image planes, which can be converted to an axial separation of ~ 450 nm given a magnification of the objective lens according to Ref. [94]. Based on this axial separation, we first generated an ideal 3D calibration curve for biplane imaging, as shown in Fig. 7.4(a), which shows the full width at the half maximum (FWHM) of PSFs along the y-axis in both spatial and spectral images. This calibration curve was used to generate PSFs at different depths as ground-truth. Using the

generated PSFs, we estimated the axial precision of the biplane sSMLM system in the same manner previously reported in Ref. [46]. Figure 7.4(b) shows the estimated axial precision (the left vertical axis) and the reconstructed localization z-position (the right vertical axis). As a result, we obtained the axial precision of 26.9 nm for the proposed DWP-based design and 36.8 nm for the grating-based design, respectively, at 0-nm depth with a signal of 3000 photons and a background of 5-photons/pixel, as an example. This corresponds to 27% improvement.

To validate the 3D spectroscopic imaging capability of the proposed 3D sSMLM module, we applied it to a realistic simulated data set, which consists of filaments in 3D (Fig. 7.4(c)), with a size of 5x5x0.8 μm^3 and a labeling density of 100 molecules/μm along the line structure. The other characteristics parameters used in the simulation are listed in Table 7.2. Figure 7.4(d) shows the reconstructed sSMLM image with pseudo colors corresponding to SCs of single molecules. Notably, we successfully distinguished two filaments labeled with different species near one of cross-sections (region 1 in Figs. 7.4(c) and 7.4(d)) using SC, as shown in the inset of Fig 7.4(d), which is beyond the capability of existing SMLM technologies shown in the inset of Fig. 7.4(c). Furthermore, the simultaneous acquired 3D information enables to clearly distinguish another cross-section (region 2 in Figs. 7.4(c-e)), as shown in Fig. 7.4(e).

7.4 CONCLUSION AND DISCUSSION

In this work, we proposed a 3D sSMLM design with a DWP-based lensless spectrometer. Through the simulations, we estimated theoretically achievable spatial and spectral precisions. We also compared the results with those of the existing grating-based design. Finally, we validated its 3D spectroscopic single-molecule imaging capability using the realistic simulated data set as an example, which shows the potential to uncover rich information about single molecules for

fundamental understanding of subcellular structures and nanomaterial properties. In particular, the proposed 3D sSMLM module eliminates alignment of additional discrete optical components and ensures straightforward implementation and reliable operation of the 3D sSMLM system, through manufacturing a single piece of the compound optical element. We believe its compactness allows for an easy integration into the conventional fluorescence microscope system and make sSMLM broadly accessible by users in biology research community.

Chapter 8

Conclusion and future works

This dissertation has provided technical advances in sSMLM to improve spatial resolution and spectral precision of single molecules. It covered a range of topics under this overall goal: (1) We first established a theoretical framework to evaluate the sSMLM performance using numerical simulation and analytical solution; (2) We developed new optical configurations and post-data processing techniques. Specifically, four new techniques were introduced: (i) tunable spectral dispersion sSMLM, (ii) 3D biplane sSMLM, (iii) SDsSMLM, and (iv) PACER; (3) We experimentally validated their multimodal imaging capability using biology samples and nanoparticles; and (4) We proposed a compact optical device integrating all demonstrated 3D sSMLM functionalities. There studies offer comprehensive technical guidance for better designing and optimizing the sSMLM system and thus provides an opportunity to investigate nanoscopic biological and non-biological 3D structures with spectroscopic analysis at precision levels previously far out of reach.

Future work in sSMLM is expected to address two technical issues: temporal resolution and 3D axial range. Despite a significant spatial resolution improvement of sSMLM compared with the conventional fluorescence microscopy, its temporal resolution is relatively slow. To reconstruct an image, tens of thousands of frames should be recorded, resulting in a temporal resolution of ~ 10 minutes. The slow acquisition time may cause practical issues, such as sample drift and frequent imaging buffer replacement, which reduce the reliability of the experiment. With a better handling of the sample preparation in sSMLM, techniques based on temporal fluctuation

correlation, deconvolution image estimation, or machine learning image reconstruction, can be promising to improve temporal resolution of sSMLM and alleviate practical constraints caused by slow acquisition time.

In addition, currently reported 3D sSMLM techniques, including astigmatism-based and biplane-based methods, are restricted to thin samples, typically less then 4 μm, near the coverslip. This is primarily due to background coming from out-of-focus fluorophores. This background reduces not only the axial spatial precision of each emitter but also its lateral spatial and spectral precisions, which ultimately prevents imaging in thick cells. Combining 3D biplane sSMLM with light sheet illumination techniques can be a promising solution to significantly improve localization precision and the axial range per splice. It thus will be able to improve 3D imaging in thick samples, together with a slicing scanning method.

Lastly, we expect to develop the sSMLM system that acquires the spectroscopic signature without a spectral channel. All reported sSMLM techniques require a dispersive element, such as a grating, a prism, or a diffractive optic to acquire emission spectra of individual molecules. Thus, it sacrifices the limited photon budget of each emitter, which reduces the localization precision. As discussed so far, the ultimate goal of this dissertation has been to address the aforementioned issue by better understanding a correlation between spatial and spectral channels and, thus, efficiently utilizing a given photon budget. Ironically, we may not need to face this issue unless we have two separate channels using dispersion. In other words, it would be ideal if we could extract spectroscopic signatures from the PSF itself in the spatial channel. Wavelength-dependent phase variation or wavelength-induced chromatic aberration detection techniques can be interesting alternatives to broaden technical perspectives of sSMLM.

References

1. S. J. Sahl, S. W. Hell, and S. Jakobs, "Fluorescence nanoscopy in cell biology," Nature Reviews Molecular Cell Biology **18**, 685-701 (2017).

2. B. Huang, M. Bates, and X. Zhuang, "Super-resolution fluorescence microscopy," Annual Review of Biochemistry **78**, 993-1016 (2009).

3. Z. Zhang, S. J. Kenny, M. Hauser, W. Li, and K. Xu, "Ultrahigh-throughput single-molecule spectroscopy and spectrally resolved super-resolution microscopy," Nature Methods **12**, 935-938 (2015).

4. M. N. Bongiovanni, J. Godet, M. H. Horrocks, L. Tosatto, A. R. Carr, D. C. Wirthensohn, R. T. Ranasinghe, J. E. Lee, A. Ponjavic, J. V. Fritz, C. M. Dobson, D. Klenerman, and S. F. Lee, "Multi-dimensional super-resolution imaging enables surface hydrophobicity mapping," Nature Communications **7**, 13544 (2016).

5. B. Dong, L. Almassalha, B. E. Urban, T. Q. Nguyen, S. Khuon, T. L. Chew, V. Backman, C. Sun, and H. F. Zhang, "Super-resolution spectroscopic microscopy via photon localization," Nature Communications **7**, 12290 (2016).

6. M. J. Mlodzianoski, N. M. Curthoys, M. S. Gunewardene, S. Carter, and S. T. Hess, "Super-Resolution Imaging of Molecular Emission Spectra and Single Molecule Spectral Fluctuations," PLoS One **11**, e0147506 (2016).

7. Y. Zhang, K.-H. Song, B. Dong, J. L. Davis, G. Shao, C. Sun, and H. F. Zhang, "Multicolor super-resolution imaging using spectroscopic single-molecule localization microscopy with optimal spectral dispersion," Applied Optics **58**, 2248-2255 (2019).

8. J. K. Trautman, J. J. Macklin, L. E. Brus, and E. Betzig, "Near-Field Spectroscopy of Single Molecules at Room-Temperature," Nature **369**, 40-42 (1994).

9. H. P. Lu, and X. S. Xie, "Single-molecule spectral fluctuations at room temperature," Nature **385**, 143-146 (1997).

10. W. E. Moerner, "A dozen years of single-molecule spectroscopy in physics, chemistry, and biophysics," Journal of Physical Chemistry B **106**, 910-927 (2002).

11. D. Kim, Z. Zhang, and K. Xu, "Spectrally Resolved Super-Resolution Microscopy Unveils Multipath Reaction Pathways of Single Spiropyran Molecules," Journal of the American Chemical Society **139**, 9447-9450 (2017).

12. S. Moon, R. Yan, S. J. Kenny, Y. Shyu, L. Xiang, W. Li, and K. Xu, "Spectrally Resolved, Functional Super-Resolution Microscopy Reveals Nanoscale Compositional Heterogeneity in Live-Cell Membranes," Journal of the American Chemical Society **139**, 10944-10947 (2017).

13. J. L. Davis, Y. Zhang, S. Yi, F. Du, K. H. Song, E. A. Scott, C. Sun, and H. F. Zhang, "Super-Resolution Imaging of Self-Assembled Nanocarriers Using Quantitative Spectroscopic Analysis for Cluster Extraction," Langmuir **36**, 2291-2299 (2020).

14. S. J. Lord, H.-l. D. Lee, and W. E. Moerner, "Single-Molecule Spectroscopy and Imaging of Biomolecules in Living Cells," Analytical Chemistry **82**, 2192-2203 (2010).

15. J. L. Davis, B. Dong, C. Sun, and H. F. Zhang, "Method to identify and minimize artifacts induced by fluorescent impurities in single-molecule localization microscopy," Journal of Biomed Optics **23**, 1-14 (2018).

16. K. I. Mortensen, L. S. Churchman, J. A. Spudich, and H. Flyvbjerg, "Optimized localization analysis for single-molecule tracking and super-resolution microscopy," Nature Methods **7**, 377-381 (2010).

17. G. T. Dempsey, J. C. Vaughan, K. H. Chen, M. Bates, and X. Zhuang, "Evaluation of fluorophores for optimal performance in localization-based super-resolution imaging," Nature Methods **8**, 1027-1036 (2011).

18. B. Rieger, and S. Stallinga, "The Lateral and Axial Localization Uncertainty in Super-Resolution Light Microscopy," A European Journal of chemical physics and physical chemistry **15**, 664-670 (2014).

19. K.-H. Song, B. Dong, C. Sun, and H. F. Zhang, "Theoretical analysis of spectral precision in spectroscopic single-molecule localization microscopy," Review of Scientific Instruments **89**, 123703 (2018).

20. R. Zhang, Y. Zhang, Z. C. Dong, S. Jiang, C. Zhang, L. G. Chen, L. Zhang, Y. Liao, J. Aizpurua, Y. Luo, J. L. Yang, and J. G. Hou, "Chemical mapping of a single molecule by plasmon-enhanced Raman scattering," Nature **498**, 82-86 (2013).

21. S. Yampolsky, D. A. Fishman, S. Dey, E. Hulkko, M. Banik, E. O. Potma, and V. A. Apkarian, "Seeing a single molecule vibrate through time-resolved coherent anti-Stokes Raman scattering," Nature Photonics **8**, 650-656 (2014).

22. E. Wertz, B. P. Isaacoff, J. D. Flynn, and J. S. Biteen, "Single-Molecule Super-Resolution Microscopy Reveals How Light Couples to a Plasmonic Nanoantenna on the Nanometer Scale," Nano Letters **15**, 2662-2670 (2015).

23. A. Pertsinidis, Y. X. Zhang, and S. Chu, "Subnanometre single-molecule localization, registration and distance measurements," Nature **466**, 647-U611 (2010).

24. H. Deschout, K. Neyts, and K. Braeckmans, "The influence of movement on the localization precision of sub-resolution particles in fluorescence microscopy," Journal of Biophotonics **5**, 97-109 (2012).

25. M. Ovesny, P. Krizek, J. Borkovec, Z. Svindrych, and G. M. Hagen, "ThunderSTORM: a comprehensive ImageJ plug-in for PALM and STORM data analysis and super-resolution imaging," Bioinformatics **30**, 2389-2390 (2014).

26. F. Long, S. Q. Zeng, and Z. L. Huang, "Effects of fixed pattern noise on single molecule localization microscopy," Physical Chemistry Chemical Physics **16**, 21586-21594 (2014).

27. J. Broeken, B. Rieger, and S. Stallinga, "Simultaneous measurement of position and color of single fluorescent emitters using diffractive optics," Optics Letters **39**, 3352-3355 (2014).

28. J. S. Morgan, D. C. Slater, J. G. Timothy, and E. B. Jenkins, "Centroid position measurements and subpixel sensitivity variations with the MAMA detector," Applied Optics **28**, 1178-1192 (1989).

29. H. Li, H. Song, C. Rao, and X. Rao, "Accuracy analysis of centroid calculated by a modified center detection algorithm for Shack–Hartmann wavefront sensor," Optics Communications **281**, 750-755 (2008).

30. R. E. Thompson, D. R. Larson, and W. W. Webb, "Precise nanometer localization analysis for individual fluorescent probes," Biophysical Journal **82**, 2775-2783 (2002).

31. S. W. Hell, and J. Wichmann, "Breaking the diffraction resolution limit by stimulated emission: stimulated-emission-depletion fluorescence microscopy," Optics Letters **19**, 780-782 (1994).

32. M. G. L. Gustafsson, "Nonlinear structured-illumination microscopy: Wide-field fluorescence imaging with theoretically unlimited resolution," Proceedings of the National Academy of Sciences **102**, 13081 (2005).

33. E. Betzig, G. H. Patterson, R. Sougrat, O. W. Lindwasser, S. Olenych, J. S. Bonifacino, M. W. Davidson, J. Lippincott-Schwartz, and H. F. Hess, "Imaging Intracellular Fluorescent Proteins at Nanometer Resolution," Science **313**, 1642 (2006).

34. M. J. Rust, M. Bates, and X. Zhuang, "Sub-diffraction-limit imaging by stochastic optical reconstruction microscopy (STORM)," Nature Methods **3**, 793-796 (2006).

35. A. Sharonov, and R. M. Hochstrasser, "Wide-field subdiffraction imaging by accumulated binding of diffusing probes," Proceedings of the National Academy of Sciences **103**, 18911 (2006).

36. M. Bates, B. Huang, G. T. Dempsey, and X. Zhuang, "Multicolor Super-Resolution Imaging with Photo-Switchable Fluorescent Probes," Science **317**, 1749 (2007).

37. N. Olivier, D. Keller, V. S. Rajan, P. Gönczy, and S. Manley, "Simple buffers for 3D STORM microscopy," Biomedical Optics Express **4**, 885-899 (2013).

38. A. von Diezmann, Y. Shechtman, and W. E. Moerner, "Three-Dimensional Localization of Single Molecules for Super-Resolution Imaging and Single-Particle Tracking," Chemical Reviews **117**, 7244-7275 (2017).

39. B. Huang, H. Babcock, and X. Zhuang, "Breaking the Diffraction Barrier: Super-Resolution Imaging of Cells," Cell **143**, 1047-1058 (2010).

40. H. Shroff, C. G. Galbraith, J. A. Galbraith, H. White, J. Gillette, S. Olenych, M. W. Davidson, and E. Betzig, "Dual-color superresolution imaging of genetically expressed probes within individual adhesion complexes," Proceedings of the National Academy of Sciences **104**, 20308 (2007).

41. R. Jungmann, M. S. Avendaño, J. B. Woehrstein, M. Dai, W. M. Shih, and P. Yin, "Multiplexed 3D cellular super-resolution imaging with DNA-PAINT and Exchange-PAINT," Nature Methods **11**, 313-318 (2014).

42. M. Dai, R. Jungmann, and P. Yin, "Optical imaging of individual biomolecules in densely packed clusters," Nature Nanotechnology **11**, 798-807 (2016).

43. F. Schueder, J. Lara-Gutiérrez, B. J. Beliveau, S. K. Saka, H. M. Sasaki, J. B. Woehrstein, M. T. Strauss, H. Grabmayr, P. Yin, and R. Jungmann, "Multiplexed 3D super-resolution imaging of whole cells using spinning disk confocal microscopy and DNA-PAINT," Nature Communications **8**, 2090 (2017).

44. T. Huang, C. Phelps, J. Wang, L.-J. Lin, A. Bittel, Z. Scott, S. Jacques, S. L. Gibbs, J. W. Gray, and X. Nan, "Simultaneous Multicolor Single-Molecule Tracking with Single-Laser Excitation via Spectral Imaging," Biophysical Journal **114**, 301-310 (2018).

45. S. Malkusch, U. Endesfelder, J. Mondry, M. Gelléri, P. J. Verveer, and M. Heilemann, "Coordinate-based colocalization analysis of single-molecule localization microscopy data," Histochemistry and Cell Biology **137**, 1-10 (2012).

46. K.-H. Song, Y. Zhang, G. Wang, C. Sun, and H. F. Zhang, "Three-dimensional biplane spectroscopic single-molecule localization microscopy," Optica **6** (2019).

47. J. E. Lee, J. C. Sang, M. Rodrigues, A. R. Carr, M. H. Horrocks, S. De, M. N. Bongiovanni, P. Flagmeier, C. M. Dobson, D. J. Wales, S. F. Lee, and D. Klenerman, "Mapping Surface Hydrophobicity of alpha-Synuclein Oligomers at the Nanoscale," Nano Letters **18**, 7494-7501 (2018).

48. B. Huang, S. A. Jones, B. Brandenburg, and X. Zhuang, "Whole-cell 3D STORM reveals interactions between cellular structures with nanometer-scale resolution," Nature Methods **5**, 1047-1052 (2008).

49. B. Huang, W. Wang, M. Bates, and X. Zhuang, "Three-Dimensional Super-Resolution Imaging by Stochastic Optical Reconstruction Microscopy," Science **319**, 810 (2008).

50. M. F. Juette, T. J. Gould, M. D. Lessard, M. J. Mlodzianoski, B. S. Nagpure, B. T. Bennett, S. T. Hess, and J. Bewersdorf, "Three-dimensional sub–100 nm resolution fluorescence microscopy of thick samples," Nature Methods **5**, 527-529 (2008).

51. S. Ram, P. Prabhat, J. Chao, E. Sally Ward, and R. J. Ober, "High Accuracy 3D Quantum Dot Tracking with Multifocal Plane Microscopy for the Study of Fast Intracellular Dynamics in Live Cells," Biophysical Journal **95**, 6025-6043 (2008).

52. M. J. Mlodzianoski, M. F. Juette, G. L. Beane, and J. Bewersdorf, "Experimental characterization of 3D localization techniques for particle-tracking and super-resolution microscopy," Optics Express **17**, 8264-8277 (2009).

53. S. R. P. Pavani, M. A. Thompson, J. S. Biteen, S. J. Lord, N. Liu, R. J. Twieg, R. Piestun, and W. E. Moerner, "Three-dimensional, single-molecule fluorescence imaging beyond the diffraction limit by using a double-helix point spread function," Proceedings of the National Academy of Sciences **106**, 2995 (2009).

54. G. Shtengel, J. A. Galbraith, C. G. Galbraith, J. Lippincott-Schwartz, J. M. Gillette, S. Manley, R. Sougrat, C. M. Waterman, P. Kanchanawong, M. W. Davidson, R. D. Fetter, and H. F. Hess, "Interferometric fluorescent super-resolution microscopy resolves 3D cellular ultrastructure," Proceedings of the National Academy of Sciences **106**, 3125 (2009).

55. D. Aquino, A. Schönle, C. Geisler, C. v. Middendorff, C. A. Wurm, Y. Okamura, T. Lang, S. W. Hell, and A. Egner, "Two-color nanoscopy of three-dimensional volumes by 4Pi detection of stochastically switched fluorophores," Nature Methods **8**, 353-359 (2011).

56. G. Grover, K. DeLuca, S. Quirin, J. DeLuca, and R. Piestun, "Super-resolution photon-efficient imaging by nanometric double-helix point spread function localization of emitters (SPINDLE)," Optics Express **20**, 26681-26695 (2012).

57. S. Quirin, S. R. P. Pavani, and R. Piestun, "Optimal 3D single-molecule localization for superresolution microscopy with aberrations and engineered point spread functions," Proceedings of the National Academy of Sciences **109**, 675 (2012).

58. K. Xu, H. P. Babcock, and X. Zhuang, "Dual-objective STORM reveals three-dimensional filament organization in the actin cytoskeleton," Nature Methods **9**, 185-188 (2012).

59. S. Jia, J. C. Vaughan, and X. Zhuang, "Isotropic three-dimensional super-resolution imaging with a self-bending point spread function," Nature Photonics **8**, 302-306 (2014).

60. Christian M. Winterflood, E. Platonova, D. Albrecht, and H. Ewers, "Dual-Color 3D Superresolution Microscopy by Combined Spectral-Demixing and Biplane Imaging," Biophysical Journal **109**, 3-6 (2015).

61. A. Aristov, B. Lelandais, E. Rensen, and C. Zimmer, "ZOLA-3D allows flexible 3D localization microscopy over an adjustable axial range," Nature Communications **9**, 2409 (2018).

62. M. J. Mlodzianoski, P. J. Cheng-Hathaway, S. M. Bemiller, T. J. McCray, S. Liu, D. A. Miller, B. T. Lamb, G. E. Landreth, and F. Huang, "Active PSF shaping and adaptive optics enable volumetric localization microscopy through brain sections," Nature Methods **15**, 583-586 (2018).

63. B. Dong, B. T. Soetikno, X. Chen, V. Backman, C. Sun, and H. F. Zhang, "Parallel Three-Dimensional Tracking of Quantum Rods Using Polarization-Sensitive Spectroscopic Photon Localization Microscopy," ACS Photonics **4**, 1747-1752 (2017).

64. C. Smith, M. Huisman, M. Siemons, D. Grünwald, and S. Stallinga, "Simultaneous measurement of emission color and 3D position of single molecules," Optics Express **24**, 4996-5013 (2016).

65. S. Culley, D. Albrecht, C. Jacobs, P. M. Pereira, C. Leterrier, J. Mercer, and R. Henriques, "Quantitative mapping and minimization of super-resolution optical imaging artifacts," Nature Methods **15**, 263-266 (2018).

66. N. Banterle, K. H. Bui, E. A. Lemke, and M. Beck, "Fourier ring correlation as a resolution criterion for super-resolution microscopy," Journal of Structural Biology **183**, 363-367 (2013).

67. R. P. J. Nieuwenhuizen, K. A. Lidke, M. Bates, D. L. Puig, D. Grünwald, S. Stallinga, and B. Rieger, "Measuring image resolution in optical nanoscopy," Nature Methods **10**, 557 (2013).

68. T. Kakizuka, K. Ikezaki, J. Kaneshiro, H. Fujita, T. M. Watanabe, and T. Ichimura, "Simultaneous nano-tracking of multiple motor proteins via spectral discrimination of quantum dots," Biomedical Optics Express **7**, 2475-2493 (2016).

69. T. Huang, C. Phelps, J. Wang, L. J. Lin, A. Bittel, Z. Scott, S. Jacques, S. L. Gibbs, J. W. Gray, and X. Nan, "Simultaneous Multicolor Single-Molecule Tracking with Single-Laser Excitation via Spectral Imaging," Biophysical Journal **114**, 301-310 (2018).

70. X. Liu, C. Huang, X. Dong, A. Liang, Y. Zhang, Q. Zhang, Q. Wang, and H. Gai, "Asynchrony of spectral blue-shifts of quantum dot based digital homogeneous immunoassay," Chemical Communications **54**, 13103-13106 (2018).

71. L. Xiang, M. Wojcik, S. J. Kenny, R. Yan, S. Moon, W. Li, and K. Xu, "Optical characterization of surface adlayers and their compositional demixing at the nanoscale," Nature Communications **9**, 1435 (2018).

72. J. Comtet, E. Glushkov, V. Navikas, J. Feng, V. Babenko, S. Hofmann, K. Watanabe, T. Taniguchi, and A. Radenovic, "Wide-Field Spectral Super-Resolution Mapping of Optically Active Defects in Hexagonal Boron Nitride," Nano Letters **19**, 2516-2523 (2019).

73. H. Deschout, F. C. Zanacchi, M. Mlodzianoski, A. Diaspro, J. Bewersdorf, S. T. Hess, and K. Braeckmans, "Precisely and accurately localizing single emitters in fluorescence microscopy," Nature Methods **11**, 253-266 (2014).

74. H. P. Kao, and A. S. Verkman, "Tracking of single fluorescent particles in three dimensions: use of cylindrical optics to encode particle position," Biophysical Journal **67**, 1291-1300 (1994).

75. C. G. Ebeling, A. Meiri, J. Martineau, Z. Zalevsky, J. M. Gerton, and R. Menon, "Increased localization precision by interference fringe analysis," Nanoscale **7**, 10430-10437 (2015).

76. S. W. Hell, and J. Wichmann, "Breaking the Diffraction Resolution Limit by Stimulated-Emission - Stimulated-Emission-Depletion Fluorescence Microscopy," Optics Letters **19**, 780-782 (1994).

77. M. G. L. Gustafsson, "Nonlinear structured-illumination microscopy: Wide-field fluorescence imaging with theoretically unlimited resolution," Proceedings of the National Academy of Sciences **102**, 13081-13086 (2005).

78. E. Betzig, G. H. Patterson, R. Sougrat, O. W. Lindwasser, S. Olenych, J. S. Bonifacino, M. W. Davidson, J. Lippincott-Schwartz, and H. F. Hess, "Imaging intracellular fluorescent proteins at nanometer resolution," Science **313**, 1642-1645 (2006).

79. M. J. Rust, M. Bates, and X. W. Zhuang, "Sub-diffraction-limit imaging by stochastic optical reconstruction microscopy (STORM)," Nature Methods **3**, 793-795 (2006).

80. J. Folling, M. Bossi, H. Bock, R. Medda, C. A. Wurm, B. Hein, S. Jakobs, C. Eggeling, and S. W. Hell, "Fluorescence nanoscopy by ground-state depletion and single-molecule return," Nature Methods **5**, 943-945 (2008).

81. M. Raab, J. J. Schmied, I. Jusuk, C. Forthmann, and P. Tinnefeld, "Fluorescence Microscopy with 6 nm Resolution on DNA Origami," A European Journal of chemical physics and physical chemistry **15**, 2431-2435 (2014).

82. M. J. Dai, R. Jungmann, and P. Yin, "Optical imaging of individual biomolecules in densely packed clusters," Nature Nanotechnology **11**, 798-807 (2016).

83. F. Balzarotti, Y. Eilers, K. C. Gwosch, A. H. Gynna, V. Westphal, F. D. Stefani, J. Elf, and S. W. Hell, "Nanometer resolution imaging and tracking of fluorescent molecules with minimal photon fluxes," Science **355**, 606-612 (2017).

84. A. Yildiz, J. N. Forkey, S. A. McKinney, T. Ha, Y. E. Goldman, and P. R. Selvin, "Myosin V walks hand-over-hand: Single fluorophore imaging with 1.5-nm localization," Science **300**, 2061-2065 (2003).

85. L. S. Churchman, Z. Okten, R. S. Rock, J. F. Dawson, and J. A. Spudich, "Single molecule high-resolution colocalization of Cy3 and Cy5 attached to macromolecules measures intramolecular distances through time," Proceedings of the National Academy of Sciences **102**, 1419-1423 (2005).

86. W. P. Ambrose, and W. E. Moerner, "Fluorescence Spectroscopy and Spectral Diffusion of Single Impurity Molecules in a Crystal," Nature **349**, 225-227 (1991).

87. F. Pinaud, X. Michalet, L. A. Bentolila, J. M. Tsay, S. Doose, J. J. Li, G. Iyer, and S. Weiss, "Advances in fluorescence imaging with quantum dot bio-probes," Biomaterials **27**, 1679-1687 (2006).

88. C. Steinhauer, R. Jungmann, T. L. Sobey, F. C. Simmel, and P. Tinnefeld, "DNA Origami as a Nanoscopic Ruler for Super-Resolution Microscopy," Angewandte Chemie-International Edition **48**, 8870-8873 (2009).

89. J. J. Schmied, A. Gietl, P. Holzmeister, C. Forthmann, C. Steinhauer, T. Dammeyer, and P. Tinnefeld, "Fluorescence and super-resolution standards based on DNA origami," Nature Methods **9**, 1133-1134 (2012).

90. "MATLAB, Statistics and Machine Learning Toolbox userguide ver 11 (The MathWorks Inc, USA, 2001)."

91. R. Jungmann, M. S. Avendaño, M. Dai, J. B. Woehrstein, S. S. Agasti, Z. Feiger, A. Rodal, and P. Yin, "Quantitative super-resolution imaging with qPAINT," Nature Methods **13**, 439 (2016).

92. Y. Feng, P. A. Dalgarno, D. Lee, Y. Yang, R. R. Thomson, and A. H. Greenaway, "Chromatically-corrected, high-efficiency, multi-colour, multi-plane 3D imaging," Optics Express **20**, 20705-20714 (2012).

93. J. A. Kurvits, M. Jiang, and R. Zia, "Comparative analysis of imaging configurations and objectives for Fourier microscopy," Journal of the Optical Society of America A **32**, 2082-2092 (2015).

94. P. Prabhat, S. Ram, E. S. Ward, and R. J. Ober, "Simultaneous imaging of different focal planes in fluorescence microscopy for the study of cellular dynamics in three dimensions," IEEE Transactions on NanoBioscience **3**, 237-242 (2004).

Vita

Education

2006 – 2010   BS in Electrical and Computer Engineering
University of Seoul, Seoul, Korea

2010 – 2012   MS in Information and Communications
Gwangju Institute of Science and Technology, Gwangju, Korea

2016 – 2020   PhD in Biomedical Engineering,
Northwestern University. Evanston, IL, U.S.A.

Professional Experiences

2012 – 2016   Researcher in Space-Time Resolved Molecular Imaging Research Group
Korea Basic Science Institute, Seoul, Korea

Awards and Honors

2016 – 2017   Murphy Fellowship
Northwestern University

2019 – 2020   Christina Enroth-Cugell and David Cugell Graduate Fellowship in Biomedical
Engineering and Visual Neuroscience
Northwestern University

Peer reviewed journal publications (* Equal contribution)

1. **K. Song***, Y. Zhang*, C. Sun, and H. F. Zhang, "Symmetrically dispersed spectroscopic single-molecule localization microscopy", *Light Science and Applications* 9, 90 (2020).

2. J. Davis, Y. Zhang, **K. Song**, E. A. Scott, C. Sun, H. F. Zhang, "Super-resolution imaging of self-assembled nanocarriers using quantitative spectroscopic analysis for cluster extraction", *Langmuir* 36, 2291-2299 (2020).

3. L. Sansalone, Y. Zhang, M. M. Mazza, J. Davis, **K. Song**, B. Captain, H. F. Zhang, F. M. Raymo, "High-Throughput Single-Molecule Spectroscopy Resolves the Conformational Isomers of BODIPY Chromophores", *Journal of Physical Chemistry Letters* 10, 6807-6812 (2019).

4. **K. Song**, Y. Zhang, G. Wang, C. Sun, and H. F. Zhang, "Three-dimensional biplane spectroscopy single-molecule localization microscopy", *Optica* 6, 709-715 (2019).

5. Y. Zhang*, **K. Song***, B. Dong, J. Davis, C. Sun, and H. F. Zhang, "Multi-color Super-Resolution Imaging using spectroscopic single-molecule localization microscopy", *Applied Optics* 58, 2248-2255 (2019).

6. **K. Song***, B. Dong*, C. Sun, and H. F. Zhang, "Theoretical analysis of spectral precision in spectroscopic single-molecule localization microscopy", *Review of Scientific Instruments* 89, 123703 (2018).

7. Y. Zhang, **K. Song**, S. Tang, L. Ravelo, J. Cusido, C. Sun, H. F. Zhang, and F. M. Raymo, "Far-red photoactivatable BODIPYs for the Super-resolution Imaging of live cells", *Journal of the American Chemical Society* 140, 12741-12745 (2018).

8. **K. Song**, M. Gu, M. Kim, H. Kwon, H. Rhee, H. Han, and M. Cho, "Quantum beats and phase shifts in two-dimensional electronic spectra of Zinc naphthalocyanine monomer and aggregate", *Journal of Physical Chemistry Letters* 6, 4314-4318 (2015).

9. D. Lee, J. Lee, **K. Song**, H. Rhee, and D. Jang, "Formation and decay of charge carriers in aggregate nanofibers consisting of poly(3-hexylthiophene)-coated gold nanoparticles", *Physical Chemistry Chemical Physics* 18, 2087-2096 (2015).

10. H. Rhee, I. Eom, S. Ahn, **K. Song**, and M. Cho, "Chiroptical signal enhancement in quasi-null-polarization-detection geometry: Intrinsic limitations", *Physical Review A* 91, 053839 (2015).

11. S. Jeon, **K. Song**, K. Kim, M. Jung, and C. Park, "Polarization-insensitive wideband OSNR monitoring using thermally expanded core fiber", *IEEE Photonics Technology Letters* 23, 1421-1423 (2011).